ROBUST, REUSABLE QUBITS FOR QUANTUM INFORMATION APPLICATIONS

A Thesis
Presented to
The Academic Faculty

by

Michael J. Gibbons

In Partial Fulfillment
of the Requirements for the Degree
Doctor of Philosophy in the
School of Physics

Georgia Institute of Technology
May, 2011

ROBUST, REUSABLE QUBITS FOR QUANTUM INFORMATION APPLICATIONS

Approved by:

Professor Michael Chapman, Advisor
School of Physics
Georgia Institute of Technology

Professor Phillip First
School of Physics
Georgia Institute of Technology

Professor T. A. Brian Kennedy
School of Physics
Georgia Institute of Technology

Professor Ken Brown
School of Chemistry
Georgia Institute of Technology

Professor Rick Trebino
School of Physics
Georgia Institute of Technology

Date Approved: 8 December, 2010

ACKNOWLEDGEMENTS

I would first like to thank my advisor, Professor Michael Chapman. From the moment I entered graduate school, he has been supportive and helpful. He has always been ready with ideas and suggestions, while still giving me enough room to try things on my own. I have greatly enjoyed the opportunity to work in his lab and to benefit from his knowledge and experience. Thanks also to my committee members, Professors Brian Kennedy, Rick Trebino, Phil First, and Ken Brown, for the time and effort they spent helping me finalize my thesis.

I would like to thank Kevin Fortier for his guidance and patience through my first few years working in the lab. He gave me extensive instruction, regarding both our specific experiments and experimental physics in general. He was always available to help as I was assembling my experiment, and his expertise was crucial for its success.

I had the pleasure of working together with several other graduate students and postdocs, all of whom supported or encouraged me during my time at Georgia Tech. Ming-Shien Chang guided me my first semester in the lab and taught me the basics of how to run an experiment. Peyman Ahmadi worked closely with me on my first paper, assisting with both writing and data collection. Chris Hamley has been an endless source of ideas and suggestions, many of which have proved vital to the experiment. I also appreciate his constant encouragement and general camaraderie. I have had the privilege of working alongside many others as well, including Soo Kim, Chung-Yu Shih, Jacob Sauer, Eva Bookjans, Adam Steele, Layne Churchill, Michael DePalatis, Paul Griffin, and Ghazal Behin-Aein. All of them have been wonderful colleagues, and have helped make the lab an enjoyable place to work.

I would like to thank my family for their constant support throughout my time

as a graduate student. Thank you for all of your help and encouragement, and for giving me someone to talk to when things weren't going well. A big thank you to Bob and Debbie Sullivan, who always looked out for me and treated me like a member of the family, as well as to Frank and Ruth Holleman and Andrew Fuggle.

Finally, I would like to thank Jesus Christ, my Lord and Savior. My life is yours; may everything I do be for Your glory.

TABLE OF CONTENTS

LIST OF FIGURES

SUMMARY

Most neutral atom quantum computing experiments rely on destructive state detection techniques that eject the detected qubits from the trap. These techniques limit the repetition rate of these experiments due to the necessity of reloading a new quantum register for each operation.

We address this problem by developing reusable neutral atom qubits. Individual ^{87}Rb atoms are trapped in an optical lattice and are held for upwards of 300 s. Each atom is prepared in an initial quantum state and then the state is subsequently detected with 95% fidelity with less than a 1% probability of losing it from the trap. This combination of long storage times and nondestructive state detection will facilitate the development of faster and more complex quantum systems that will enable future advancements in the field of quantum information.

CHAPTER I

INTRODUCTION

1.1 Classical Information Storage

Methods of information storage have existed for thousands of years. Ancient civilizations used pictures and objects to store and transmit important information and concepts. These gave way to ideographic and phonetic writing systems, descendants of which are still in use today. Until the last century, written languages represented the most effective and reliable method of information storage [1]. However, with the development of the first digital computers in the 1940s, and the first digital magnetic storage in the 1950s, a new paradigm in information storage began to emerge. The storage and transmission capacities for digital information quickly eclipsed traditional systems and have been increasing exponentially ever since. Today, the vast majority of information is coded and stored primarily in digital form.

The most basic unit of digital information is a bit. A bit is a mathematical representation of a two state system, with the two states typically denoted as 0 and 1. Using a sufficiently large number of bits, any arbitrary information can be stored in binary through an appropriately defined conversion process. All information stored in modern computers is composed of bits. Bits are, in turn, frequently assembled into bytes, units which consist of strings of eight bits.

One of the first digital storage mediums was the punch card. Punch cards were first used in the 1700's to control textile looms, and were adapted for data storage in 1889 [2]. Several decades later, magnetic storage began to replace punch cards, first in primary computer memory and later for archival storage. At the same time, memory capacity rapidly increased, while the physical size of each bit decreased accordingly. In

modern computer memory, a typical bit is less than 25 nm across, with new technology constantly reducing this value. These advancements have revolutionized information storage, making it possible to accurately preserve unprecedented amounts of data [1].

The march of progress in the computer industry in the past forty years has been impressive, but new innovations will soon be required. As modern processors rapidly approach fundamental limits of performance imposed by the size of the atom, it becomes increasingly important to explore new paradigms in information science. A particularly fascinating approach to surpassing these limits harnesses the power of quantum mechanics to effectively enable massive parallel calculations. This field of research is generally known as quantum information.

1.2 Quantum Information

One of the first people to suggest applying the principles of quantum mechanics to computing problems was Richard Feynman, in 1982. In order to overcome the difficulty of modeling quantum mechanical processes on a classical computer, he suggested the construction of a quantum simulator, which would model a quantum system by using another quantum system [3]. David Deutsch extended this idea to propose a general-purpose quantum computer, which could simulate any quantum system [4]. A quantum simulator would help solve a large array of theoretical problems, and would therefore be an extremely valuable tool for physicists.

In 1994, Peter Shor developed an algorithm for a quantum computer that was designed to factor large numbers [5]. Factoring large numbers take an exponential amount of time to solve classically, but the solution can be checked in polynomial time. In contrast, Shor's algorithm can solve such a problem in polynomial time, given a sufficiently powerful quantum computer. A few years later, another quantum algorithm was proposed by Lov Grover [6]. Using Grover's algorithm, a quantum

computer can perform a search of an unordered database much faster than any classical computer. The discovery of these quantum algorithms led to increased interest from the general public and funding from the government, and efforts to build a quantum computer intensified.

Several elements are required in order to create a quantum computer [7]. The first requirement is a source of stable quantum bits (qubits). A qubit is the quantum version of the bit. Whereas a bit can only occupy one of two states (0 or 1), a qubit can be in any quantum superposition of the two, with the most general state given by $|\psi\rangle = \alpha|0\rangle + \beta|1\rangle$, where $\alpha^2 + \beta^2 = 1$. A quantum computer will require a large array of qubits, which must be individually addressable without disturbing any of the neighboring qubits. Further, a quantum computer must be able to initialize each of these qubits into a specific quantum state, with high reliability.

The next requirement is the ability to perform quantum gate operations. In addition to state manipulations involving one qubit, a quantum computer requires the ability to generate entanglement between arbitrary pairs of qubits. All necessary two-qubit manipulations can be achieved by implementing a series of controlled-not (CNOT) gates. A CNOT gate takes two input qubits, the control and the target. If the control qubit is in the $|1\rangle$ state, then a NOT is performed on the target qubit. Otherwise, the inputs are unchanged. If the control qubit is in an equal superposition state, $|\psi\rangle = \frac{1}{\sqrt{2}}(|0\rangle + |1\rangle)$, and the target is in the state, $|\psi\rangle = |1\rangle$, then a CNOT gate will produce an entangled state, $|\psi\rangle = \frac{1}{\sqrt{2}}(|1\rangle|0\rangle + |0\rangle|1\rangle)$. Any arbitrary quantum calculation can be performed through a series of one-qubit unitary operations and two-qubit CNOT gates. The final step in a quantum calculation is to read out the result. This requires the ability to accurately detect the state of each qubit, either sequentially or all at once. Furthermore, all of the preceding steps must be accomplished within a time period significantly shorter than the coherence time or the qubit loss rate.

1.3 Quantum Computing

Experimental work in quantum computing has advanced a great deal over the last fifteen years. Although large-scale quantum computations are still perhaps many decades away, a number of important milestones have been reached, and steady progress is being made. Some of the most promising results to date in quantum computing have used trapped ions. The first quantum logic gate using trapped ions was demonstrated in 1995 [8]. Three years later, the same group demonstrated the ability to deterministically entangle two ions with a fidelity of 0.7 [9]. This fidelity was later improved to better than 0.97 [10]. In 2005, Grover's search algorithm was implemented using two trapped ions [11] and entanglement between eight ions was demonstrated [12]. Two-dimensional control over trapped ions was achieved in 2006 [13], and in 2009, a prototype for a scalable quantum processor was demonstrated [14].

Neutral atom quantum computing experiments have thus far lagged somewhat behind ion trapping. This is mainly due to the relative ease of trapping ions. Because ions are charged, they can be trapped directly using electric fields, which produce an extremely deep trap. The resulting potential can be many hundred thousand times deeper than a typical neutral atom trap. Furthermore, since ions are mutually repulsive, they naturally tend to form convenient strings or lattices at fixed intervals. This makes maintenance and manipulation of trapped ion strings relatively easy compared to neutral atoms. Nevertheless, neutral atom traps have several distinct advantages over ion traps. While strings of ions are easy to generate, neutral atom traps scale more easily into two and three dimensions. In addition, ion traps require a physical trap structure near the trap, while neutral atom traps can be constructed entirely using laser beams. Ion traps also require a source of ionized atoms, typically an oven or heated filament. In contrast, neutral atom traps require only an evaporative neutral atomic source. This reduces the complexity of neutral atom vacuum chambers. The

lack of a physical trapping structure can also increase optical access to the trapped atoms, and the lack of a charge eliminates any concerns about electric interactions between the atoms and nearby surfaces. Finally, neutral atom quantum operations can be performed very quickly using Rydberg gates [15].

Recently, neutral atom experiments have made significant progress. Trapping of single neutral atoms in a MOT was first demonstrated in 1994 [16]. Meschede's research group was able to transfer individual atoms into an optical trap in 2000 [17], and into an optical lattice the following year [18]. This led to the development of a neutral atom quantum register in 2004 [19]. Volz et al. were able to create entanglement between a single atom and a single photon in 2006 [20], and the first entanglement between two neutral atoms was reported in 2010 [21]. This was followed shortly by the implementation of the first neutral atom CNOT gate [22]. These recent developments are extremely promising. Nevertheless, the relative difficulty involved in storage and maintenance of neutral atom qubits has limited the rate and scope of these experiments. This problem could be largely solved through the development of an improved quantum register.

1.4 Quantum Registers

The quantum register is the quantum equivalent of a classical processor register. A quantum register is simply a piece of quantum memory, a string of qubits that can be initialized and entangled. There are several general requirements for a useful quantum register. At a minimum, it must hold enough qubits to enable a single quantum calculation of the desired complexity, and it must be stable enough to faithfully maintain the quantum states for the duration of the calculation. Furthermore, it must be possible to perform initialization operations on any single qubit in the register and to perform entanglement operations on any pair of qubits. If the gate operations consist solely of a series of externally directed laser pulses, then a fixed register is probably

sufficient. However, direct interaction approaches, such as collisional entanglement, and complex hardware approaches, such as those involving optical cavities, will demand greater versatility. For such operations, the quantum register must be able to move specific qubits to the location where they can become entangled.

A quantum register can be characterized by at least three important parameters. The first is its capacity, or the total number of qubits it can hold. This value directly limits the scope of quantum calculations that can be performed. To solve problems that are intractable for a classical computer, at least a few hundred qubits would be required. The second important attribute of a quantum register is its coherence time. If the coherence time isn't significantly larger than the total calculation time, errors will be introduced into the calculation. Error correction can counteract this to some degree, but at the cost of further overhead [23]. The final important parameter is the maximum possible repetition rate for performing quantum calculations. In an ideal system, the repetition rate would be determined by the speed of the entanglement generation. However, if the quantum register must be rebuilt for each calculation, the repetition rate is instead limited by the time required to prepare a new register.

Neutral atom quantum registers have progressed a great deal over the last several years. In 2002, Greiner et al. used the Mott insulator phase transition to fill each site in an optical lattice with exactly one atom [24]. In 2007, individual atoms were trapped in a three-dimensional lattice with over 500 resolvable lattice sites, with each site separated by 5 μm [25]. A quantum gas microscope using high numerical aperture optics was demonstrated in 2009 and was able to resolve trapping sites separated by only 640 nm [26]. These trapping sites were generated in two dimensions by using a holographic mask and focusing the trapping light through the imaging optics. In 2010, Klinger et al. proposed a register which employs two independent hexagonal lattices at different wavelengths to trap two different species of atoms [27].

Despite these advancements, most neutral atom qubit systems share a common

limitation. Neutral atom state readout is typically destructive (in the sense that many of the atoms are ejected from the trap), requiring that qubits be reloaded after each measurement. Our work focuses on the production of robust and reusable qubits for quantum information applications. First, we demonstrate drastically increased trap lifetimes, using both active and passive means. We then achieve non-destructive state detection of a neutral atom qubit trapped in an optical lattice, including the ability to prepare and detect the same qubit as many as 100 times without losing it from the trap. By demonstrating reliable, non-destructive state detection in free space, coupled with extremely long storage times, this work will significantly advance the state of neutral atom quantum computing.

The first portion of this thesis will discuss the history and theory behind neutral atom trapping and quantum information. This will cover past work with neutral atom qubits and explain the need for improved storage and detection schemes. Following that is a description of the basic experimental setup, which will lay the groundwork for the experimental sections to follow. The latter part of this thesis will focus on experimental contributions. Chapter 5 will present trap heating and cooling measurements as well as a variety of cooling schemes. Chapter 6 will describe the system used to achieve non-destructive state detection. This thesis will conclude by discussing ways to improve on the system, as well as how one might implement these improvements in a full scale quantum computing experiment.

CHAPTER II

NEUTRAL ATOM TRAPPING

The first neutral atom trap to be developed was the magnetic trap, which uses magnetic forces to capture atoms. It was first demonstrated by Metcalf et al. in 1985 [28], although it had been initially proposed much earlier [29, 30]. Later that same year, the first optical molasses was developed [31]. An optical molasses uses laser beams to cool atoms. This was followed by the creation of a magneto optical trap (MOT) in 1987 [32]. The MOT has several advantages over the magnetic trap. In particular, it requires much smaller magnetic fields and is able to trap a greater number of atomic states. It was later shown to have excellent versatility and control, working well even in the single atom limit [16].

Another technique for trapping atoms, first demonstrated in 1986, is the optical dipole trap [33]. This type of trap is much shallower than the others, and therefore requires a source of cold atoms. Nevertheless, it can provide much tighter confinement and more controllability than either of the other types of trap, and is, therefore, well suited for quantum information applications. This chapter will focus on the development and theory of optical molasses, the MOT, and the optical dipole trap.

2.1 Optical Molasses

Optical molasses was first demonstrated at Bell Labs in 1985 [31]. It utilizes a set of lasers, detuned slightly from an atomic resonance, to cool atoms. For the correct detuning, the Doppler effect gives rise to a velocity-dependent radiation force that causes the atoms to lose energy on average. For many experiments, this cooling process is the first step toward trapping atoms. As such, it is worthwhile to present the elementary theory.

The momentum of a single photon is $\vec{p} = \hbar\vec{k}$, where $\vec{k}$ is the wave vector, which has a magnitude equal to $2\pi/\lambda$ and points in the direction of motion of the photon. When a photon is absorbed by an atom, this momentum transfers to the atom. If a beam of light, resonant to an atomic transition, is applied to an atom, this creates an average force in the direction of the light, proportional to the momentum of the photons. For a two-level atom, this force is given by [34],

$$\vec{F} = \hbar\vec{k}\gamma/2\frac{s_0}{1+s_0}, \tag{2.1}$$

where γ is the linewidth of the excited state and s_0 is the on-resonance saturation parameter, defined as the ratio of the intensity of the light, I, to the saturation intensity, I_s. The saturation intensity is defined as:

$$I_s = \frac{\pi\hbar c\gamma}{3\lambda^3}. \tag{2.2}$$

If the frequency of the light is shifted from atomic resonance by a detuning δ, the resulting force is reduced somewhat and is given by [34],

$$\vec{F} = \hbar\vec{k}\gamma/2\frac{s_0}{1+s_0+(2\delta/\gamma)^2}. \tag{2.3}$$

For an atom in motion with a velocity $\vec{v}$, the effective frequency of the light as seen by the atom is Doppler shifted by $\delta_w = -\vec{k}\cdot\vec{v}$. This changes the effective detuning of the light, adding a velocity-dependent component, given by,

$$\delta_+ = \delta - \vec{k}\cdot\vec{v}. \tag{2.4}$$

If a second beam of light is added, identical to the first but counter-propagating, with a wave vector $\vec{k}_2 = -\vec{k}$, this produces a combined force given by $\vec{F} = \vec{F}_+ + \vec{F}_-$, where

$$\vec{F}_\pm = \pm\hbar\vec{k}\gamma/2\frac{s_0}{1+s_0+(2(\delta\mp\vec{k}\cdot\vec{v})/\gamma)^2}. \tag{2.5}$$

In the limit of small atomic velocities, this force can be approximated by [34],

$$\vec{F} \approx 8\hbar|k|^2\delta\frac{s_0}{\gamma(1+s_0+(2\delta/\gamma)^2)^2}\vec{v} \equiv -\beta\vec{v}, \tag{2.6}$$

where β is the damping coefficient. If the detuning δ is negative, then β is positive, and the resulting force opposes the motion of the atoms.

If this was the only force on the atoms, and the force was continuous, then the atoms would quickly be brought completely to rest. In reality, as the atoms re-emit the absorbed photons, this creates a heating force that ultimately limits the temperature achievable by Doppler cooling. For each absorption and reemission event, the average kinetic energy of the atoms increases by twice the recoil energy, which leads to a heating rate of $4\hbar\omega_r\gamma$ [34]. Setting this equal to the cooling rate, and assuming a saturation parameter less than one, gives a steady state kinetic energy of:

$$E_{kinetic} = \hbar\gamma/8\left(\frac{\gamma}{2\delta} + \frac{2\delta}{\gamma}\right). \tag{2.7}$$

This energy is minimized when the detuning is equal to half the linewidth, and produces a minimum temperature (called the Doppler temperature), given by [34, 35],

$$T_D = \hbar\frac{\gamma}{2k_b}, \tag{2.8}$$

where k_b is Boltzmann's constant. Doppler temperatures for the alkali atoms range from about 100 to 250 μK.

2.2 Sub-Doppler Cooling

Early experiments in Doppler cooling were able to achieve temperatures significantly below the Doppler temperature, violating the predicted theoretical limitations [36]. These unexpected results spurred further theoretical work, which led to the identification of additional cooling mechanisms, referred to generally as sub-Doppler cooling, or polarization gradient cooling. These cooling methods depend on the polarizations of the optical molasses beams [37, 38], and we will focus on σ_+-σ_- polarization gradient cooling, which is used in this thesis.

Two counter-propagating beams with orthogonal circular polarizations produce a light field with uniform magnitude and linear polarization, but the direction of the

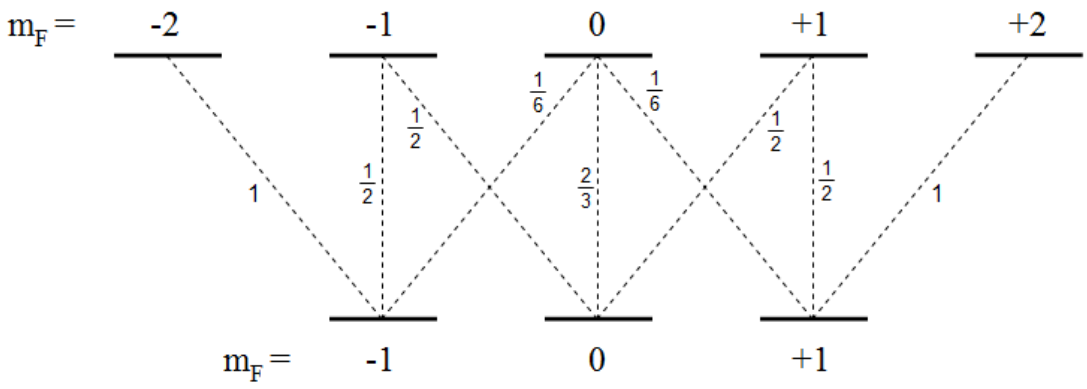

Figure 2.1: State diagram for an $F = 1 \rightarrow F' = 2$ transition.

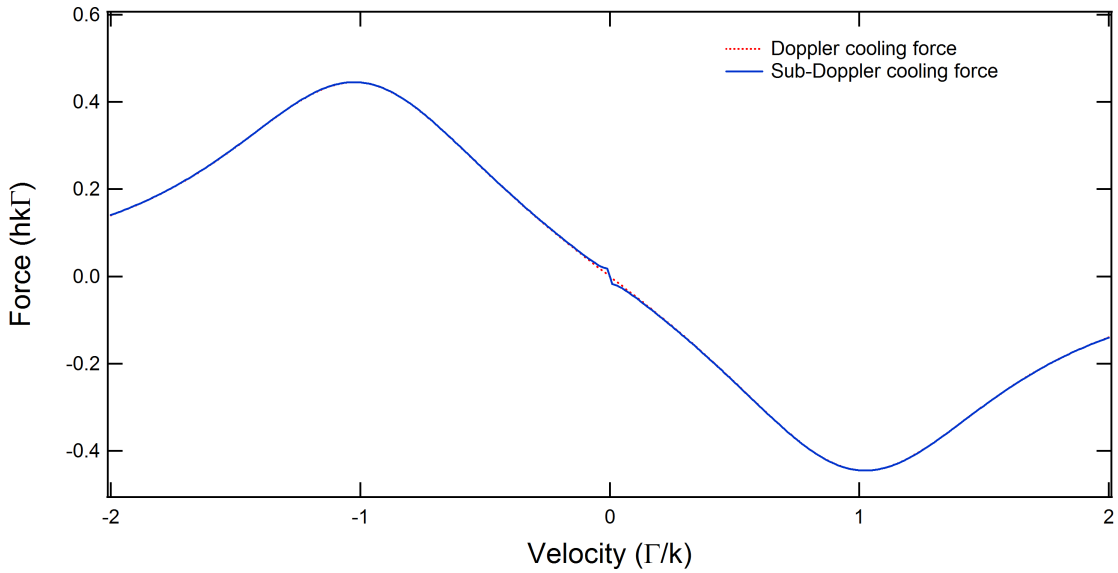

Figure 2.2: Graph comparing the Doppler and sub-Doppler cooling forces. The dotted red line represents the Doppler force. The solid blue line represents the sub-Doppler force. The sub-Doppler force is much steeper at the origin, leading to a lower minimum temperature.

polarization changes with respect to position. For simplicity, let us assume for the moment that the ground state has three Zeeman sublevels (the same process will work for more than three). The proposed system is illustrated in Figure 2.1. Given a stationary atom in linearly polarized light, the atom will be preferentially pumped into the $m_F = 0$ state. As the atom moves, the direction of the linear polarization changes faster than the orientation of the atom. This brief non-adiabaticity produces an optical pumping effect which favors either the $m_F = +1$ or $m_F = -1$ state. Assuming small atomic velocities ($kv << \delta$), this leads to a state imbalance given by [38]:

$$P_{+1} - P_{-1} \approx \frac{40}{17}\frac{kv}{\delta}, \tag{2.9}$$

where P_{+1} and P_{-1} are the population in the $m_F = +1$ and $m_F = -1$ states respectively. Therefore, if the light is detuned to the red of the transition, atoms traveling towards the σ_+ light are more likely to be in the $m_F = +1$ state. Referring back to Figure 2.1, these atoms are then also more likely to scatter σ_+ photons. Similarly, an atom moving towards the σ_- light is more likely to be pumped into the $m_F = -1$ state, and therefore more likely to scatter σ_- light. In the limit of low laser power and low atomic velocity ($kv << s\gamma$, $s << 1$), this results in a force, given by [38]:

$$\vec{F} = \frac{120}{17}\frac{\delta\gamma}{5\gamma^2 + 4\delta^2}\hbar k^2 \vec{v}. \tag{2.10}$$

This force opposes the direction of motion if the detuning is negative (see Figure 2.2). Combined with Doppler cooling, this produces a theoretical minimum temperature (in the semi-classical approximation) of:

$$k_B T = \frac{\hbar\Omega^2}{|\delta|}\left(\frac{29}{300} + \frac{254}{75}\frac{\gamma^2/4}{\delta^2 + \gamma^2/4}\right), \tag{2.11}$$

where $\Omega = \sqrt{s_0/2}\gamma$ is the generalized Rabi frequency. This expression assumes that the temperature is large compared to the heating caused by a single photon recoil. This cooling method relies entirely on photon scattering, and every scattering

event is followed by the emission of a photon, which heats the atom. Therefore, the lowest temperature that can be achieved is the recoil temperature, $k_B T_r = \hbar^2 k^2/(2m)$, representing the energy imparted by a single photon recoil.

2.3 Magneto-Optical Trap

Optical molasses is an excellent tool for cooling atoms, but because the forces are not position dependent, it does not constitute a trap. One solution to this problem, first demonstrated in 1987 [32], uses a magnetic field gradient, in combination with the optical molasses light, to create a position-dependent force. This type of trap is known as the magneto optical trap (MOT).

An atom with angular momentum $F = 0$ in the ground state and $F' = 1$ in the excited state is placed in a one-dimensional optical molasses with detuning $\delta < 0$. The excited state has three m_F states, which are degenerate in the absence of a magnetic field. Once a magnetic field is applied, the Zeeman effect causes a state-dependent energy shift with magnitude given by [39],

$$\Delta E = \vec{\mu} \cdot \vec{B} = \mu m_F B. \tag{2.12}$$

We now apply a magnetic field of the form $B(z) = B_0 z$. If the atom is in a position $z > 0$, the energy of the $m_F = +1$ state is increased, while the energy of the $m_F = -1$ state is decreased. Now the $F = 0, m_F = 0 \rightarrow F' = 1, m_F = 1$ transition is further away from the laser frequency, while the $F = 0, m_F = 0 \rightarrow F' = 1, m_F = -1$ transition is closer to the laser frequency. This means that atoms in the $z > 0$ region are more likely to absorb σ_- light than σ_+ light. For the $z < 0$ region, this effect is reversed.

Each laser beam is now prepared with a specific circular polarization. The light coming from the +z direction is given σ_- polarization, and the light coming from the -z direction is given σ_+ polarization. The result is that atoms at any point other than the origin are more likely to scatter light that pushes them toward the origin

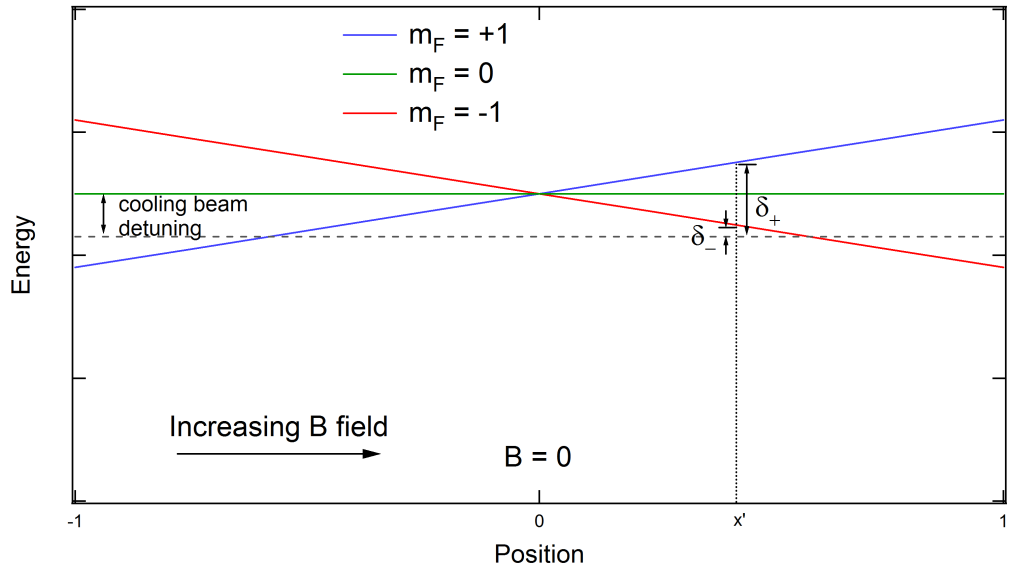

Figure 2.3: Illustration of the position-dependent trapping force in a MOT. As the magnetic field increases, the Zeeman shift causes the $m_F = -1$ transition (red line) to move closer to resonance with the detuned laser. Assuming the beam coming from the +z direction is σ_- polarized, there is a net force pushing the atom toward the origin.

than light that pushes them away (see Figure 2.3). For small Zeeman shifts compared to the laser detuning, this produces an average restoring force which is linear with position.

This example addresses only one dimension, but it can be extended to three dimensions by using six optical molasses beams, two in each direction, and a magnetic field produced by two coils of wire in an anti-Helmholtz configuration. This setup provides cooling and trapping in all three dimensions. Also, the example assumed a single cycling transition. Real atoms do not typically have convenient closed transitions between two levels. In cases with multiple ground states, one or more repump lasers may be necessary to return the atom to the desired ground state [34].

MOTs are very useful for general cooling and trapping of atoms, but they also have limitations that preclude their direct use for storing individual atomic qubits. First, maintaining the trap requires constant repeated excitation on a cycling transition.

This means the state of the trapped atoms is constantly being perturbed. Second, atoms are continuously being slowed by the molasses and captured in the MOT, so it is difficult to isolate a particular sample of atoms for any significant amount of time. In addition, it is difficult to tightly confine atoms using a MOT. Although the size of a MOT can vary depending on experimental parameters, it is very difficult to obtain a diameter less than 20 μm.

2.4 Optical Traps

Many of the limitations of a MOT are avoided in traps based on the optical dipole force. The first optical traps were created in 1970 by Arthur Ashkin at Bell Labs [40], who used a focused argon ion laser to manipulate the movement of latex beads floating in water. When the laser was turned on, the beads would be attracted to the focus of the laser and remain trapped there. If the laser was then turned off, the beads would resume normal Brownian motion. This so-called optical tweezers technique has become an important tool in biophysics [41] and can be used for precise manipulation of organic matter. Optical traps are useful for a broad variety of applications because they can generate a force on any material that can be polarized. In his paper describing this effect, Ashkin suggested using optical traps to confine neutral atoms. However, even with powerful lasers, the trapping potential for atoms is very small. Optical atom traps thus require a source of pre-cooled atoms, and for this reason, an optical trap for neutral atoms was not demonstrated until 16 years later.

The breakthrough which finally allowed the creation of neutral atom optical traps was the development of the optical molasses. The optical molasses provided a convenient source of cold atoms, which could then be loaded into an optical trap. Optical dipole trapping of neutral atoms was first demonstrated by Cable et al. in 1986 [33], using a laser detuned up to 1300 GHz from resonance. The trap had a lifetime of

only 5 ms, limited by laser heating of the atoms due to off-resonant scattering from the trapping beam. In order to overcome this obstacle and improve the trap lifetime, the far off resonant trap (FORT) was developed. The first FORT, demonstrated by Dan Heinzen's group in 1993, used trapping light detuned 65 nm from resonance [42]. Although this required higher laser power than a near-resonant trap, it significantly reduced off-resonant scattering and improved the lifetime by more than an order of magnitude.

Optical dipole traps have now become an essential tool in ultracold atomic and molecular physics. They have applications in important research areas including atomic frequency standards [43], tests of fundamental symmetries [44], quantum degenerate gases [45, 46], single-atom trapping [17, 47, 48, 49], and the development of scalable quantum information processing systems [19]. Furthermore, optical trapping potentials can be tailored through the choice of optical wavelengths and laser beam configurations to yield a wide variety of trapping arrangements. This section will first discuss the general theory behind optical dipole traps and will then look at different trap configurations and practical applications.

2.4.1 Dipole Trap Theory

The optical dipole force results from the interaction between an induced electric dipole and a spatially non-uniform electric field. The induced dipole moment is proportional to the electric field [50],

$$\vec{p} = \alpha \vec{E}, \tag{2.13}$$

where α is the complex polarizability. In the classical limit, one can use the Lorentz model of an oscillator, which assumes the electron is bound to the atom by a spring force. The oscillation is driven by the electric field, and the acceleration of the electron leads to damping according to the Larmor formula. Solving the resulting equation of

motion leads to a complex polarizability of [50],

$$\alpha = 6\pi\epsilon_0 c^3 \frac{\Gamma/\omega_0^2}{\omega_0^2 - \omega^2 - i(\omega^3/\omega_0^2)\Gamma}, \tag{2.14}$$

where ϵ_0 is the permittivity of free space, ω is the driving frequency, and ω_0 is the transition frequency. The interaction potential generated by the electric field is given by,

$$U_{dip} = -\frac{1}{2}\left\langle \vec{p}\cdot\vec{E}\right\rangle = -Re(\alpha)\left|E\right|^2. \tag{2.15}$$

Substituting in the previous expression for α and the laser intensity, $I = 2\epsilon_0 c\left|E\right|^2$, gives:

$$U_{dip}(\vec{r}) = -\frac{3\pi c^2}{2\omega_0^3}\left(\frac{\Gamma}{\omega_0-\omega} + \frac{\Gamma}{\omega_0+\omega}\right) I(\vec{r}). \tag{2.16}$$

If one applies the rotating wave approximation by assuming that $\delta = \omega - \omega_0 << \omega_0$, the second term vanishes, giving the final expression for the potential:

$$U_{dip}(\vec{r}) = \frac{3\pi c^2}{2\omega_0^3}\frac{\Gamma}{\delta} I(\vec{r}). \tag{2.17}$$

Note that the potential has the same sign as the detuning. This means that, for a negative detuning, an atom will be drawn toward the area of maximum intensity, while for a positive detuning, the atom will be pushed away. Both of these regimes can be used to trap atoms, as will be seen later.

The power absorbed (and later re-emitted) by the atom is related to the rate of change of the dipole moment, according to

$$P = \left\langle \dot{\vec{p}}\cdot\vec{E}\right\rangle = 2\omega I_m(\alpha)\left|E\right|^2. \tag{2.18}$$

Dividing by the energy per photon, $\hbar\omega$, gives the photon scattering rate. Substituting in the expression for α and taking the rotating wave approximation gives

$$\Gamma_{sc}(\vec{r}) = \frac{3\pi c^2}{2\hbar\omega_0^3}\left(\frac{\Gamma}{\delta}\right)^2 I(\vec{r}). \tag{2.19}$$

By comparing this expression to the expression for the dipole potential, it can be seen that the potential scales with $1/\delta$, while the scattering rate scales with $1/\delta^2$. This

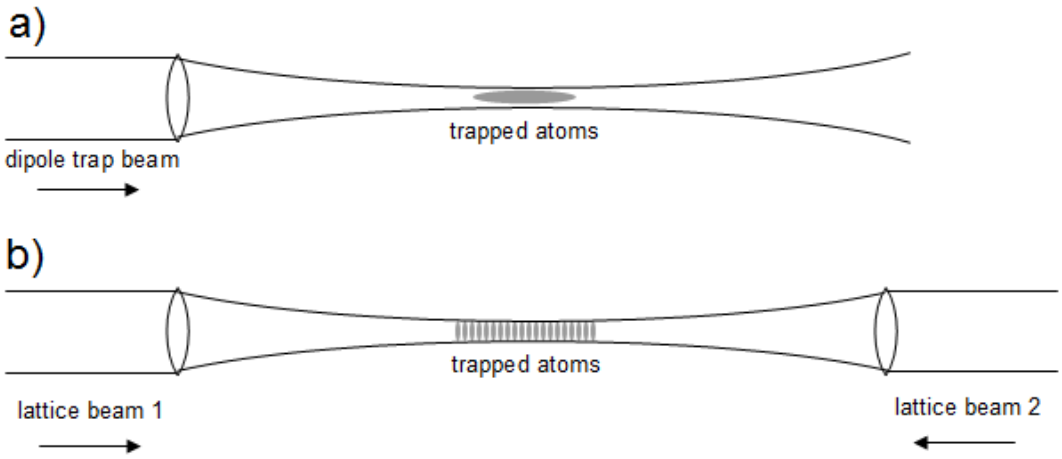

Figure 2.4: Illustration of atoms in (a) a single focus trap and (b) an optical lattice.

means that, for a given trap depth, using a laser detuned further from resonance will generate a smaller scattering rate.

One other thing to note is that all of these calculations have assumed a simple two-level atom with one resonance. For real atoms, multiple transitions must usually be taken into account in order to obtain accurate results. The total potential then becomes the sum over the potential produced from each applicable resonance.

2.4.2 Single Focus Trap

The simplest optical trap can be created by tightly focusing a red detuned laser (see Figure 2.4(a)). Since red detuned light ($\delta < 0$) causes atoms to move to the maximum intensity, this produces a trap at the focus of the beam. These single focus traps provide the easiest means of trapping atoms using the dipole force. Typically, the trapping beam is focused on the center of a MOT. Atoms are first loaded into the MOT and then transferred into the single focus trap. The atoms are typically confined more tightly than in a MOT and are not continuously subjected to perturbations from near-resonant light. For sufficiently large trapping light detuning, lifetimes of

hundreds of seconds can be achieved, usually limited by collisions with background gases [51].

For a focused Gaussian trapping beam, near the focus, the intensity profile in cylindrical coordinates is [52],

$$I(r,z) = \frac{2P}{\pi w^2(z)} e^{-\frac{2r^2}{w^2(z)}}, \tag{2.20}$$

where P is the total optical power and w is the waist of the trapping beam. This intensity profile provides relatively tight confinement in the radial direction, and looser confinement in the axial direction. The maximum trap depth is found using Eq. (2.17) and substituting in the optical intensity at $z = r = 0$, giving:

$$U_{trap} = \frac{3c^2}{\omega_0^3} \frac{\Gamma}{\Delta} \frac{P}{w_0^2}. \tag{2.21}$$

For tighter confinement, an additional perpendicular trapping laser beam can be added to create a cross trap. The second trap beam provides tight confinement in the axial direction of the first trap, producing a more localized trap, and one that is closer to isotropic in three dimensions.

2.4.3 Optical Lattice

Greater spatial control is sometimes needed than can be provided by a single focus trap. A number of more complicated trap geometries have been used for various applications. The most common by far, due to its simple setup and versatility, is the optical lattice. Optical lattices were first used in 1987 to direct and compress atom beams [53]. The first atom trap using an optical lattice was demonstrated by Westbrook et al. in 1990 [54].

A one-dimensional optical lattice can be formed by two counter-propagating single focus traps, focused at the same point, and can be implemented easily by retro-reflecting the original trapping beam. The interference between the two beams produces an axial trapping potential near the focus ($r/w_0 << 1$ and $z/z_R << 1$) given

by [50],

$$U(z) \approx -4U_0 cos^2(kz), \tag{2.22}$$

where $U_0 = U_{trap}$ is the maximum trap depth for the corresponding single focus trap given by Eq. (2.21). For a red detuned trap laser, the atoms are trapped at the antinodes of the standing wave, producing a lattice of trap sites with spacing $\lambda/2$, as depicted in Figure 2.4(b). Hence, the trapped atoms are extremely well localized in the axial direction. The trap is also four times as deep as a single focus trap using the same beam power, assuming that the standing wave is created by retro-reflecting the laser beam. These properties make the optical lattice a very powerful tool for a variety of applications, including coupling neutral atoms into a cavity mode [55, 56], studying quantum phase transitions in quantum gases [57], and creating quantum registers [19].

The one-dimensional optical lattice can be extended into multiple dimensions by adding additional beams. A three-dimensional optical lattice, which can be realized with three retro-reflected beams, provides a very large number of identical but spatially separated traps with extremely tight confinement ($\sim \lambda/2$) in all dimensions [54]. It also has the advantage that it produces stable trapping for either red detuned or blue detuned light. The advantages of blue detuned traps will be discussed later.

An important variant of the optical lattice is the optical conveyor [58]. For this, the counter-propagating trap beam is given a frequency shift, δ, relative to the other trap beam. This adds a time-dependent term to the potential,

$$U(z) \approx -U_0 cos^2(kz - \frac{\delta}{2}t), \tag{2.23}$$

which causes the interference pattern to 'travel' at a velocity of

$$v = \frac{\lambda\delta}{4\pi}. \tag{2.24}$$

By controlling the frequency difference, δ, this allows controlled translation of the atoms along the trap axis.

This technique was initially used to accelerate and launch clouds of atoms in atomic fountain applications [59, 60]. It was particularly useful for this purpose because it caused very little lateral heating. In 2001, the method was adapted for precision manipulation of trapped atoms [18, 58, 61]. Individual atoms or small groups of atoms could be moved along the lattice with minimal heating or loss, and while maintaining coherence [62]. Conveyors are useful for a number of applications, such as moving atoms into and out of a cavity [49] or rearranging atoms in a quantum register [63], and have even been applied to larger objects such as polystyrene beads [64].

2.4.4 Dipole Trap Frequency

Atoms confined in a trapping potential oscillate at a characteristic resonance frequency. This frequency depends on the position variation of the potential and can be different in each spatial dimension. Many heating and cooling effects depend critically on the frequency of these oscillations. Assuming that the atoms are near the center of the trap, a harmonic approximation can be used for the potential. For a single focus trap, the second order Taylor expansion gives

$$U(r,z) = -U_0 \left(1 - 2\left(\frac{r}{w_0}\right)^2 - \left(\frac{z}{z_R}\right)^2\right). \tag{2.25}$$

This leads to the trap frequencies,

$$\omega_r = \sqrt{\frac{4U_0}{mw_0^2}}, \tag{2.26}$$

$$\omega_z = \sqrt{\frac{2U_0}{mz_R^2}}. \tag{2.27}$$

In the case of the one dimensional optical lattice, the approximation of the potential is

$$U(r,z) = -U_0 cos^2(kz) \left(1 - 2\left(\frac{r}{w_0}\right)^2 - \left(\frac{z}{z_R}\right)^2\right). \tag{2.28}$$

For values of z near the focus, this gives frequencies of approximately,

$$\omega_r = \sqrt{\frac{4U_0}{mw_0^2}}, \tag{2.29}$$

$$\omega_z = 2\pi\sqrt{\frac{2U_0}{m\lambda^2}}. \tag{2.30}$$

Notice that these values are accurate only near the bottom of the trap. As the atoms become hotter, the anharmonicity of the trap becomes increasingly important, and the trap frequency deviates from this result. In most cases, the atoms are cold enough to make this approximation valid.

2.4.5 Localization of Trapped Atoms

The degree of localization of the atom in an optical trap depends on the temperature of the atom compared to the trap depth. For an atom with energy $E = \alpha U_0$, the furthest the atom can travel from the center of the trap will be the point where the trap depth is $U = (1-\alpha)U_0$. To determine the total confinement length in each direction, one can substitute this value into Eq. (2.20), giving:

$$(1-\alpha)U_0 = U_0\frac{w_0^2}{w^2}e^{-2r^2/w^2}. \tag{2.31}$$

If we assume that all of the energy is in the radial direction, then $z = 0$ and $w = w_0$. Eq. (2.31) then reduces to:

$$(1-\alpha) = e^{-2r^2/w_0^2}, \tag{2.32}$$

which can be rearranged to give:

$$r_{max} = w_0\sqrt{\frac{1}{2}\ln\left(\frac{1}{1-\alpha}\right)}. \tag{2.33}$$

If we assume that all of the energy is in the axial direction, then $r = 0$ and w is given by [52],

$$w = w_0\sqrt{1+\left(\frac{\lambda z}{\pi w_0^2}\right)^2}. \tag{2.34}$$

Substituting these into Eq. (2.31) gives:

$$(1-\alpha) = \frac{1}{1+\left(\frac{\lambda z}{\pi w_0^2}\right)^2}, \tag{2.35}$$

which can be rearranged to give:

$$z_{max} = \frac{\pi w_0^2}{\lambda}\sqrt{\frac{\alpha}{1-\alpha}}. \tag{2.36}$$

Under typical experimental conditions, $z_{max} >> r_{max}$ for a single focus trap.

The radial confinement in an optical lattice (at the focus) is the same as for the single focus trap. In the axial direction, the trap depth as a function of z is given in Eq. (2.22). If all of the energy is in the axial direction, this leads to:

$$1-\alpha = \cos^2(kz), \tag{2.37}$$

which can be rearranged to give:

$$z_{max} = \frac{\lambda}{2\pi}\sin^{-1}\left(\sqrt{\alpha}\right). \tag{2.38}$$

2.4.6 Differential Stark Shift

A dipole force trap relies on the spatially dependent energy shift created by the trapping laser. For a two level atom, the trap potential in the excited state is equal and opposite to the potential in the ground state. This produces a total shift in the transition frequency equal to twice the trap potential, as shown in Figure 2.5. This shift is known as the differential Stark shift.

Multi-level systems are more complicated, and there is usually no direct relationship between the trap potential in the ground state and the trap potential in the excited state due to contributions from a large number of different atomic transitions. Calculating the differential Stark shift requires first calculating the trap potential for both the excited state and the ground state, taking into account all applicable transitions. The difference between these two values gives the differential Stark shift in

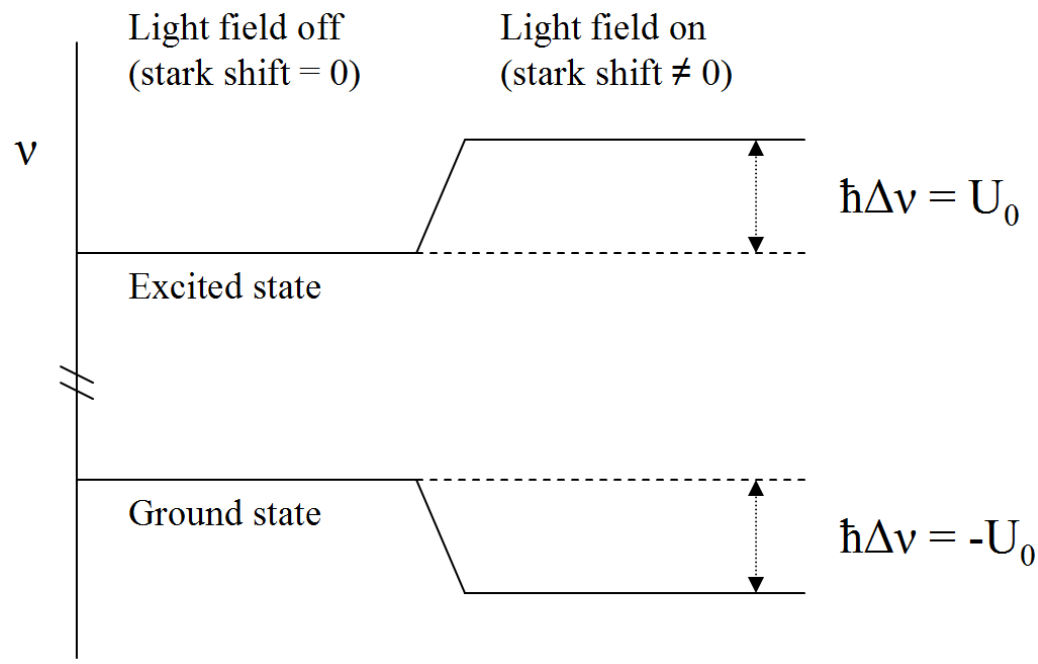

Figure 2.5: Stark shift for the excited and ground states of a two level atom.

terms of energy. The differential Stark shift is important because it adds an effective detuning to the resonance frequency of the transition.

Another important parameter is the differential Stark shift between the two hyperfine ground states. For many quantum information applications, coherence between the hyperfine ground states is crucial, and differential shifts in the ground state energy levels can cause decoherence. The shift can be calculated by taking the difference between the Stark shifts for each of the hyperfine states [65]:

$$\hbar\delta_{hfs} = U_0(\Delta) - U_0(\Delta + \omega_{hfs}), \tag{2.39}$$

where Δ is the detuning of the optical trap, and ω_{hfs} is the frequency spacing between the two hyperfine levels. For $\omega_{hfs} << \Delta$, this equation becomes [65],

$$\hbar\delta_{hfs} \approx \frac{\omega_{hfs}}{\Delta} U_0. \tag{2.40}$$

It is important to note that these equations give the maximum value of the Stark

shift, for the deepest point in the trap. As the atom oscillates in the trap, the differential Stark shift changes with the atom's position, producing a constantly changing resonance frequency. One strategy to compensate for the differential Stark shift of the optical transition is to create a dipole trap at a magic wavelength [66]. A magic wavelength occurs when contributions from multiple resonance frequencies create a trap potential that is equal in both the excited and ground states. A trap at such a magic wavelength produces no differential Stark shift. Because the differential Stark shift can increase decoherence [67], a magic wavelength can be particularly useful for quantum information experiments.

2.4.7 Calculation of Typical Values

All of the experiments described in this thesis use the ^{87}Rb D2 line at 780.241 nm for cooling, optical pumping, and detection of atoms. Atoms are cooled and detected using the $F = 2 \rightarrow F' = 3$ cycling transition. The red-detuned optical traps are created with a Yb fiber laser operating at 1064 nm. For an optical lattice with 1.7 W of power in each lattice beam, focused to 13 μm, the trap depth is approximately 2 mK (64 MHz) for the $5S_{1/2}$ ground state, and -2.9 mK (-91 MHz) for the $5P_{3/2}$ excited state. This leads to a differential Stark shift of 155 MHz for the D2 line. The differential Stark shift between the $F = 1$ and $F = 2$ ground states is 750 Hz. The trap frequencies are 843 kHz in the axial direction and 13.4 kHz in the radial direction. Both the trap depth and the differential Stark shift are linearly dependent on the trap power, while the trap frequency varies with the square root of the trap power.

CHAPTER III

QUBITS AND QUANTUM INFORMATION

Quantum computing requires quantum memory [68], and many physical systems are being pursued for storing quantum information, including ions [69], neutral atoms [19], and various solid state implementations [70]. Regardless of the method used, a quantum computer requires a large number of qubits, with minimal decoherence or loss for at least as long as it takes to perform a quantum operation. Figure 3.1 shows an illustration of a generic atomic quantum register.

This thesis focuses on developing improved neutral atom qubit storage and detection. The qubits are trapped using an optical lattice, with neutral ^{87}Rb atoms loaded from a magneto-optical trap. Major challenges include loading atoms reliably, holding atoms for a sufficiently long time, preparing a quantum state, and reading out the state without losing the atom from the trap. After briefly explaining the advantages of ^{87}Rb, each of these challenges will then be discussed in turn, beginning with loading atoms into a trap.

3.1 Choice of Qubit

The first important decision is the selection of the atomic element to be used as a qubit. To date, alkali atoms have been used exclusively for neutral atom qubit realizations. For these atoms, the single valence electron produces a reasonably simple energy level structure near the ground states. This simplicity makes alkali atoms much more convenient to work with than most other atoms. Although all alkali atoms have suitable electronic structure for realizing qubits, ^{87}Rb is particularly attractive. It has a strong cycling transition at 780.241 nm, which can easily be addressed with relatively cheap diode lasers. In comparison, sodium has its strongest transition at

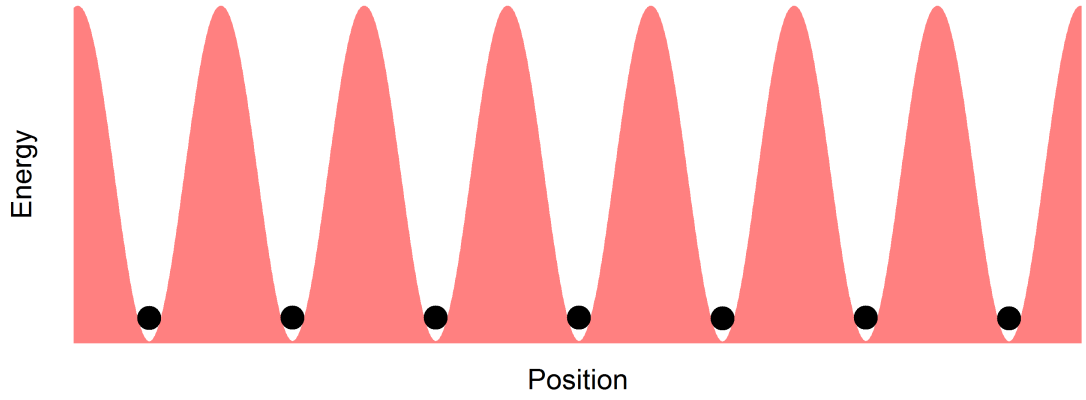

Figure 3.1: Illustration of a quantum register. A series of qubits are confined to evenly spaced traps in a periodic potential.

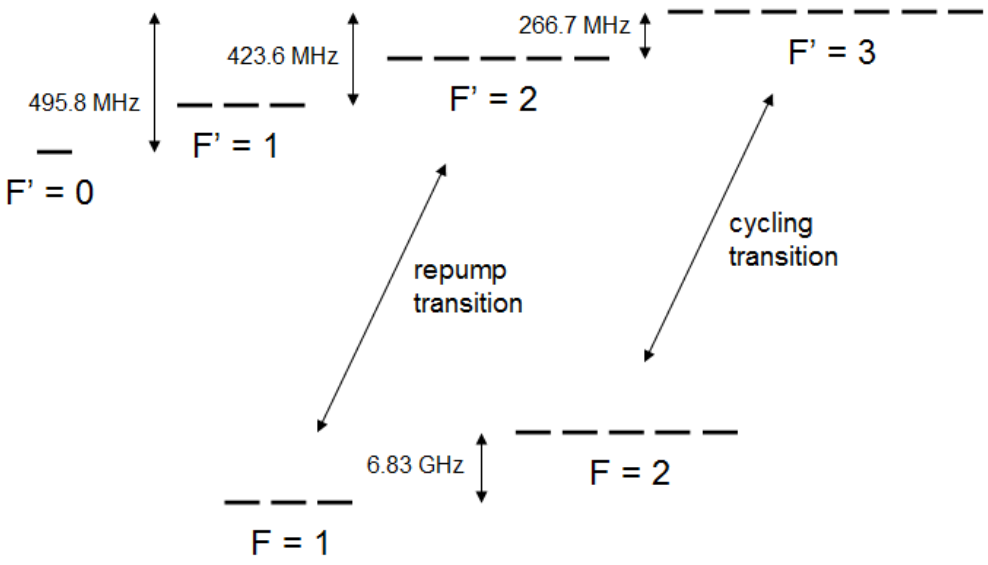

Figure 3.2: Hyperfine state diagram for the ^{87}Rb D2 line.

589 nm, which requires much more expensive lasers. Also, ^{87}Rb has half as many Zeeman ground states as cesium, making optical pumping somewhat simpler. ^{87}Rb has two hyperfine ground states and the $5P_{3/2}$ state has four excited states, along with several Zeeman sublevels, as shown in Figure 3.2 [71].

3.2 Loading a Quantum Register

Ideally, a quantum register should consist of an array of qubits, equally spaced and individually addressable. This array can occupy one or more dimensions [22, 25], but for simplicity the current discussion will be limited to one. It would, however, be fairly straightforward to scale up to higher dimensions. An optical lattice is one of the easiest methods to create a series of evenly spaced traps, and therefore seems ideal for this sort of application. The immediate difficulty, however, is in loading exactly one atom into each trap. This section will discuss how to load single atoms into a MOT, then into a lattice, and will finish by examining probabilistic versus deterministic loading schemes.

3.2.1 Single Atom MOT

In recent years, loading a single atom (or small number of atoms) into a MOT has become relatively commonplace. It was originally accomplished in 1994 by Hu et al. [16]. The MOT loading rate is given by [72],

$$R = \frac{1}{2} n v_c^4 V^{2/3} \left(\frac{m}{2 k_b T} \right)^{3/2}, \tag{3.1}$$

where V is the volume of the MOT and v_c is the maximum capture velocity. There is no exact analytical solution for the capture velocity, but approximate relationships can be derived in the limits of low and high magnetic field gradient. For a small magnetic field gradient, the volume and capture velocity of the MOT depend primarily on the beam diameters. It is assumed that any atom which enters the molasses and is slowed to the minimum temperature will become trapped. For beam diameter d, $V \approx 1/6\pi d^3$

and $v_c^2 \approx 2v_r\Gamma d$ [73], where v_r is the photon recoil velocity. This results in a loading rate,

$$R \propto d^4. \tag{3.2}$$

The other important limit is for a high magnetic field gradient. In this case, not all atoms which are slowed by the molasses beams become trapped. Since the molasses area is large compared to the effective trapping area, the trap volume and capture velocity depend primarily on the magnetic field gradient. For a magnetic field gradient B', $V \propto B'^{-3}$ and $v_c \propto B'^{-2/3}$ [74]. The resulting loading rate scales as:

$$R \propto B'^{-14/3}. \tag{3.3}$$

This relationship between the magnetic field gradient and the loading rate provides a simple method for loading a small number of atoms. By increasing the gradient, the loading rate can be reduced enough to (probabilistically) load only one atom in a specified amount of time [17]. This atom can then be transferred into an optical lattice by overlapping the two traps. Although this is an effective way to probabilistically load a single atom, it does not easily extend to loading a uniform chain of atoms. Additional techniques are needed to produce an evenly spaced chain.

3.2.2 Sparse Loading

The simplest method to load an array of atoms is to sparsely load a string of atoms probabilistically. If even spacing between atoms is not required, this method produces an addressable quantum register with the minimum possible effort. Unfortunately, this method scales poorly. As the number of atoms increases, the chance of two atoms occupying the same lattice site grows quickly. An improvement on probabilistic loading involves active relocation of individual atoms in the lattice. Miroshnychenko et al. demonstrated in 2006 [63] that sparsely loaded atoms in a one dimensional optical conveyor can be actively repositioned using a second, orthogonal optical conveyor.

This produces evenly spaced atoms, but it still scales poorly with large atom number, since it relies initially on sparse loading.

3.2.3 Collisional Blockade

A second loading scheme depends on the collisional blockade mechanism to load individual atoms into approximately half of the lattice sites, with zero atoms in the other sites. A collisional blockade was demonstrated in a single focus trap in 2002 [48], and has since been used in a three dimensional optical lattice [25]. In an optical trap, the rate of collisions varies inversely with the trap volume. If this rate is high enough, then whenever a second atom enters the trap, collisions will occur very quickly. In the absence of near-resonant light, these collisions are mediated by the relatively weak Van der Waals force ($F \propto 1/r^6$) [75]. These elastic collisions are very unlikely to cause atoms to leave the trap. If near-resonant light is present, however, inelastic three-body collisions between the two atoms and a photon can occur. These collisions can result in a large change in the kinetic energy of each atom, and will frequently cause both atoms to be ejected from the trap. This provides a simple method to obtain single occupation of half of the lattice sites. However, unoccupied lattice sites are arranged probabilistically, and there is no easy way to fill the remaining lattice sites. One possible compacting scheme has been proposed by Vala et al., but has not yet been realized experimentally [76].

3.3 Atom Lifetime

Most neutral atom traps exhibit a characteristic lifetime, defined as the time required for the population to drop by a factor of $1/e$. Several different loss mechanisms must be minimized in order to retain the atoms as long as possible. Important loss mechanisms include off-resonant scattering from the optical trap laser, heating from trap fluctuations, and collisions with background gas.

As discussed earlier, off-resonant scattering can be minimized by using a far off

resonant trapping laser. At sufficient detuning, the resulting heating can be easily rendered negligible compared to other loss mechanisms, such as background collisions and dipole trap fluctuations [42]. Using standard UHV vacuum techniques, background pressures below 10^{-11} Torr can reasonably be achieved [77]. These low pressures allow lifetimes in excess of 300 seconds [51]. Another source of loss, trap fluctuation heating, has been analyzed by Savard et al. [78]. Random fluctuations in the intensity and positioning of the optical trap laser can cause significant heating, which may limit trap lifetimes to as little as several seconds. These effects will be discussed in greater detail later.

3.4 State Preparation

A neutral atom qubit must have at least two states, designated $|0\rangle$ and $|1\rangle$, which are stable on the time scales of the experiment. One must be able to prepare the atom in either of these two states, or in an arbitrary superposition of the two. For this work involving ^{87}Rb, the $F = 1, m_F = 0$ and $F = 2, m_F = 0$ ground states will be designated as $|0\rangle$ and $|1\rangle$ respectively.

The $F = 1$ and $F = 2$ states can be initialized by direct excitation of an appropriate optical transition, with error rates $<< 1\%$ [79]. Initialization to a specific m_F state is considerably more difficult, although it can still be achieved through optical pumping [80]. Once the atom is initialized to either $|0\rangle$ or $|1\rangle$, coherent superpositions can be created using Raman [81] and microwave transitions [82]. Of these, microwave transitions provide the easiest and most direct method of preparing the atomic state. This section will examine the theory behind microwave state preparation and explain how it is used experimentally.

In order to examine the effect of microwaves on atoms in the ground state, two assumptions will be made. The first assumption is that the atom has only two relevant energy levels. In our case, the two levels will be $F = 1, m_F = 0$ and $F = 2, m_F = 0$.

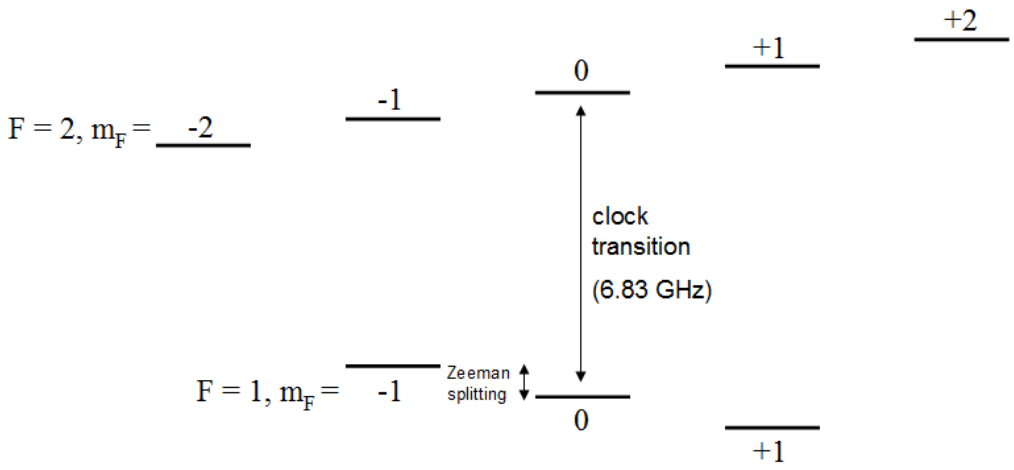

Figure 3.3: ^{87}Rb hyperfine ground states, showing Zeeman splitting. The $F = 1, m_F = 0 \rightarrow F = 2, m_F = 0$ transition is known as the clock transition.

This assumption is reasonable as long as there is a magnetic field present to lift the degeneracy of the Zeeman sublevels. The relevant levels and sublevels are shown in Figure 3.3. The second assumption is that the microwaves are tuned very close to the resonant frequency ($\Delta = 0$).

The transition in question is a magnetic-dipole transition, so the strongest non-vanishing effect is magnetic. In the presence of a constant-magnitude AC magnetic field $\vec{B} = B\hat{x}$, and in the presence of decoherence mechanisms, the two-level atom's response can be characterized by the optical Bloch equations [65], given by [82, 83]:

$$\dot{u} = -\Delta v - \frac{u}{T_2}, \tag{3.4}$$

$$\dot{v} = \Delta u - \frac{v}{T_2} + \frac{ge}{2m} Bw, \tag{3.5}$$

$$\dot{w} = -\frac{w - w_{eq}}{T_1} - \frac{ge}{2m} Bv, \tag{3.6}$$

where Δ is the detuning of the magnetic field from resonance, T_1 is the relaxation time, T_2 is the dephasing time, g is the Landé g-factor, e/m is the charge to mass ratio of an electron, and (u, v, w) is the Bloch vector. The value of the Bloch vector is $(0, 0, -1)$ or $(0, 0, 1)$ for the $|0\rangle$ and $|1\rangle$ states respectively [65]. For microwave

transitions in a dipole trap, T_1 is due primarily to off-resonance scattering from the dipole trap laser, and is thousands of times larger than T_2 [65]. For this reason, the first term in Eq. (3.6) can safely be ignored. In red-detuned dipole traps, T_2 is due primarily to the differential AC Stark shift between the hyperfine ground states [65]. Setting $\Delta = 0$ and solving for w gives [82, 84]:

$$w(t) = \left(C_1 \cos(st) + \frac{C_2}{s} \sin(st) \right) e^{bt}, \tag{3.7}$$

$$C_1 = w_0, \tag{3.8}$$

$$C_2 = w_0 \left(\frac{1}{2T_2} \right) - \frac{ge}{2m} B v_0, \tag{3.9}$$

$$b = \frac{1}{2T_2}, \tag{3.10}$$

$$s = \sqrt{(\frac{ge}{2m}B)^2 - \left(\frac{1}{2T_2} \right)^2}. \tag{3.11}$$

Assuming that the atoms begin in the $F = 1, m_F = 0$ state, then $w_0 = -1$ and $v_0 = 0$. Furthermore, for large magnetic fields such that $\frac{ge}{2m}B >> 1/T_2$, the equations simplify to:

$$w(t) = -\left[\cos(\frac{ge}{2m}Bt) + \left(\frac{1}{\frac{ge}{m}BT_2} \right) \sin(\frac{ge}{2m}Bt) \right] e^{-\frac{1}{2}\left(\frac{1}{T_2}\right)t}. \tag{3.12}$$

Since $\frac{ge}{2m}BT_2 >> 1$, the sine term is small, and in most cases can be ignored. This gives us the final equation for the population inversion:

$$w(t) = -cos(\Omega t) e^{-\frac{t}{\tau}}, \tag{3.13}$$

where $\Omega = \frac{ge}{2m}B$ is the Rabi frequency and $\tau = T_2$ is the coherence time.

This is simply the formula for a damped cosine function. Figure 3.4 shows a graph of the population inversion versus time for the case of $\Omega = 5/\tau$. If the magnetic field is applied for precisely $\Delta t = \pi/\Omega$ (referred to as a π pulse), then the atom will be transferred into the other state with near unit efficiency, limited only by the

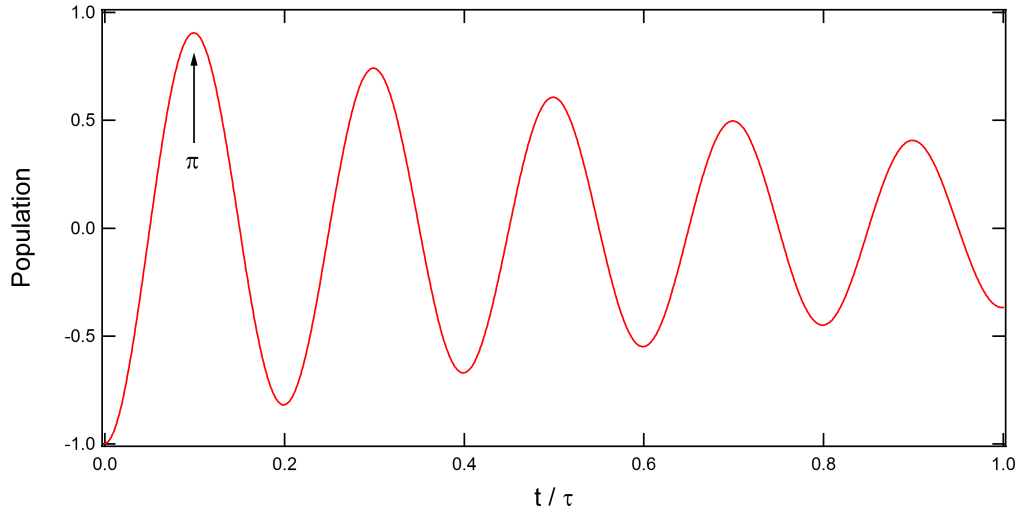

Figure 3.4: Population versus microwave pulse length, for $\Omega = 5/\tau$. Maximum population transfer is achieved by applying a π pulse.

decoherence during the pulse. Further, any arbitrary superposition between the two states is achievable by applying a pulse of the appropriate length.

The microwave pulse has a Fourier-limited linewidth inversely related to the pulse length [83]. For pulses on the order of 1 ms, this yields a linewidth of ∼1kHz. Since a 1 mG magnetic field produces Zeeman shifts of 700 Hz [85], multiple Zeeman states can be addressed only if the magnetic fields are very carefully minimized. In general, due to the effects of stray magnetic fields, microwaves typically address only a single Zeeman sub-state.

3.5 State Readout

Another requirement for any quantum information system is a reliable mechanism for reading out the states of the qubits. The most common method is to pulse a high power kickout beam tuned to the $F = 2 \rightarrow F' = 3$ resonance [20, 62, 65, 86, 87, 88]. This removes all of the atoms that are in the $F = 2$ state from the trap, as shown in Figure 3.5. The trap is then imaged, and any qubits that remain are assumed to have been in the $F = 1$ state, while the missing qubits are assumed to have been

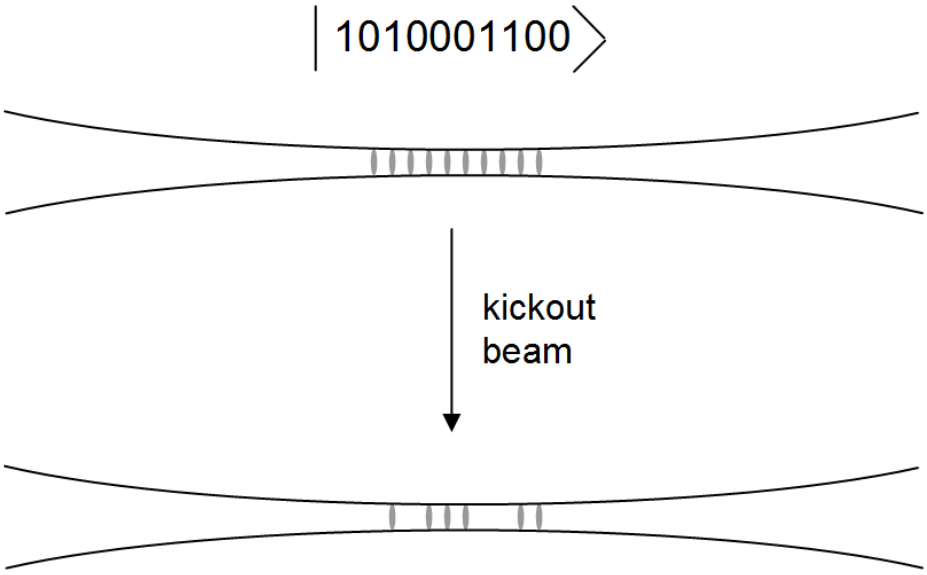

Figure 3.5: Illustration of destructive state detection. A kickout beam tuned to the $F = 2 \rightarrow F' = 3$ resonance knocks all of the atoms in the $F = 2$ ($|1\rangle$) state out of the trap, while atoms in the $F = 1$ ($|0\rangle$) state remain.

in the $F = 2$ state. Destructive readout has been used in every neutral atom qubit experiment to date. This method is fairly reliable, with error rates typically below 1%, but it has the obvious limitation that it destroys the quantum register after every readout.

One solution that has been demonstrated is to use a cavity QED system to increase the collection efficiency of the scattered photons [56, 89, 90, 91]. The quantum state can then be determined with fewer scattering events, resulting in lower heating and minimal loss of the qubits. A drawback of this approach is that cavity QED systems significantly complicate the experimental setup, and each atom to be detected needs to be localized within the small cavity mode. These limitations make a free space solution seem preferable. Direct fluorescence state detection should be possible, but has never before been demonstrated. This is due primarily to the difficulty of capturing and observing sufficient fluorescence without the aid of a cavity. Nevertheless, it is achievable with a high aperture lens and high efficiency detectors, as will be seen

later.

3.6 Repetition Rate

Each implementation of a quantum register has four important properties that largely determine its efficacy. The first property is the amount of storage space. Since 1-D optical lattices can easily have hundreds of lattice sites, and lattices can be extended in multiple dimensions, space limitations will not be a major concern for quite some time. The second property is the overall error rates of state preparation and detection. These error rates are frequently below 1% [19], which is low compared to the errors introduced during quantum gate operations [22]. The third important property is the total repetition rate for quantum operations. The quantum operations themselves are usually very fast, $t << 1$ ms. Initializing a quantum register can also be completed on the order of a millisecond or faster. However, loading a quantum register takes much longer. Depending on the method used, it can take as long as several seconds, and may be a probabilistic process [19]. Some groups have achieved faster results, on the order of a few hundred milliseconds, but at the cost of limited expandability [22].

The final issue is the stability of the trapped qubits. The loss rate of qubits from the register is important, particularly as the number of qubits increases. For example, reliably maintaining 100 atoms for 1 s in a quantum register would require a trap lifetime of over 150 seconds. Furthermore, these qubits must be able to maintain their quantum state for long enough to perform the desired quantum operations. For a red detuned optical lattice, coherence times around 20 ms have been measured [65]. A major factor that is currently believed to limit coherence times is the fluctuation of the differential Stark shift between hyperfine ground states (Eq. (2.40)) as the atom moves in the trap [65, 67]. Depending on the speed of the quantum operation, these limits on coherence time may or may not present a problem in the future.

The need to prepare a new quantum register for every calculation has thus far limited the repetition rate for neutral atom quantum operations to about one per second [22]. By switching to a non-destructive readout scheme, this rate could be increased by at least an order of magnitude. A robust, easily implemented non-destructive readout system would be extremely valuable for future quantum computing experiments. There are many experimental challenges involved in non-destructive readout. The next few chapters describe the experimental processes used to realize such a scheme.

CHAPTER IV

EXPERIMENTAL SETUP

All of the experiments reported in this thesis require a vacuum chamber, imaging system, magneto-optical trap, and dipole trap. This chapter focuses on the basic infrastructure and setup which are pre-requisite to the work presented in subsequent chapters.

4.1 Vacuum Chamber

The experiments are conducted in a vacuum chamber built mostly out of standard, off-the-shelf pieces. Atom trapping takes place inside a rectangular quartz cell made by Allen Scientific Glass. The cell measures 27 by 27 by 150 mm and is attached to the vacuum chamber through a round glass transition piece fitted with a standard vacuum flange. This in turn is attached to the main body of the vacuum chamber. The setup is illustrated in Figure 4.1.

A Rb getter from SAES Getters is mounted to a feedthrough inside the vacuum chamber, with the active area pointed towards the trapping region. The getter is a filament with a small amount of a rubidium compound deposited on one side. An electric current is applied across the getter, which heats the active region, causing part of the compound to dissociate and release Rb atoms.

An ion gauge is attached to the system to continuously measure the vacuum pressure. For our experiments, the operating pressure is below the minimum pressure of the ion gauge (10^{-11} Torr), however, the gauge is used during the initial pumping out of the chamber and to indicate if the pressure is abnormally high. The ion gauge is turned off when minimum pressure has been reached.

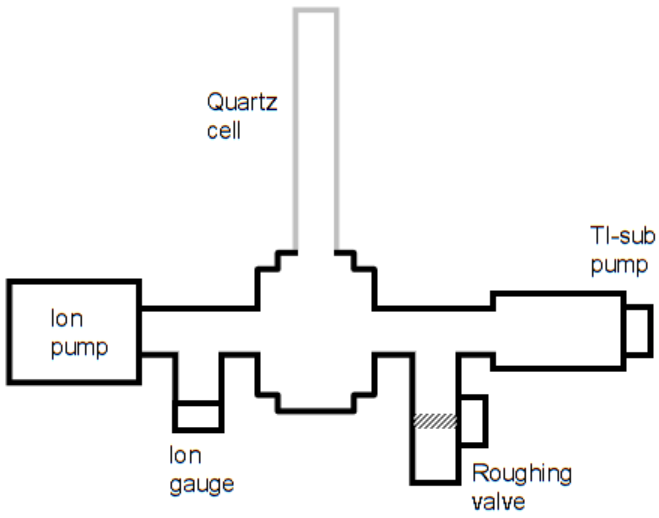

Figure 4.1: Representative diagram of the vacuum chamber used in these experiments. A quartz cell is attached to a steel chamber, which features a Rb getter, an ion gauge, an ion pump, and a titanium sublimation pump. For initial pumpout, the chamber is attached to a pumping station through the roughing valve.

The vacuum system uses four pumps to reach ultra high vacuum (UHV) pressures. An ion pump and a titanium sublimation pump are permanently attached to the system. The other two (the roughing pump and the turbo pump) are attached temporarily. The roughing pump is turned on first and is able to reach pressures around 10^{-2} Torr. The turbo pump further reduces the pressure to around 10^{-9} Torr. With the chamber connected to these pumps, the chamber is baked at a temperature of 400 ° C for approximately two weeks. This removes nearly all water from the system, as well as most other impurities.

Following the bakeout, the ion pump is turned on, and the roughing and turbo pumps are disconnected from the system. The ion pump utilizes electrons emitted from an anode to ionize passing atoms, which are then accelerated toward a titanium cathode using a strong electric field. The atoms form stable compounds with the titanium on the cathode surface, while also spreading titanium atoms onto nearby

surfaces [92]. The total pumping rate depends on the mass of the gas particles being pumped. Under most circumstances, the ion pump runs continuously, and in the absence of hydrogen, it can typically maintain a pressure as low as 10^{-11} Torr. It is relatively poor at removing hydrogen, however, due to its low mass.

A titanium sublimation (TI-sub) pump is used to remove the hydrogen in the system. The TI-sub pump is made up of titanium filaments mounted inside a large vacuum nipple. When current is applied to the filaments, titanium is ejected, coating the inside wall of the nipple with a thin layer of titanium. Hydrogen (along with several other elements) reacts with the titanium, effectively removing it from the system. The TI-sub pump is not run continuously. Instead, it is pulsed on for a short period of time every few months, or if the vacuum starts to become poor. Working together, these pumps are able to reliably maintain pressures below 10^{-11} Torr, as required for our experiment.

4.2 Magneto-Optical Trap

We use a MOT for initial cooling and trapping of ^{87}Rb atoms. Creating the MOT requires two primary components: a magnetic field gradient and cooling lasers. The MOT setup is shown in Figure 4.2.

4.2.1 Magnetic Gradient

The magnetic field is supplied by a pair of wire coils made from bare copper refrigerator tubing wrapped with kapton tape. The tubing has an outside diameter of 0.25" and an inside diameter of 0.19". Each coil has a total of 40 turns, wrapped tightly in five layers of eight turns each. The inner diameter of each coil is 2.5". The coils are placed on either side of the glass cell, 1.5" apart with their shared axis parallel to the table. A 15 kW power supply is attached to the coils, generating a maximum current of 320 A, which produces a maximum magnetic field gradient of 400 G/cm near the center of the glass cell. The coils are cooled by running chilled water through the

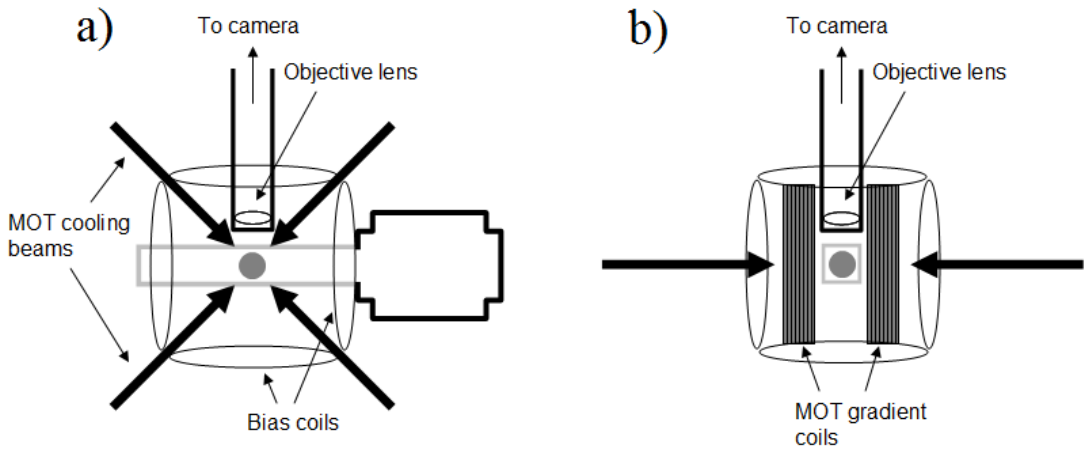

Figure 4.2: Diagram of the magneto-optical trap (MOT) setup. The MOT is created by shining cooling light from six directions, all of which cross in the center of the glass cell. Two large coils of refrigerator tubing create the necessary magnetic field gradient, while six smaller coils of wire control the bias field.

hollow center of the refrigerator tubing to dissipate the heat.

Six bias coils are placed surrounding the trap (one pair in each direction), and are used to counteract the earth's magnetic field as well as stray magnetic fields from nearby electronics, magnets, and other sources. Each coil is made up of 20 turns of thin wire.

4.2.2 Cooling Lasers

The cooling lasers comprise two 780.241 nm wavelength diode laser systems, each tuned to a different ^{87}Rb D2 transition. The trapping laser is tuned near the cycling transition ($F = 2 \rightarrow F' = 3$), while the repump laser is tuned to the $F = 1 \rightarrow F' = 2$ transition. Both lasers are locked to their respective transitions using saturated absorption spectroscopy. Fine control of the laser power and frequency is obtained through the use of acousto-optic modulators (AOMs). Additionally, either laser can be blocked completely using a mechanical shutter.

Both laser systems employ a master-slave configuration, with a grating-stabilized

master laser and an injection-locked slave laser. All of these lasers use the Sharp Electronics, model GH0781JA2C laser diode, and are controlled using homemade electronics. The master lasers are set up in the Littrow configuration [93].

The laser diodes are powered by a stable current control circuit based on a design by Libbrecht and Hall [94]. A modulation input allows fast feedback to the current for locking and stabilization. Temperatures are stabilized using a thermo-electric cooler (TEC) attached to the aluminum housing. The temperature of the diode is monitored using a thermistor, and a PI (proportional/integral) locking circuit controls the TEC. The temperature control circuit is based on a design by Hulet's group [95].

Each master laser is locked to its respective transitions using saturated absorption and FM spectroscopy techniques. A small portion of the light from the laser is redirected and split into two beams, which act as a pump and probe beam respectively. These beams counter-propagate through a Rb vapor cell, and the probe is focused onto a photodiode. This produces a saturated absorption signal. In order to obtain a dispersion signal, the pump beam is modulated using a 210 MHz AOM, and the modulation signal is mixed with the signal from the photodiode. The resulting signal is low-pass filtered to remove high frequency oscillations. These techniques are described in much greater detail in Refs [96, 97].

The lasers are locked to the dispersion signal using a home-built lockbox. The lockbox amplifies the dispersion signal and creates separate proportional and integral outputs. The proportional output is connected to the modulation input on the current controller. The integral output controls the precise position of the laser's diffraction grating through the use of a PZT.

Light from the trapping master is double-passed through a variable frequency AOM. This allows the final frequency of the trapping light to be tuned from about -50 MHz to $+10$ MHz relative to the cycling transition. Light from the master trapping and repump lasers is then used to injection lock the slave lasers. Each

resulting laser beam passes through an AOM, which allows fast control of the laser power, and a shutter, which allows the beam to be completely blocked.

Polarizing beam splitter cubes are used to split the trapping laser beam into three beams of roughly equal power. The repump beam is then combined with one of the three trapping laser beams. Each beam is then split one additional time, producing six trapping beams. Using quarter wave plates, the beams are given the appropriate circular polarizations, and oriented in a standard six beam MOT configuration, with all beams overlapping at the center of the magnetic coils. The trapping and repump beams have a maximum diameter of 11 mm, which can be reduced to as small as 1 mm. The total power in each beam is 3 mW (4 mW for the repump), which gives a total maximum intensity of 10 mW/cm^2 (4.5 mW/cm^2 for the repump).

4.2.3 Single Atom MOT

To form the MOT, the trapping laser is detuned slightly to the red of transition ($\delta = -10$ MHz), the magnetic gradient is set fairly low ($\sim$40 G/cm), and a 2 A current is applied to the getter. This produces a MOT with a steady state population of $>$10,000 ^{87}Rb atoms.

In order to operate the MOT in the single atom limit, several different approaches are used to reduce the number of atoms in the trap. First, the rubidium vapor pressure is lowered by shutting off the getter and leaving it off for several weeks. On occasions where a higher rubidium vapor pressure is needed, an ultraviolet LED is shone on the glass cell, which temporarily increases the amount of rubidium gas in the cell by light induced desorption of rubidium from the glass walls [98]. Once the light is shut off, the rubidium quickly bonds to the cell again, returning the pressure to its previous value (the response time is less than a second). The UV light produces a much lower rubidium vapor pressure than the getter, but it still allows for loading several thousand atoms.

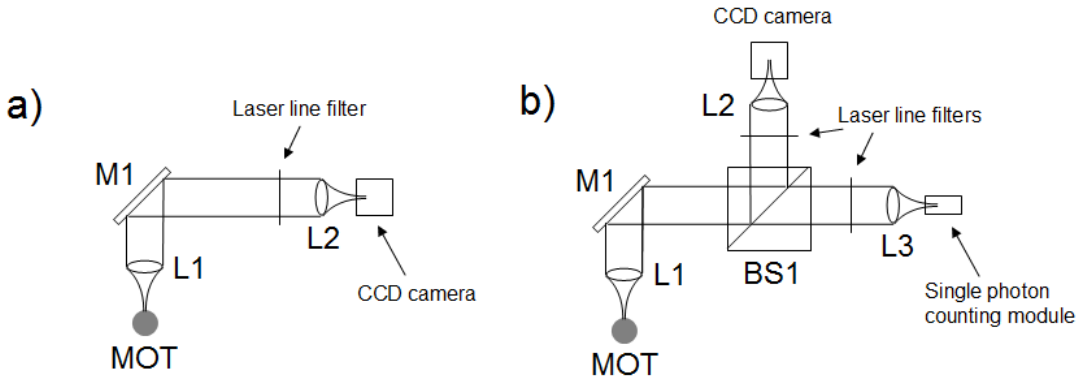

Figure 4.3: Diagrams of the primary imaging systems. (a) Light from the trapped atoms is captured by objective lens L1 (f = 10 mm), passes through a laser line filter, and is focused onto a CCD camera by lens L2 (f = 75 mm). Total capture and detection efficiency is 2.9%. (b) Light from the trapped atoms is split by the pick-off beam splitter BS1 (R = 5%). A small amount of light is focused onto the camera by lens L2 (f = 75 mm). The rest of the light is focused onto the single photon counting module by lens L3 (f = 25 mm). Total efficiencies are 0.14% and 1.5% for the camera and the photon counter, respectively.

The loading rate is further reduced by changing the magnetic field gradient and the trapping laser beam diameters. Increasing the magnetic field gradient decreases both the MOT loading rate and the MOT diameter [74, 99]. This method has been used by Frese et al. in their single atom trapping experiments [17]. Decreasing the trapping beam diameters also decreases the loading rate [73], but makes precise alignment of the beams much more critical. If necessary, the trapping laser detuning can be used to change the loading rate of the MOT, but this will also affect the minimum temperature of the atoms in the MOT.

4.3 Imaging System

Fluorescence imaging is used to detect the atoms in the trap. The imaging setup is shown in Figure 4.3(a). To capture light from the atoms in the trap, a 20X microscope objective (Mitutoyo M Plan NIR 20X) is mounted directly above the glass cell, focused

on the center of the MOT. The objective lens has a numerical aperture of 0.4, an effective focal length of 10 mm, and a working distance of 20 mm. It captures about 4% of the fluorescence from the trapped atoms. In most cases, this light is then directed through a laser line filter (>90% efficiency) and to an Andor back-illuminated CCD camera. The camera has a quantum efficiency of 80%, resulting in a total system efficiency of 2.9%. The total magnification of the system is 7.5X, creating a field of view of just under 1.1 mm on the 8.2 mm square camera sensor.

CCD cameras are useful for detecting the presence of single atoms and for measuring the trap population. However, most of these cameras have a readout noise level of at least five counts per pixel, which renders any signal smaller than around twenty counts difficult to detect. Nondestructive state measurements will require detecting signals as small as a few photons. For these measurements, a PerkinElmer single photon counting module (model SPCM-AQR-14) is used in addition to the camera, as shown in Figure 4.3(b). The single photon counting module has an efficiency of 45% and an intrinsic noise level (dark count) of <100 counts per second.

4.4 Dipole Trap

The atoms in the MOT are transferred to an optical dipole trap. The dipole trap is generated using a single mode 1064 nm Ytterbium fiber laser (IPG Photonics YLR-10-1064-LP-SF-G) with 10 W maximum optical power. The beam is shaped by passing it through an optical fiber, which limits the maximum usable power to 4 W. The beam is then focused onto the center of the MOT. The experiments in this thesis use a few different trap configurations. The most typical configuration, a retro-reflected optical lattice, is shown in Figure 4.4. Other setups include a single focus trap, an optical conveyor, and dual lattices.

The single focus trap setup uses a single 4 W beam focused to a minimum waist $w_0 = 13$ μm (Figure 4.4 with the retro-reflection beam blocked). This setup is very

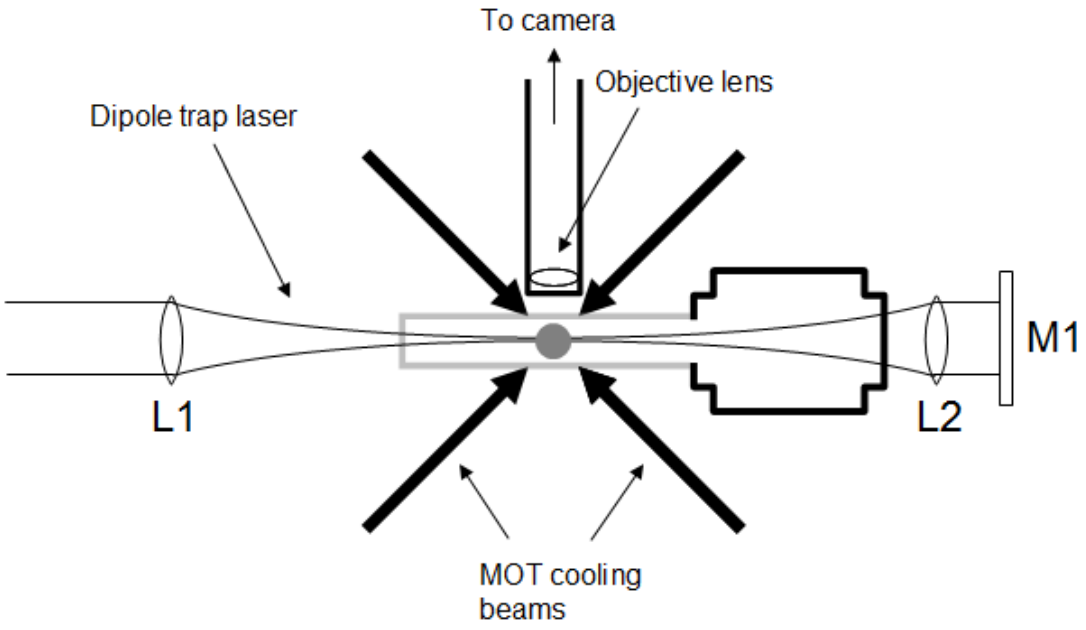

Figure 4.4: Diagram of the optical lattice setup. The trapping laser is focused through lens L1 (f = 300 mm) onto the center of the MOT ($w_0 = 13$ μm). The laser is collimated by lens L2 (f = 300 mm) and then retro-reflected by mirror M1. When creating a single focus trap, the retro-reflection is blocked.

simple, but has several drawbacks. The atoms are not very tightly trapped, and there is no easy way to limit the trap to a single atom. Furthermore, a single focus trap produces only a single trapping site. It is used primarily for diagnostic purposes and as an initial step toward creating an optical lattice. For the optical lattice setup, the beam power is lowered to 2 W or less in order to prevent a misaligned retro-reflected beam from damaging the optical fiber.

CHAPTER V

HEATING AND COOLING OF SINGLE ATOMS

In early work with optical dipole traps, trap lifetimes were limited primarily by heating due to off-resonant absorption of trap light [42]. However, even with the advent of far off-resonance trapping beams, significant heating rates remained [100]. It was later suggested that fluctuations in the trap potential due to laser intensity noise and pointing instabilities can cause significant heating, which can reduce the lifetime of optically trapped atoms [78]. However, only a few efforts have been made to quantitatively study this heating experimentally [101, 102]. It is particularly important to study heating in optical lattices, since the heating rates scale strongly with the trap frequencies [78], which are typically much higher in optical lattices. While trap lifetimes exceeding 300 s have been observed in low frequency optical traps [51], the longest previously reported lifetime in an optical lattice is around 60 s [63].

This chapter examines heating and cooling in an optical lattice and quantifies the effects on the trap lifetime. First, the trap lifetime is measured in the absence of cooling, revealing a nonexponential decay of the population with an asymptotic lifetime of 62 s. Next, heating due to trapping laser fluctuations is examined experimentally, producing good quantitative agreement with a numerical simulation. In order to counteract this heating, continuous cooling is applied to the atoms, extending the lifetime dramatically. Finally, a lattice lifetime of >300 s is demonstrated by using a pulsed cooling technique, with a cooling pulse applied once every 20 s. A variation on this scheme is proposed for use with qubits.

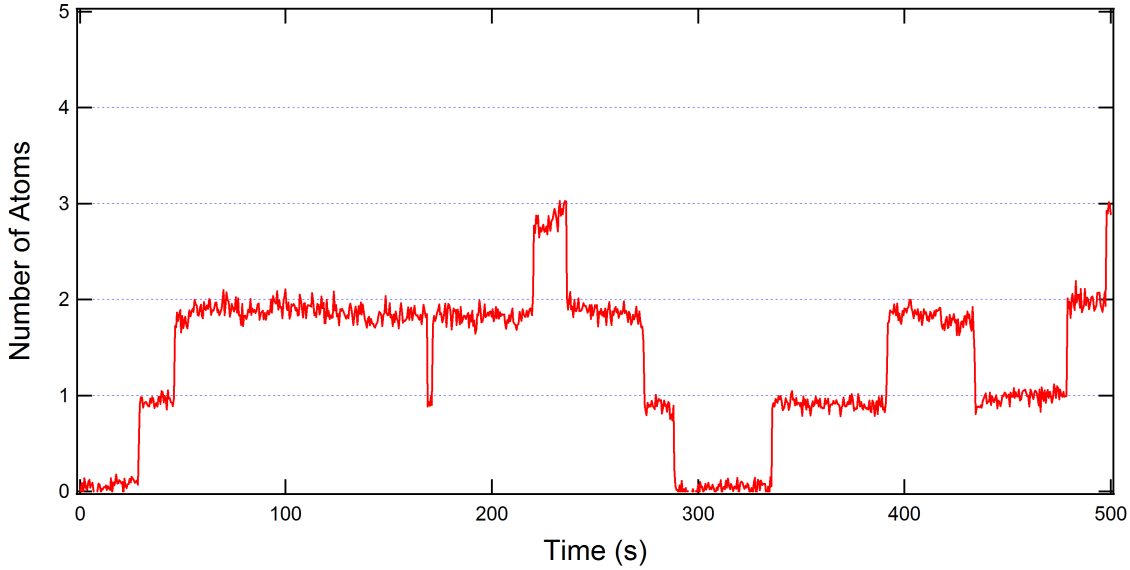

Figure 5.1: Fluorescence level of the MOT over time. Distinct jumps in the fluorescence can be seen as atoms enter and leave the trap. Exposure time is 0.2 s. Each atom produces a signal of 1700 counts (8500 cts/s), with a background level of 3570 counts, primarily due to light scattering off of the glass cell.

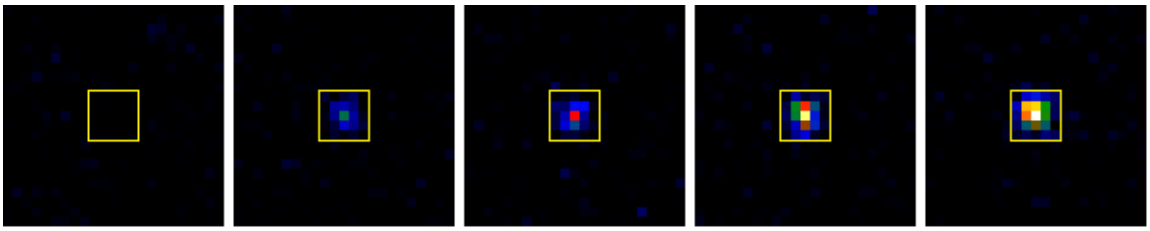

Figure 5.2: CCD camera images of a low atom number MOT. From left to right, the images show zero, one, two, three, and four atoms loaded. Exposure time is 0.7 s. The yellow box shows the 25 pixel area of interest.

5.1 Single Atom MOT

First, a small number of atoms are loaded into the MOT using 3 mm trapping beams, a 400 G/cm magnetic field gradient, and trapping beam detunings of -20 MHz. These parameters yield a loading rate of approximately one atom every 60 s. Figure 5.1 shows the fluorescence level in the trap with respect to time, over a period of 500 seconds. The exact number of atoms in the trap can be ascertained up to at least five by the discreet levels of fluorescence. Figure 5.2 shows images of different numbers of atoms taken with the CCD camera. These pictures were taken at a 700 ms exposure time, and give a signal per atom of about 6000 counts (8500 cts/s). This is about 25% lower than our predicted signal of 11,000 cts/s.

5.2 Optical Lattice

The optical lattice is formed by a single 1 W, 1064 nm, retro-reflected beam, focused to 13 μm. This produces a trap with individual lattice sites separated by 532 nm. Because the resolution of the imaging system is 2 μm, the individual lattice sites cannot be resolved. Loading into any given lattice site is entirely probabilistic, and the location of each atom can only be determined within a few sites.

Atoms are loaded into the optical lattice from the MOT. The lattice beams are aligned such that the focus is at the center of the MOT. Once the lattice beams are turned on, the atoms in the MOT are pulled toward the maxima of the light field and become trapped. After a short wait (less than 1 s), the magnetic gradient coils and the MOT light are turned off, leaving the atoms confined in the optical lattice.

The transfer efficiency between the MOT and the lattice is measured by repeatedly transferring the same atoms from the MOT to the lattice and back. Assuming that the transfers happen much faster than the loading rate of the MOT, the chance of loading additional atoms during the measurement is small. For small numbers of atoms ($\sim$1-3), our trap exhibited an overall transfer efficiency of approximately 97%.

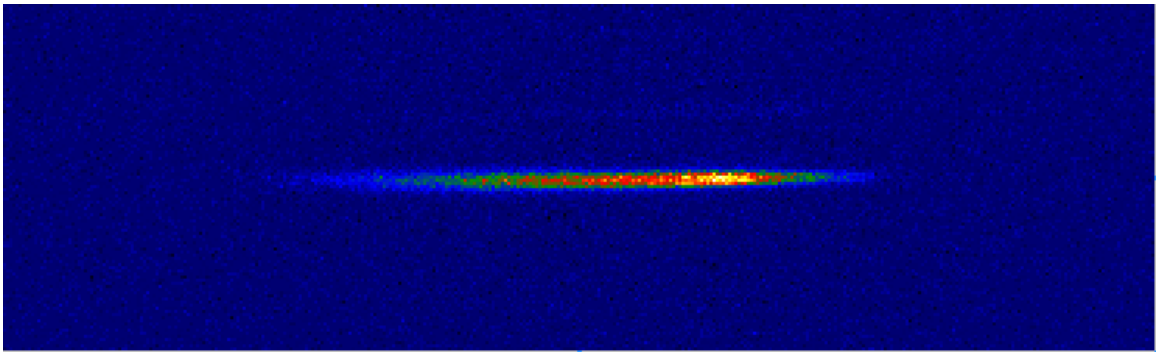

Figure 5.3: Several thousand atoms in an optical lattice. The atoms were imaged destructively, using the horizontal MOT beam as an on-resonance probe, with a 1 ms probe time.

As the number of atoms increased, the transfer efficiency dropped, possibly due to light assisted inelastic collisions or mismatched overlap of the traps.

5.3 Continuous Observation

Atoms in optical traps are typically detected through a destructive imaging process (see Figure 5.3) [103]. The trap is turned off, and an on-resonance probe beam excites the atoms, causing them to fluoresce. This fluorescence is captured by the camera. This method has several advantages. It is fairly straightforward to implement, and the probe time is typically short enough (less than 1 ms) to effectively freeze the motion of the atoms. It can therefore be used to measure the temperature of the atoms in the trap via measurements of the expansion of the atom cloud. Unfortunately, this method also has a few drawbacks. Most obviously, it causes all of the atoms to leave the trap. Also, the short exposure time limits the maximum fluorescence that can be emitted by each atom. This is not a problem when dealing with tens of thousands of atoms (or more), but for small numbers of atoms the resulting signal may not exceed the readout noise of the camera.

An alternate detection system, which works well for individually separated atoms,

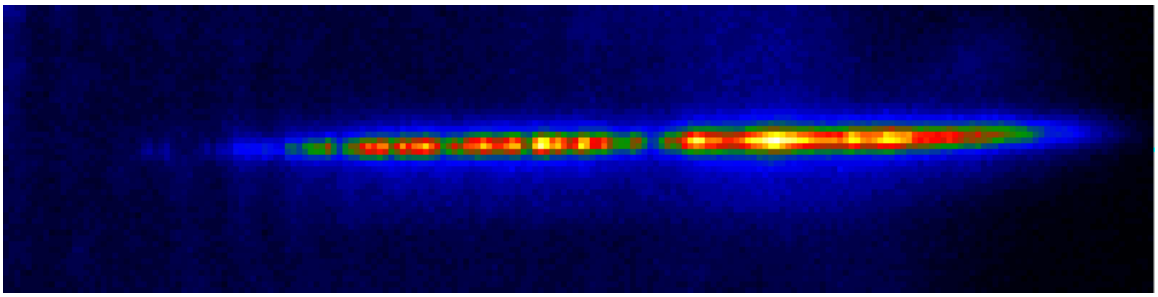

Figure 5.4: Several hundred atoms in an optical lattice. The lattice was imaged by using the molasses beams to continuously cool the atoms, with an exposure time of 0.7 s.

is continuous observation [61]. In this scheme, the MOT beams are used to continuously cool the atoms in the trap, and the fluorescence from the atoms is observed continuously by the camera. This allows camera exposures of (nearly) arbitrary length, which makes it comparatively easy to detect single atoms. Furthermore, for a sufficiently deep trap, the cooling from the MOT beams will counteract any heating sources in the trap, thereby extending the trap lifetime to the limit imposed by collisions, either with background gases or with other atoms in the same lattice site. This technique works best if there is no more than one atom per lattice site. In lattice sites with many atoms, the loss rate due to inelastic light-assisted collisions becomes very high [104]. A sample image using continuous observation is shown in Figure 5.4. This detection scheme produces accurate measurements of the trap population even in the limit of single atoms and is used for measuring the lifetime for a small initial population.

5.4 Single Atom Lattice

We use continuous observation to detect individual atoms in the optical lattice. First, a small number of atoms are loaded into the trap, as described previously. The magnetic gradient is turned off, and the trap is imaged for a 700 ms exposure time. The resulting picture is used to count the number of atoms in the trap. By taking

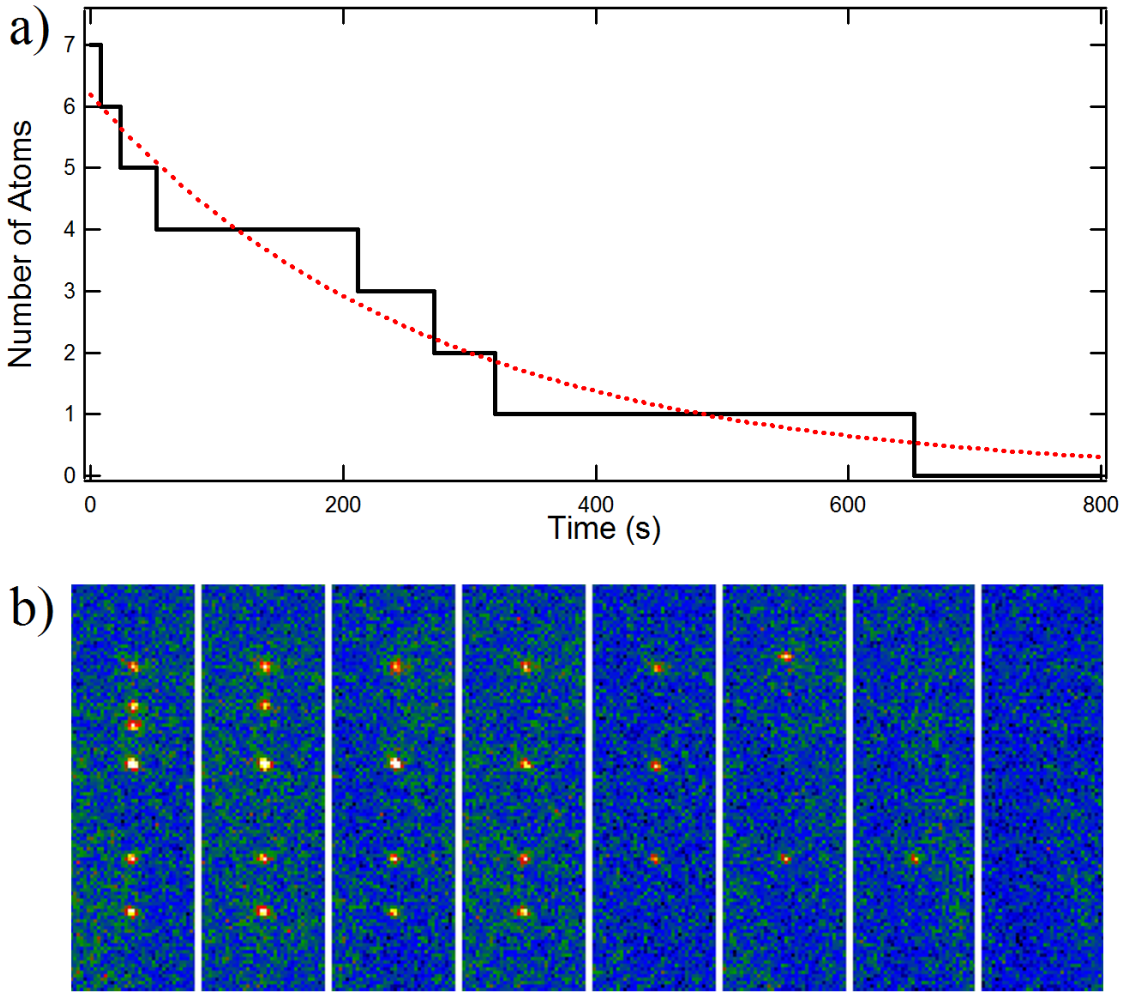

Figure 5.5: Individual atoms escaping from the lattice, one at a time. (a) Number of remaining atoms as a function of time. The red dotted line is an exponential fit to the data, with a lifetime of 270 s. (b) Images of the atoms remaining in the trap, for an exposure time of 1.7 s. Each atom produces about 3000 counts on the camera. The first image shows seven atoms, and each subsequent image has one fewer. Initially, two of the atoms are too close to distinguish.

repeated exposures, one can watch as the atoms leave the trap, one by one. A typical evolution of the trap population versus time is shown in Figure 5.5(a). For these data, the atoms were continuously cooled and monitored. Note that one of the atoms remains trapped for more than 600 s. Figure 5.5(b) shows successive pictures of the remaining atoms in the trap, starting with seven and ending with zero. An exponential fit to this limited data set indicates a $1/e$ lifetime of 270 s.

Loading into the lattice is probabilistic, meaning it is not possible to control which lattice sites are occupied. This makes it difficult to produce a well organized, individually addressable string of atoms. Active reorganization of atoms in an lattice has been demonstrated by others [63], but it is not within this experiment's current capabilities. Instead, a probabilistic method to redistribute and spread out the trapped atoms is employed. By briefly blocking the reflected dipole trap beam, the lattice is converted to a single focus trap. The atoms are then free to spread out along the axis of the trap. When the reflected beam is unblocked, the atoms are recaptured in the lattice sites, and rearranged probabilistically along the length of the trap. By repeating this procedure, a string of distinguishable atoms is eventually obtained. Typical results from this technique are shown in Figure 5.6.

5.5 Trap Lifetime

Continuous cooling has been shown to work well in the single atom limit, producing lifetimes in excess of 200 s. Next we examine the heating effects which limit the lifetime in the absence of cooling, beginning with a measurement of the trap lifetime. Atoms are loaded into the MOT for 15 seconds and then transferred into the lattice. This produces an initial population of about 100 atoms distributed across 500 lattice sites. Once the magnetic field gradient is turned off, a 700 ms exposure is taken using continuous observation. The population is measured by integrating the fluorescence over the trap area. Next, the MOT light is turned off, and the atoms are left in the

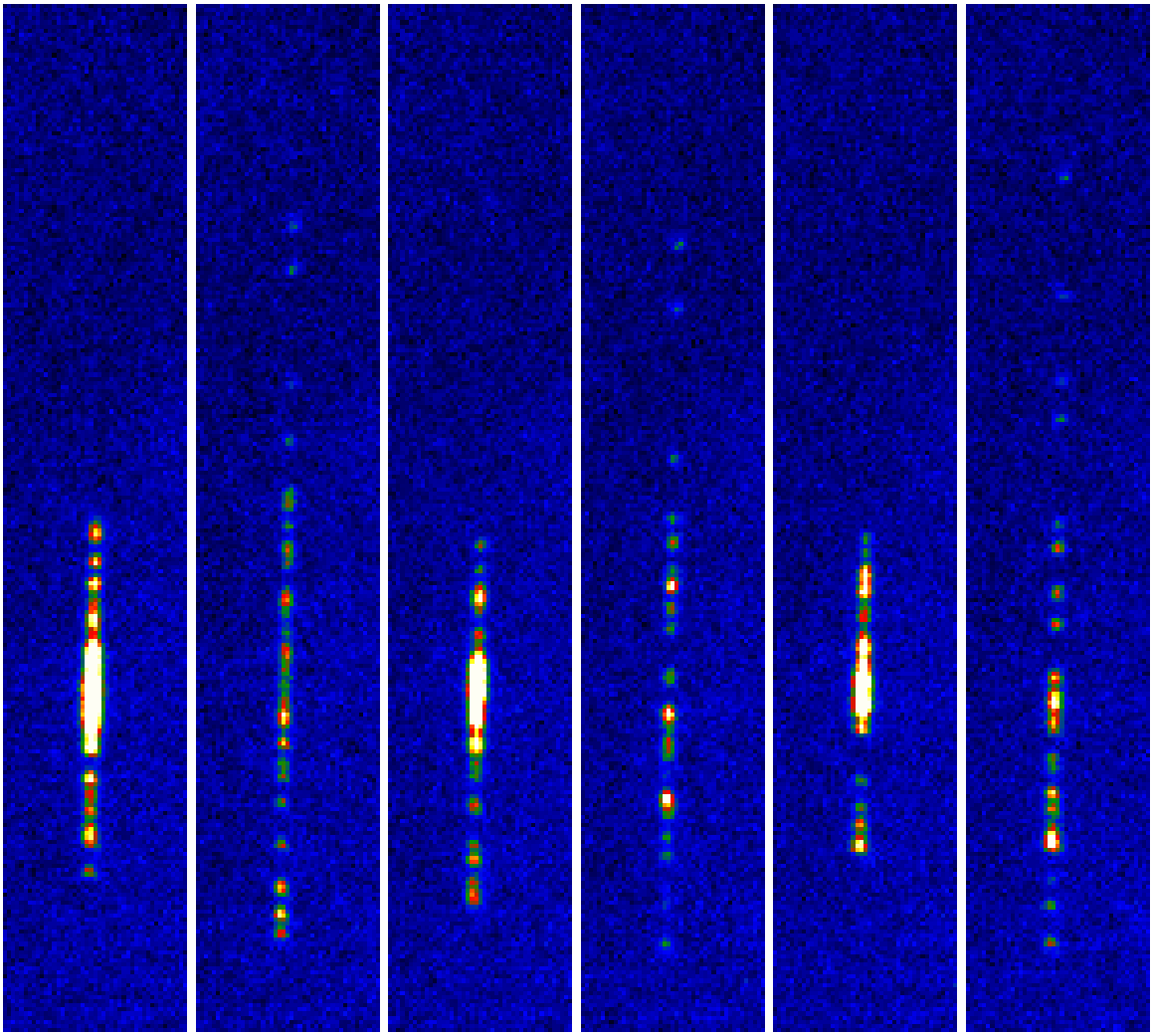

Figure 5.6: Probabilistic redistribution of atoms in an optical lattice. Atoms are redistributed by briefly blocking the reflected dipole trap beam, temporarily changing the lattice into a single focus trap. Each pair of images shows the atoms in the trap before and after the redistribution.

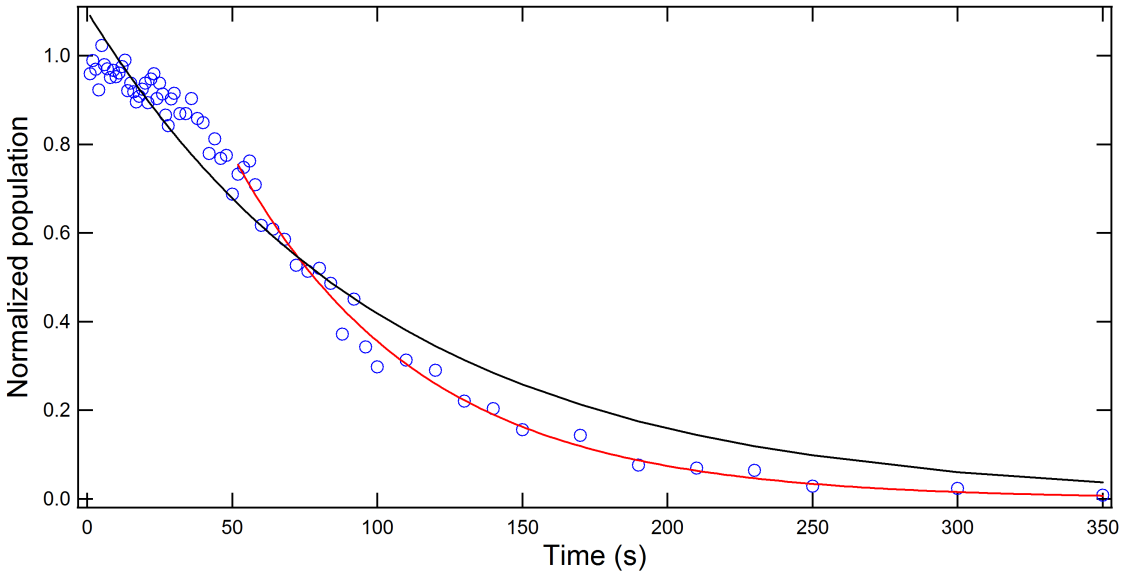

Figure 5.7: Graph of trap population over time with no cooling. The blue circles show the experimental results. The black line is an exponential fit to all of the data, and gives a lifetime of 103 s. The red line is an exponential fit only to data points beyond 50 s, and gives a lifetime of 62 s.

trap for some wait time, Δt. After that time has passed, a second image is taken using continuous observation. The remaining atoms are then emptied from the trap to prepare for the next run. The trap is reloaded for each run because some fraction of the atoms has been lost, and each run needs to begin with a similar number of atoms.

This procedure is repeated for a variety of different wait times (Δt). Decay of the trap population versus time is shown in Figure 5.7, with the remaining number of atoms normalized to the initial population loaded for each run. Each data point is the average of 5 runs. A simple exponential fit to the data gives a lifetime of 103 s, however, the data do not fit well to a standard exponential decay. Following loading, there is an initial period of about 20 s during which the atom loss is minimal. Subsequently, the population decays exponentially with a 62 s time constant. This behavior is consistent with a heating source which continuously increases the total energy of the atoms. The initial delay in the atom loss occurs because the thermal

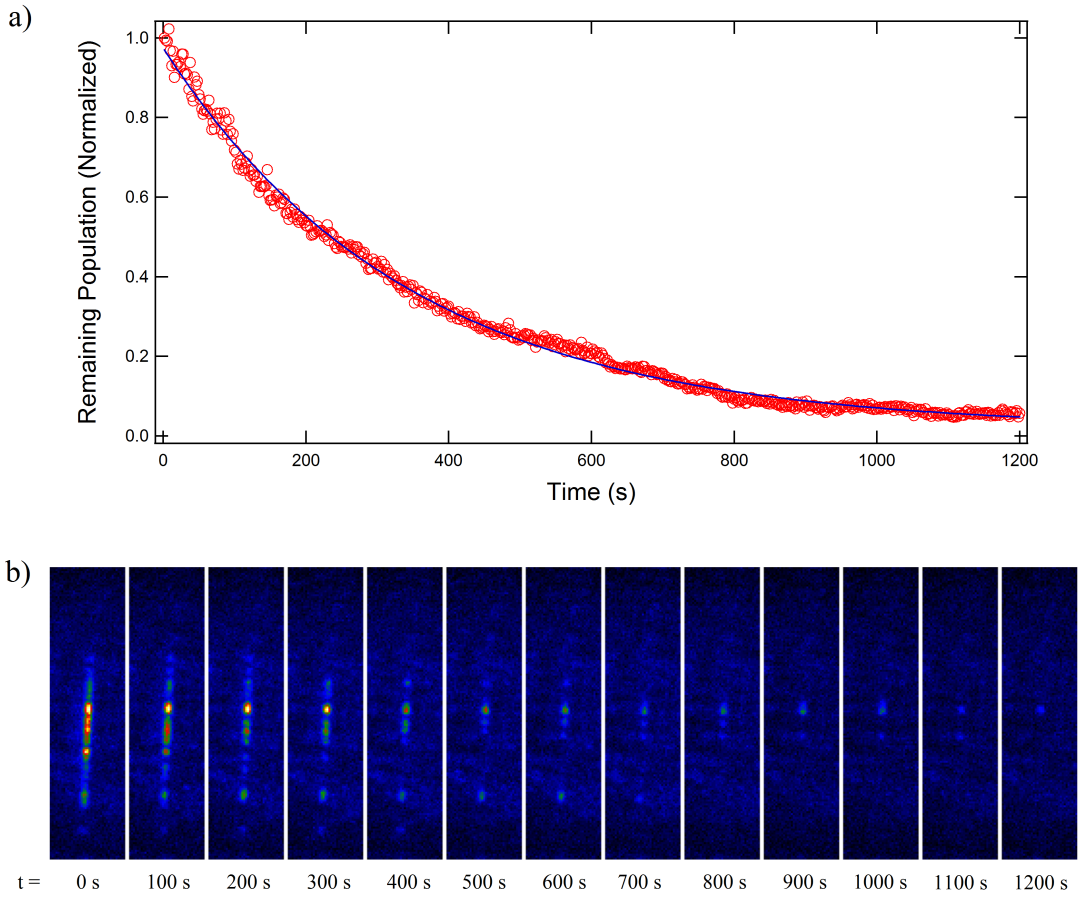

Figure 5.8: Trap lifetime with continuous cooling. (a) Graph of trap population over time, averaged over four runs. Initial population is about 100 atoms distributed over 500 lattice sites. The red circles show the experimental results. The blue line is an exponential fit to the data, and gives a lifetime of 343 s. (b) Images of the trap each 100 s after loading, for a single run. One atom remains in the trap after 1200 s.

energy of the atoms immediately after loading is considerably below the trap depth. Thus, there is a time delay before atoms gain enough energy to leave the trap. This behavior will be examined more closely later.

For comparison, lifetime data are taken while using the cooling light to continuously cool the atoms. A sample lifetime graph is shown in Figure 5.8, along with several sample pictures taken at various points throughout the data. An exponential fit to the data gives a trap lifetime of 343 $\pm$27 s, which is consistent with a vacuum-limited lifetime at a pressure of around 10^{-11} Torr [105].

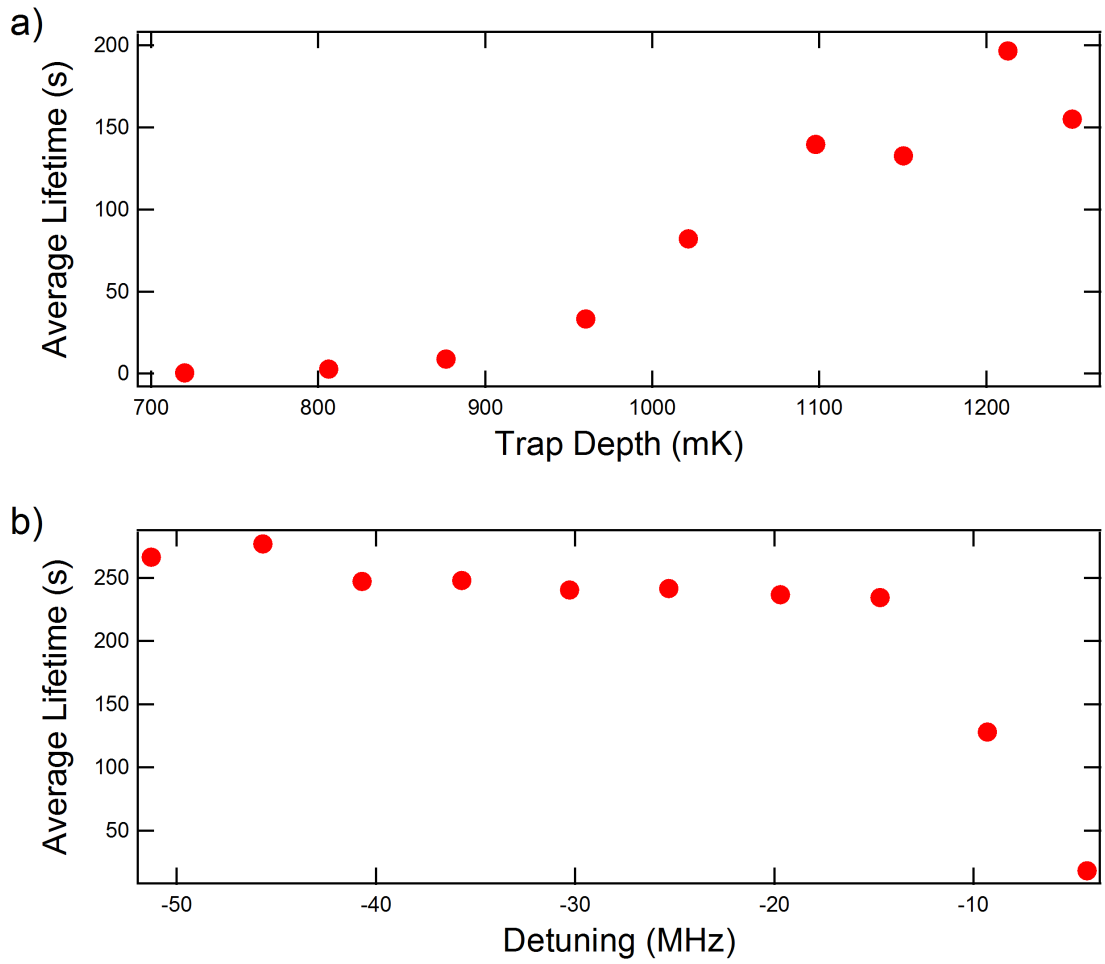

Figure 5.9: Trap lifetime versus trap depth and versus detuning. (a) Average lifetime versus trap depth. Each data point is the result of an exponential fit to the average of three runs. (b) Average lifetime versus cooling light detuning. Each data point is the result of an exponential fit to the average of three runs.

The continuously cooled trap lifetime was measured for a variety of different trap settings in order to better understand the parameters affecting cooling and trap loss. Figure 5.9(a) shows the trap lifetime as a function of trap depth. For small trap depths (<1 mK), the lifetime depends strongly on the trap depth. In this regime, the primary loss mechanism is evaporative, due to random fluctuations in the energy of the atom as it is perturbed by the cooling light. As the trap depth increases well above the average temperature of the atoms, these evaporative losses become rare and the lifetime is limited instead by collisions with background gas.

Figure 5.9(b) shows the effect of the cooling light detuning on the trap lifetime. For large detunings ($\Delta < -20$ MHz), the trap lifetime is fairly constant. However, as the detuning becomes small, the lifetime starts to degrade rapidly.

There was no convenient way to precisely measure the magnetic field at the center of the trap. The optimal settings for the applied bias fields were determined by maximizing the observed trap lifetime. It was found that the trap lifetime remains nearly constant within 50 mG of the chosen settings, but outside of that range the trap lifetime drops quickly. At 100 mG, the continuous cooling lifetime is less than 10 s.

The effects of beam imbalance on the lifetime are shown in Figure 5.10. Changing the beam balance had no significant effect on the lifetime. This effect was further examined by physically blocking one or more of the cooling beams. Continuous cooling was found to be remarkably resilient against the effects of blocking any one beam. Nevertheless, blocking both counter-propagating beams on any single axis prevented continuous cooling from working correctly.

The trap lifetime is ultimately limited by collisions. Continuous cooling is effective against gradual heating sources, but collisions can impart enough energy to cause an atom to leave the trap. In our case, two types of collisions are important. When

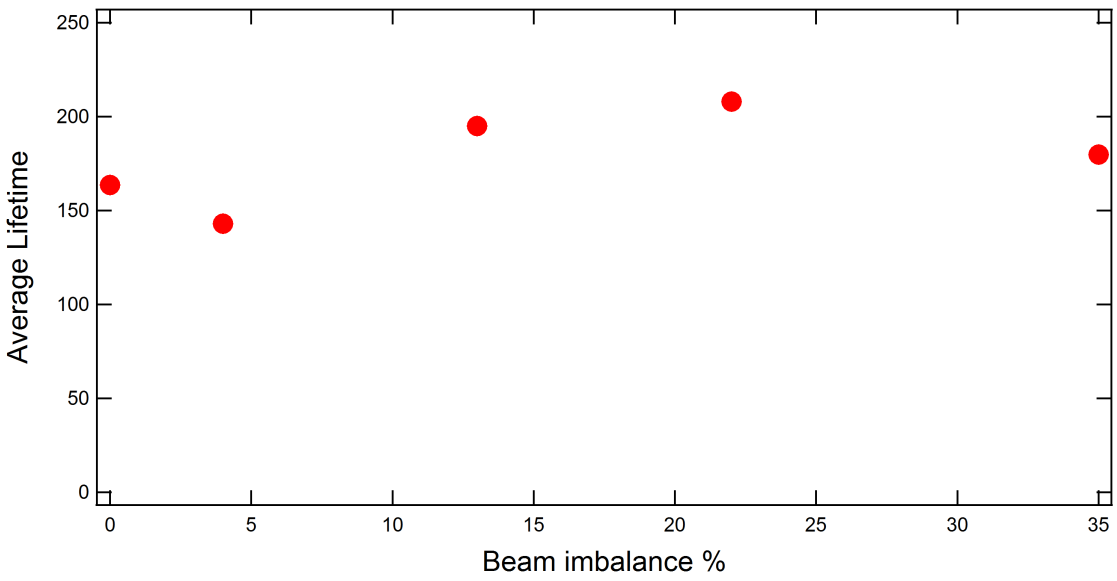

Figure 5.10: Graph showing trap lifetime versus beam imbalance. One beam in each of the three pairs of cooling beams was set to a higher intensity than the other. Each data point is the result of a fit to the average of two lifetime graphs.

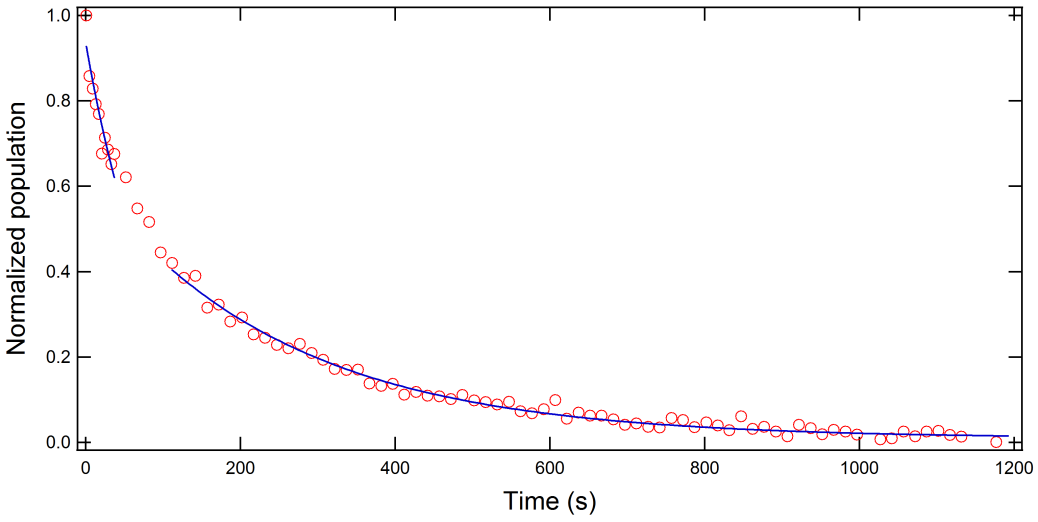

Figure 5.11: Graph of trap population over time, with continuous cooling. Initial population is about 700 atoms distributed over 500 lattice sites. The red circles show the experimental results. The blue lines show an initial exponential fit with a 91 s lifetime, transitioning to an exponential curve with a 276 s lifetime. The fast initial loss is caused by light-assisted collisions in lattice sites containing more than one atom. Once these atoms have left the trap, the lifetime is limited primarily by collisions with background gas particles.

there is more than one atom per lattice site, the lifetime is primarily limited by light-assisted collisions between trapped atoms. The resulting collisional loss rate is given by $R = \beta\rho$, where β is the loss rate constant and ρ is the two-atom density in a single lattice site [104]. We estimate our loss rate constant at $\beta \approx 10^{-11}$ cm^3/s [106], and our density is approximately $\rho = 2 \times 10^{10}$ cm^{-3} for two atoms in a lattice site. This leads to a collision rate $R \approx 0.02$ s^{-1}. When the number of atoms is much less than the number of lattice sites, then the lifetime is limited by collisions with background gas. In a typical lifetime graph, there is an initial, fast exponential decay (due to light assisted collisions) gradually transforming into a slower exponential decay (due to background collisions). This is illustrated by the data in Figure 5.11. If there were only a small number of atoms to begin, light assisted collisions would not apply, and there would be only a pure exponential due to background collisions.

5.6 Heating Mechanisms

A quantitative comparison between the measured results and possible heating sources can help reveal which heating processes are most pertinent to this experiment. Random fluctuations in the trapping laser intensity and position are known to cause heating in trapped atoms. The expected heating rate in the trap is derived from measurements of the intensity noise power spectra of the trap beam and the noise power spectra for fluctuations of the trap equilibrium position using a theoretical model developed by Thomas' group in 1997 [78]. Laser intensity fluctuations cause parametric heating of the atoms due to a modulation of the trapping potential. This leads to an exponential energy growth of the atoms with a time constant Γ given by [78],

$$\Gamma = \frac{1}{T_I} = \pi^2 \nu_{tr}^2 S_{\epsilon_I}(2\nu_{tr}), \tag{5.1}$$

where T_I is the energy e-folding time, ν_{tr} is the trap frequency, $\epsilon_I = [I(t) - I_0]/I_0$ is the fractional fluctuation in the laser intensity, and $S_{\epsilon_I}(2\nu_{tr})$ is the relative intensity

noise power spectrum defined as

$$S_{\epsilon_I}(\nu) \equiv \frac{2}{\pi} \int_0^\infty d\tau \cos(\nu\tau) \left\langle \epsilon_I(t)\epsilon_I(t+\tau) \right\rangle . \tag{5.2}$$

The other dominant heating mechanism results from fluctuations in the trap position (e.g., due to laser beam pointing or phase instabilities). In this case, the energy grows linearly with a heating rate $\dot{Q}$ given by

$$\dot{Q} = 4\pi^4 \nu_{tr}^4 m S_{\epsilon_x}(\nu_{tr}), \tag{5.3}$$

where ϵ_x is the fluctuation in the location of the trap center and $S_{\epsilon_x}(\nu_{tr})$ is the trap position noise power spectrum, which can be calculated using Eq. (5.2), with ϵ_x substituted for ϵ_I.

The intensity noise and the position fluctuation in the radial direction of the trapping beam are measured using a balanced detection method [107] in which the laser beam is separated by a 50-50 beam splitter and each beam is focused onto a different detector (see Figure 5.12). One of the beams is half blocked by a razor blade, and the other is 50% attenuated to equalize the power received by each detector. The output of the first detector measures the power fluctuations, while the difference between the two detectors measures the position fluctuations. Figure 5.13(b) shows the relative intensity noise power spectrum averaged over 50 runs. An example of observed voltage noise due to intensity fluctuations is also shown in Figure 5.13(a), where 1 mV fluctuation corresponds to 10^{-4} relative fluctuation in laser intensity.

These measurements were performed separately for two different Ytterbium doped fiber lasers, both operating at 1064 nm, but with different maximum output powers (10 W and 20 W respectively). They were also performed both with and without an AOM controlling the beam power. In measurements including an AOM, the intensity noise was dominated by noise introduced by the AOM driving electronics. Without the AOM, the 20 W laser was found to have approximately 100 times higher intrinsic intensity noise compared to the 10 W laser. The 10 W laser was used without an

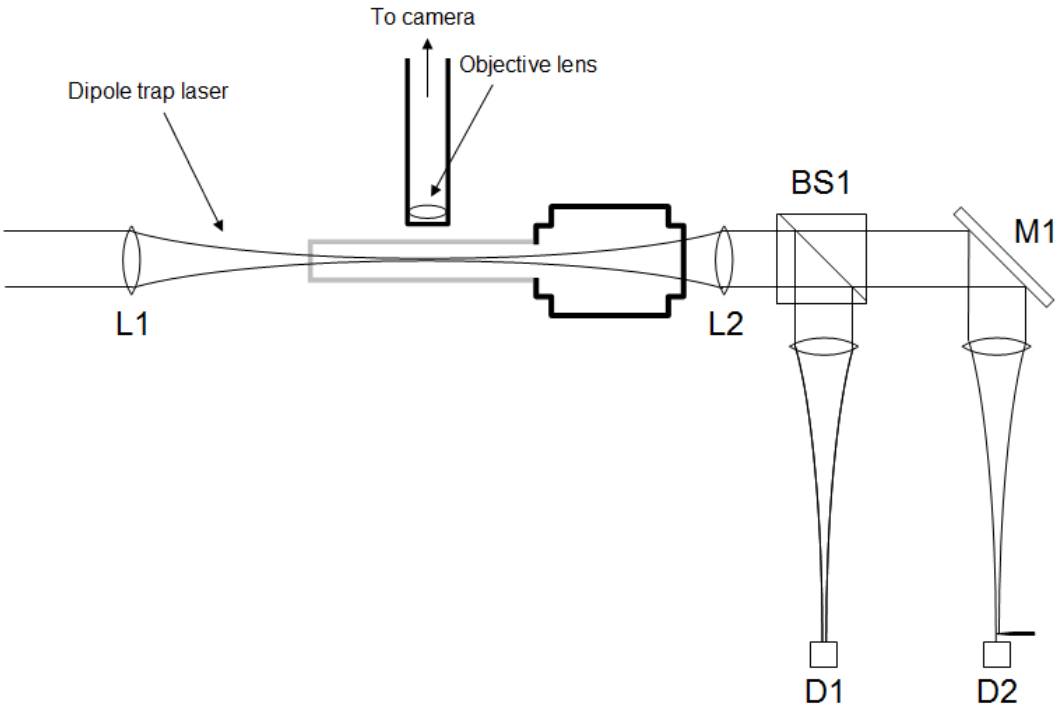

Figure 5.12: Diagram of the setup used for measuring intensity noise and radial position fluctuation. Light from the trapping laser is focused by lens L1 ($f = 300$ mm) and re-collimated by lens L2 ($f = 300$ mm) just as when creating a lattice. The light is then split on a 50:50 beamsplitter (BS1). The beams are then focused by lenses L3 and L4 ($f_3 = f_4 = 300$ mm), and detected by two photodiodes (D1 and D2). One of the beams is half-blocked at its focus by a razor blade.

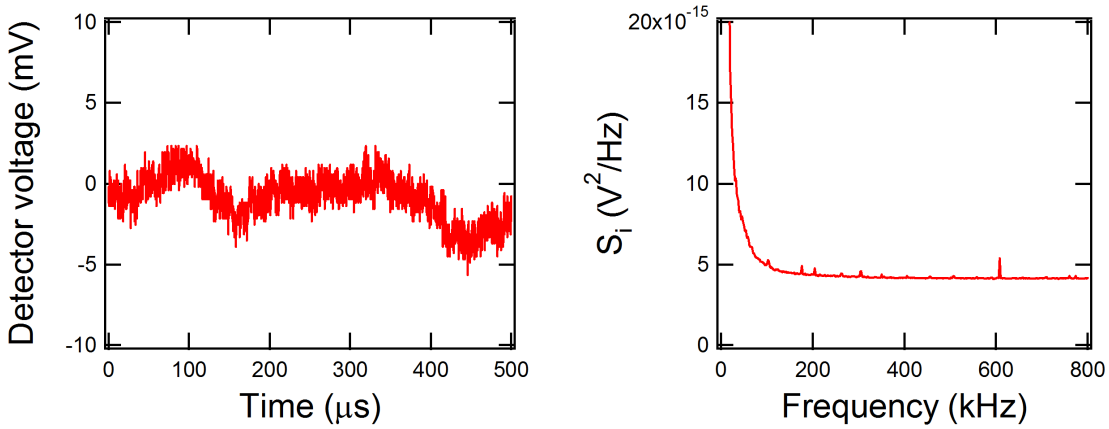

Figure 5.13: Measurement of the intensity noise on the optical trapping laser. (Left) A typical measurement of the intensity noise, as detected on a photodiode. (Right) The resulting intensity noise power spectrum, averaged over 50 runs.

AOM for the noise measurements shown in Figure 5.13 and Figure 5.15, and for all other measurements except where noted.

The position instability in the axial direction is measured using an interferometric technique. A beam splitter is placed in the path of the optical lattice laser before the focusing lens L1 (see Figure 5.14). A mirror is glued directly to one side of the beam splitter to form one arm of an interferometer. The beam passing through the beam splitter retro-reflects from the mirror (M1 in Figure 5.14) in the lattice setup, forming the second arm of the interferometer. These two beams interfere and are focused onto a detector. Once properly aligned, the phase fluctuations between the two arms are measured by monitoring the intensity fluctuation on the detector. Laser power fluctuations are simultaneously monitored on a separate detector. Subtracting these two signals isolates the phase fluctuations, which can then be used to calculate the position noise in the axial direction. Figure 5.15 shows the resulting position noise power spectrum averaged over 50 runs, along with an example of the observed voltage noise due to axial position fluctuations, where 1 mV fluctuation corresponds to 2.4×10^{-5} relative fluctuation in laser intensity. The corresponding heating rate

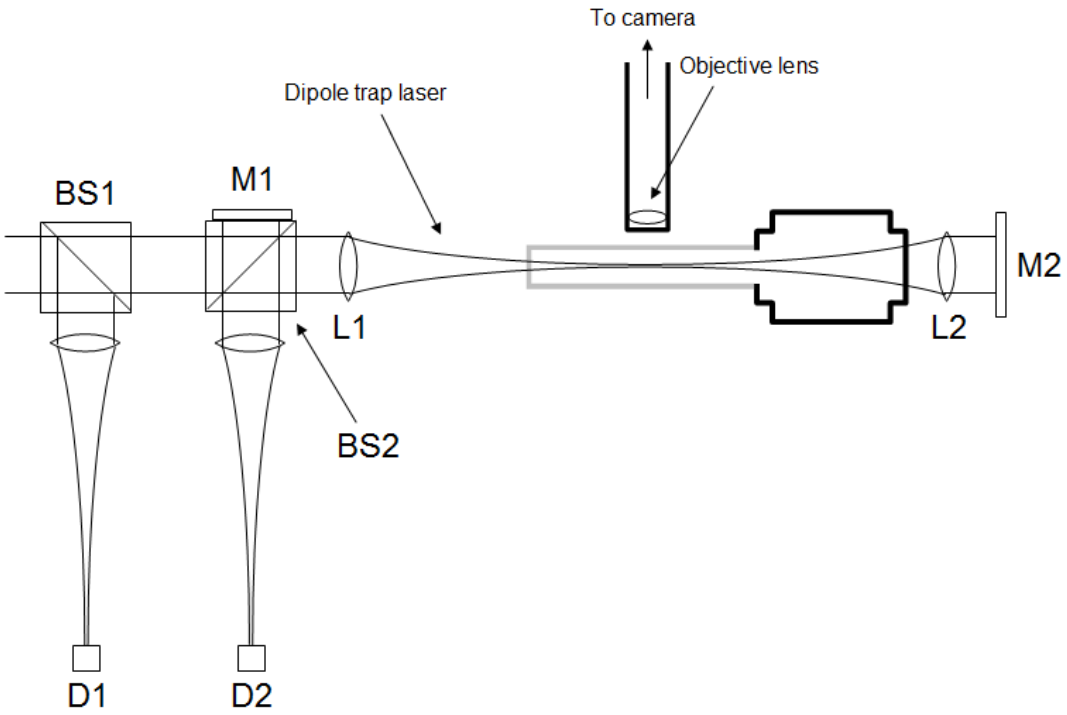

Figure 5.14: Diagram of the setup used for measuring axial position fluctuation. Light from the trapping laser is first split by a 50:50 beamsplitter (BS1). One beam is focused onto detector D1, to measure the intensity noise. The other beam passes through another 50:50 beamsplitter (BS2), splitting the beam once more. One of these beams immediately reflects off of a mirror (M1), while the other passes through the standard optical lattice setup. After retro-reflecting off of mirror M2, this beam returns and interferes with the beam that was reflected from M1. The resulting beam is focused onto detector D2.

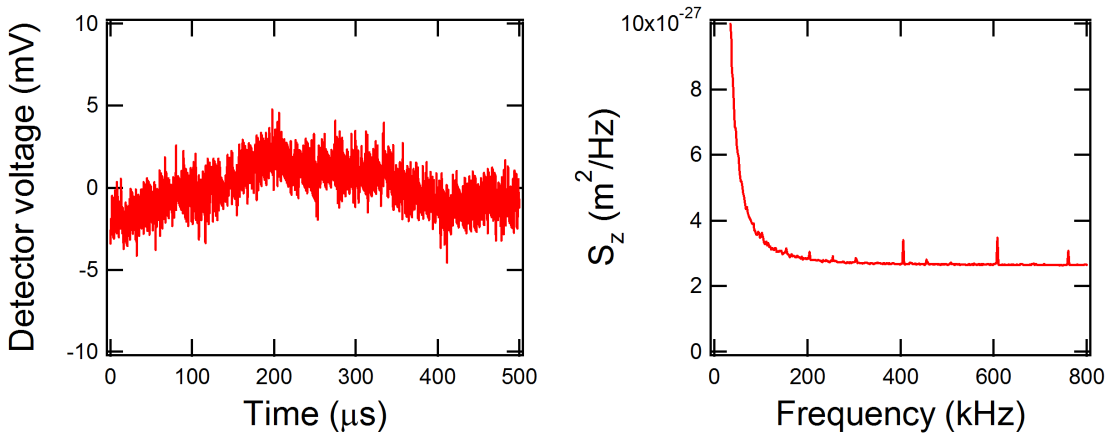

Figure 5.15: Measurement of the axial position fluctuation on the optical trapping laser. (Left) A typical measurement of the fluctuation of the interference between the two beams, as detected on a photodiode. The corresponding intensity noise has been subtracted from the signal. (Right) The resulting position fluctuation power spectrum, averaged over 50 runs.

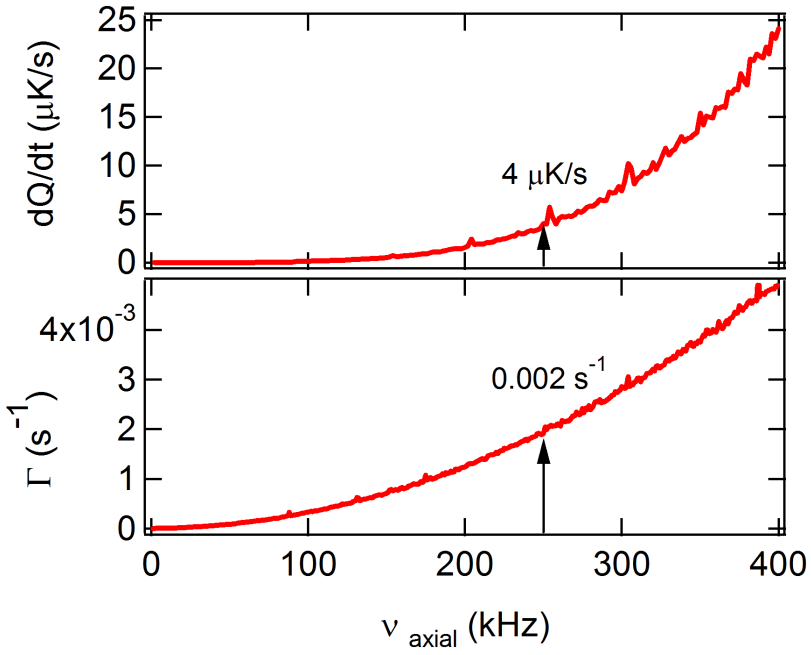

Figure 5.16: Predicted heating versus trap frequency. (top) Heating rate versus trap frequency, based on the measured axial position fluctuation power spectrum. (bottom) Energy doubling time versus trap frequency, based on the measured intensity noise power spectrum. The relevant frequency is the trap frequency in the axial direction, which is measured to be 250 kHz.

$\dot{Q}$ and heating time constant Γ calculated from Eqs. (5.1) and (5.3) are shown in Figure 5.16. In order to use these results to determine the heating rate, it is necessary to know the trap frequencies.

5.7 Trap Frequency Measurement

Trap frequencies can be calculated based on the trap parameters, however, our experience is that the measured frequency is usually substantially less than the calculated frequency [108]. The trap depth and trap frequency calculations assume perfect Gaussian beams, aberration-free focusing, harmonic trap potentials, and perfect overlap and focusing of the retro-reflected beam. In order to determine the axial and radial trapping frequencies of the optical lattice, we use parametric excitation to measure them directly [109].

Parametric excitation is a technique in which intensity modulation at a controlled frequency is intentionally added to the trapping laser for a short period of time. We use an AOM to modulate the trapping laser beam power. The AOM is driven by a function generator, which is amplitude modulated at the desired excitation frequency. Atoms are loaded into the trap as usual, and the initial population is measured. A noise component at a frequency ν is added to the laser for 5 s, and then the final population is measured. This procedure is repeated for frequencies ranging from 0.5 to 1500 kHz. The results are shown in Figure 5.17. The dips in the graph show frequencies at which atoms were lost due to parametric heating. Losses are expected at all frequencies for which $\nu = 2\nu_{tr}/n$ for $n = 1, 2, 3 \ldots$, with the largest heating at $n = 1$ [108]. A smaller and broader heating effect is expected at $\nu = 4\nu_{tr}$, due to the anharmonicity of the trap. Based on this data, the axial trap frequency is determined to be approximately $\nu_{axial} = 250$ kHz. The radial trap frequency was separately measured to be $\nu_{radial} = 2.8$ kHz.

These trap frequencies are used to calculate the expected heating rates in the trap.

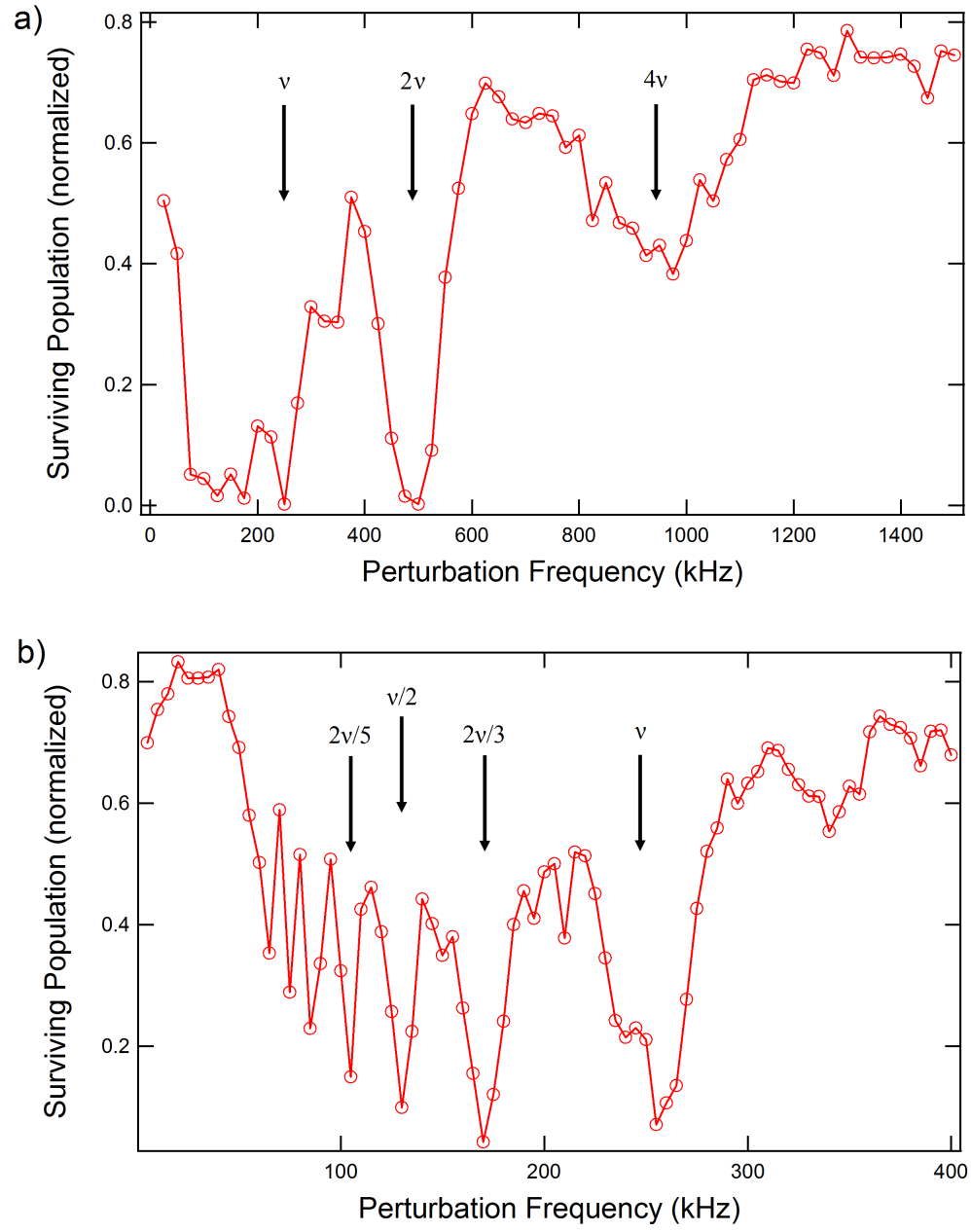

Figure 5.17: Trap frequency measurement using parametric excitation. A perturbation is added to the trapping laser at a range of different frequencies, and the effect on the atoms is measured for each frequency. (a) Graph of perturbation frequency versus surviving population over the range from 25 to 1500 kHz, for a strong perturbation. Some relevant resonance frequencies are labeled. (b) Graph of perturbation frequency versus surviving population over the range from 5 kHz to 400 kHz. Some relevant resonance frequencies are labeled.

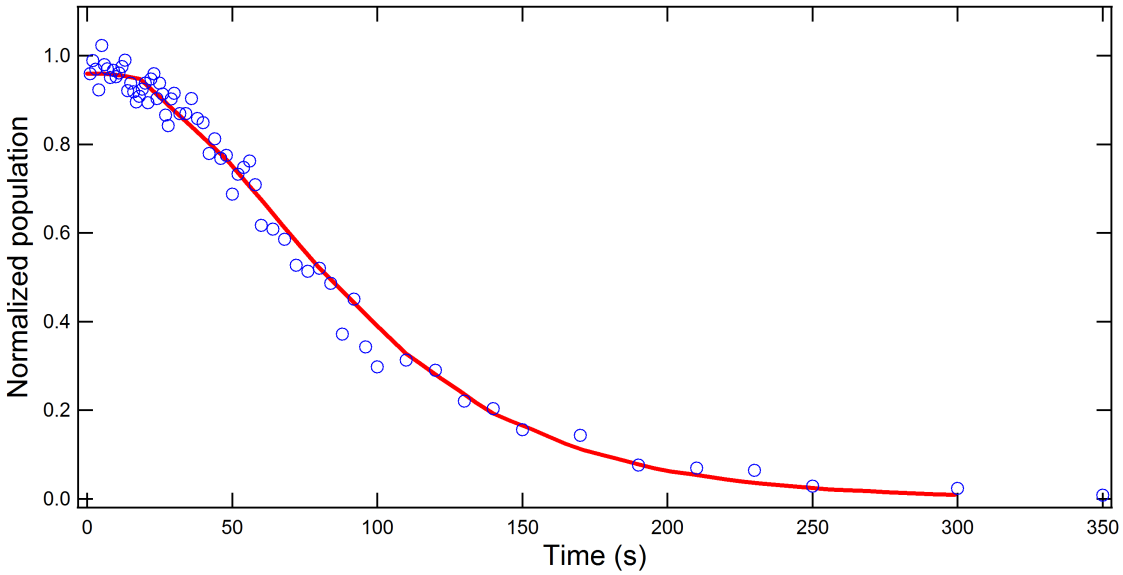

Figure 5.18: Graph of trap population over time with no cooling. The red line represents a numerical simulation, using heating parameters $\dot{Q} = 4.5$ μK/s and $\Gamma = 0.002$ s^{-1}.

Referring to Figure 5.16, $\dot{Q}$ and Γ for the axial direction are 4 μK/s and 0.002 s^{-1}, respectively. The heating rates in the radial directions are negligible compared to the heating in the axial direction because the trap frequency in the radial direction is 90 times smaller, and Γ and $\dot{Q}$ scale as ν_{tr}^2 and ν_{tr}^4 respectively.

These heating rates suggest that the trap lifetime is primarily limited by axial position fluctuations. For $\dot{Q} = 4$ μK/s and an initial temperature around 100 μK, it will take about 275 s for the atoms to reach an energy equal to the trap depth. In contrast, for $\Gamma = 0.002$ s^{-1}, it will take over 1500 s to gain an equivalent amount of energy due to intensity fluctuations.

5.8 Heating Model

The time evolution of the trap population can be modeled with a Fokker-Planck equation for the energy distribution $n(E,t)$ given by [110],

$$\frac{\delta n}{\delta t} = (\frac{\Gamma}{4}E^2 + \dot{Q}E)\frac{\delta^2 n}{\delta E^2} - \dot{Q}\frac{\delta n}{\delta E} - \frac{\Gamma}{2}n. \tag{5.4}$$

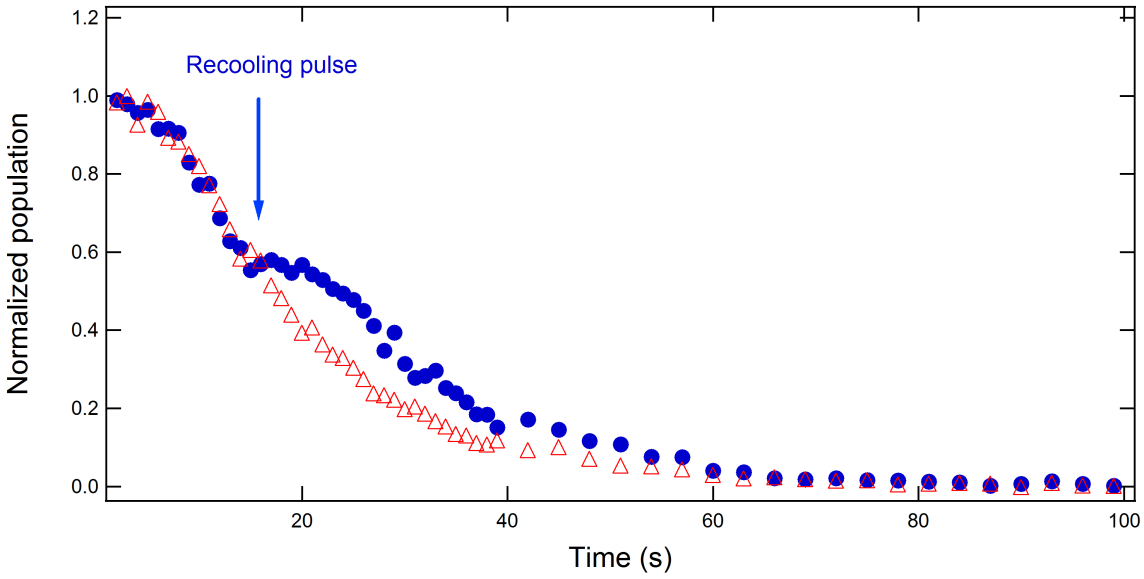

Figure 5.19: Graph of trap population over time with no cooling (red triangles), and with a single 5 ms cooling pulse (blue circles). The cooling pulse re-cools the atoms to the bottom of the trap, significantly increasing the effective lifetime.

Numerical solutions of Eq. (5.4) are obtained assuming an initial Maxwell-Boltzmann distribution with a temperature of the trapped atoms of 100 μK. The results, shown as a solid curve in Figure 5.18 for the parameters $\dot{Q} = 4.5\ \mu\text{K/s}$ and $\Gamma = 0.002\ \text{s}^{-1}$, closely reproduce the observed trap population, and in particular, show the 20 s delay before the onset of appreciable trap loss. Heating is primarily due to $\dot{Q}$ (due to fluctuations in the trap position), but Γ (due to intensity fluctuations) was also included in the numerical solution because it subtly affects the shape of the tail of the curve. It is worth noting that this model is only strictly valid assuming a harmonic potential. In reality, the effective trap frequency becomes smaller as an atom approaches the top of the trap. It is therefore likely that the model slightly overestimates the heating in the trap.

5.9 Pulsed Cooling

The most notable feature of the lifetime measurements shown in Figure 5.7, which is supported by the simulation, is that it takes a finite amount of time for the atoms to

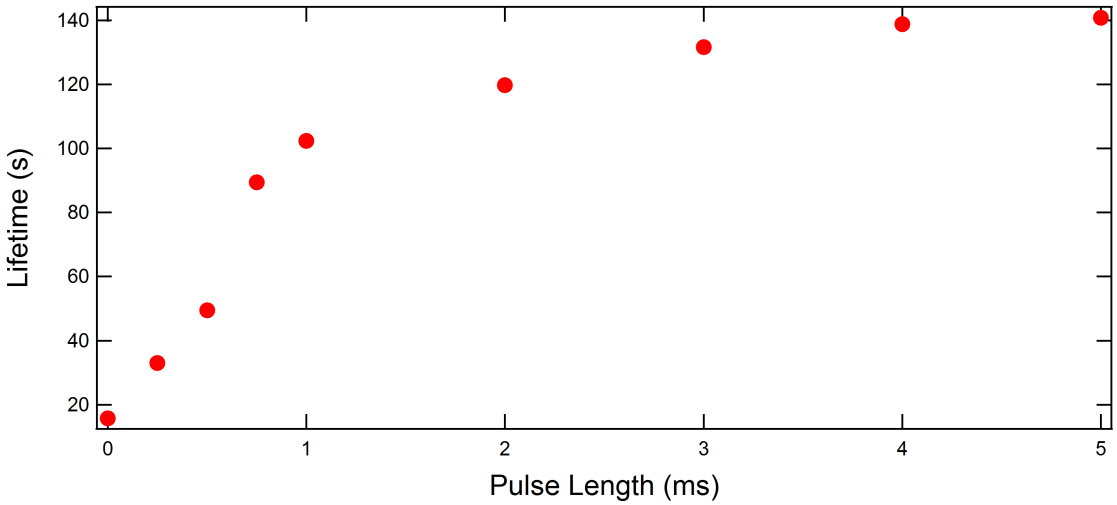

Figure 5.20: Graph of trap lifetime versus cooling pulse length. A cooling pulse is applied every two seconds, for different pulse lengths. Each data point is the result of an exponential fit to the average of three lifetime runs.

heat up sufficiently to be ejected from the trap. It follows that it should be possible to extend the lifetime of the trapped atoms by occasionally re-cooling them to the bottom of the trap. This principle was demonstrated by applying a short 5 ms pulse of laser-cooling light to the atoms at $t = 15$ s. The cooling light is provided by the laser beams used to form the MOT, detuned for optimal continuous observation. As is evident from the data shown in Figure 5.19, the loss of atoms is halted for a time comparable to the delay in atom loss following initial loading. Note that for these data, the overall lifetime is shorter than in Figure 5.7. This is because the 20 W Yb fiber laser with 100× higher intensity noise was used as the trapping laser for this measurements, and an AOM was present in the beam path.

The effect of cooling pulses was further explored by applying a short cooling pulse to the atoms at even intervals of two seconds. This was repeated for several different pulse lengths (see Figure 5.20). It was found that the lifetime increases with the pulse length, up to about 4 ms, where it levels off. This suggests that a 4 ms pulse is sufficient to cool the atoms to near their minimum temperature. This is consistent

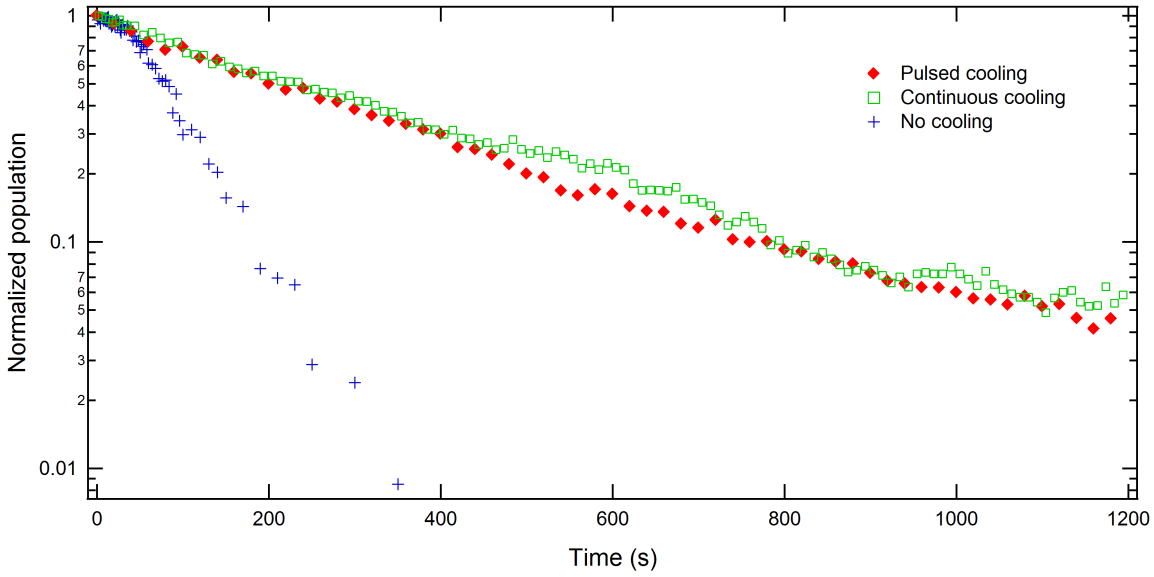

Figure 5.21: Remaining population versus time, for different cooling regimes. For the pulsed cooling data (red diamonds), cooling light was pulsed on for 1 s after each 19 s gap. For the continuous cooling data (green squares), the cooling light remained on at all times. For the no cooling data (blue crosses), the cooling light remained off at all times.

with the cooling rate expected due to Doppler cooling, which is calculated at around 200 μK/s.

The results in Figure 5.19 and Figure 5.20 suggest that it should be possible to minimize atom loss caused by heating almost entirely by providing cooling pulses at time intervals shorter than the initial heating time. The data in Figure 5.21 demonstrate that this is indeed possible and show a dramatic increase in the lifetime by application of a periodic cooling pulse to the atoms. For each cooling cycle, the atoms are held in the dark for 19 s, followed by a one second cooling pulse. The length of the cooling pulse was chosen such that it exceeds the camera exposure length, allowing a picture of the atoms to be taken during each cooling pulse. As discussed earlier, only a 4 ms pulse is actually necessary for cooling. The trap population for this cooling method shows a simple exponential decay with a 310 s lifetime. Figure 5.21 also shows a comparison between the lifetime of the pulsed cooling method and the

case where the atoms are continuously exposed to the cooling light. The continuously cooled atoms exhibit approximately the same decay rate as in the pulsed cooling case.

As discussed earlier, the trap lifetime in the absence of cooling is limited by fluctuations in the axial trap position. These fluctuations are most likely due to vibrations in the mount for the mirror used to form the lattice standing wave. Although the measured fluctuations of the lattice standing wave are very small ($\Delta x_{rms} \sim 10^{-4}\lambda$ in the frequency range from 10 kHz to 2 MHz), they provide the dominant heating source. In the current setup, it is necessary to have an adjustable mirror mount to achieve the required alignment of the lattice. It should be straightforward to reduce these vibrations by moving to a fixed mount in the future. The heating due to the laser intensity noise is expected to limit the lifetime to >1000 s, which is much longer than the background-limited lifetime.

5.10 Optical Conveyor

Another important atom trapping tool is the optical conveyor, which can be used to reposition and reorganize atoms within the trap [58, 61]. It is particularly useful for moving qubits into or out of a probe beam or area of interest [63]. In our lab, this method has been used to deterministically deliver individual atoms to a high finesse optical cavity [49], which is a crucial step toward cavity-assisted entanglement generation.

An optical conveyor is created when the two counter-propagating beams in an optical lattice have slightly different frequencies [58]. This requires using two independent beams rather than retro-reflecting the first one. However, in exchange for the increased complexity, the atoms can be translated along the axis of the trap.

The optical conveyor is constructed using two 1064 nm beams, each with a power of 1 W. The beams are created by the same laser, using a polarizing beam splitter cube, and each is passed through a different 40 MHz AOM. By slightly changing the

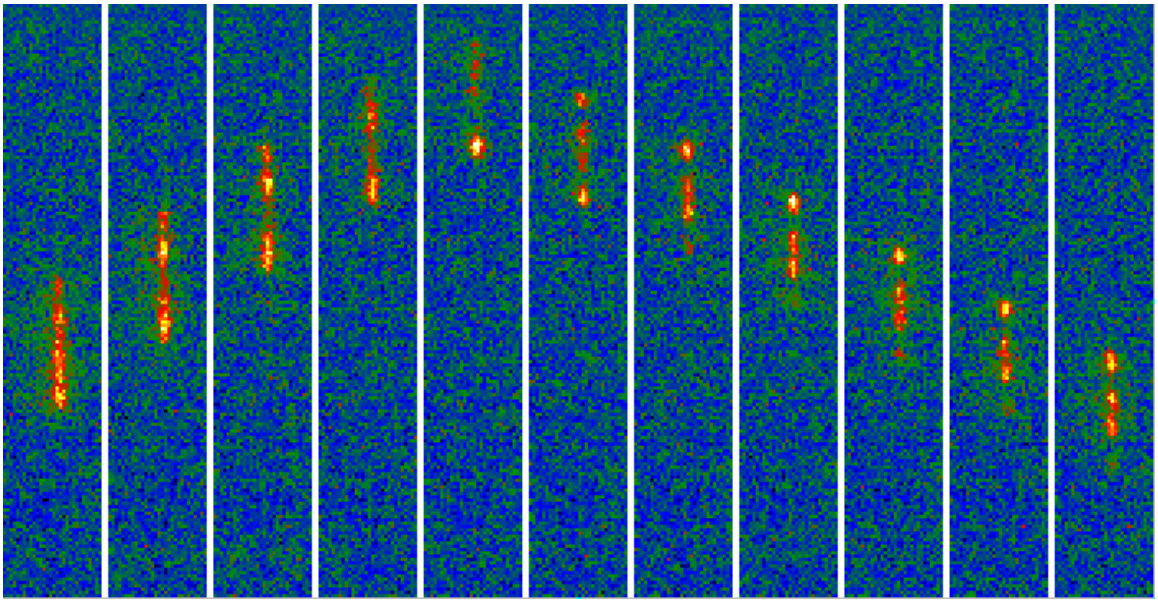

Figure 5.22: Series of images showing atoms being translated in an optical conveyor. The images are taken 1 s apart.

frequency of one of the AOMs, the velocity of the trapped atoms in the axial trap direction can be precisely manipulated.

Atoms were trapped and observed in an optical conveyor using continuous observation. A velocity was imparted to the atoms in the trap, causing them to move along the trap axis. Using this method, the atoms can be moved to whichever location in the trap is desired. In particular, for loading single atoms, it allows any arbitrary trapped atom to be positioned at the center of the area of interest.

Continuous observation of the optical conveyor was comparable to observing the simple lattice. Atoms could be moved within the continuous observation area with only moderate loss. If the atoms were moved outside of the continuous observation area, they were immediately lost from the trap. This is most likely due to edge effects of the light field. At the boundary of the molasses area, the beams are not properly aligned and balanced, producing uneven radiation pressure. Sample manipulations of atomic position are shown in Figure 5.22.

An alternate method for creating an optical conveyor was also tested. This method

uses the simple lattice setup with a translation stage underneath the retro-reflection mirror. Physically moving this mirror a distance along the trap axis causes the trap itself to move by the same amount. Although this method was successful in moving the atoms, it also caused significant loss from the trap. This loss is probably due to slight misalignment in the retro-reflection beam, introduced as the mirror moves along the axis, or to heating caused by vibrations of the mirror.

5.11 Dual Lattices

We also demonstrate two closely spaced, parallel lattices with resolvable trapped atoms. This could be useful for a number of different entanglement schemes. In particular, two atoms in parallel lattices passing through a high finesse optical cavity could be entangled using a single photon [49]. Using conveyor techniques, this could be extended to any pair composed of one atom from each lattice.

A dual lattice can be created by adding an additional trapping beam, nearly co-propagating with the first. The second beam is identical to the first, except with orthogonal polarization. The two beams are combined on a polarizing beam splitter cube, with the two traps separated slightly in the radial direction. Both beams are retro-reflected, creating two parallel lattices. The beams are aligned to produce a spacing of 35 μm, with the MOT halfway between the two traps.

Figure 5.23 shows individual atoms in two parallel lattices. Comparable loading of the two traps is not difficult to obtain, although it still remains probabilistic. For separation distances closer than 2.5 times the trap waist (32 μm), the lattices began stealing atoms from each other occasionally, and at a separation distance of about 1.5 times the trap waist (19 μm), the lattices merged into a single lattice positioned halfway between the two beams. This effectively sets a limit on the minimum separation distance between the lattices.

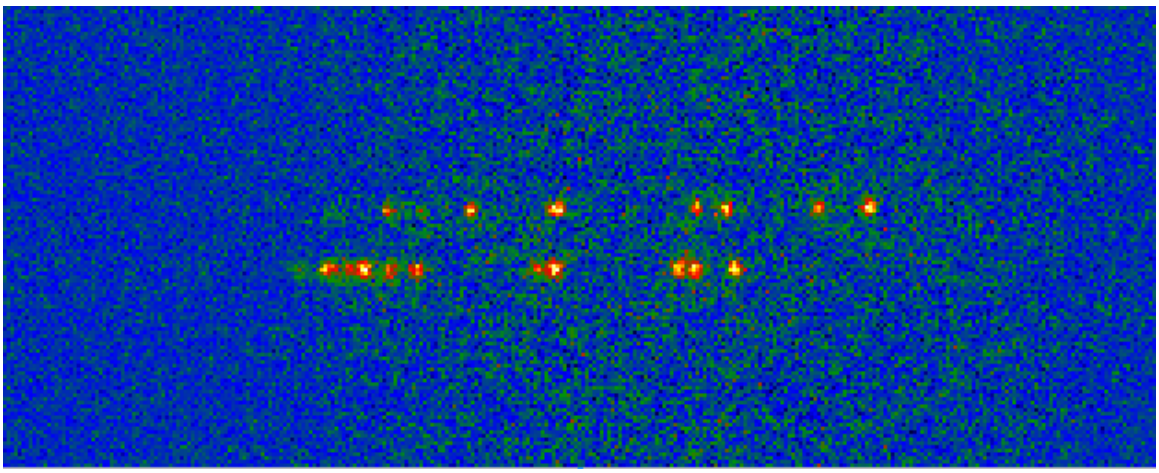

Figure 5.23: Image of individual atoms in two parallel lattices.

CHAPTER VI

NONDESTRUCTIVE STATE DETECTION

The development of techniques to trap individual laser cooled atoms and ions have paved the way for precision metrology of unprecedented accuracy and have enabled many pioneering experiments in the field of quantum information processing. The success of these systems is due to the isolation of the atom from external environmental perturbations and to the facility with which the quantum states of the atom can be initialized, manipulated and detected using external lasers and other electromagnetic fields.

In ion traps, quantum state readout has largely been done by direct detection of state-selective fluorescence [111, 112, 113], first used to observe quantum jumps in atomic systems [114, 115, 116]. Efficient state detection requires scattering 100s of photons from the atom for typical fluorescence collection efficiencies of $\sim$1%. Each scattering event heats the atom by an amount comparable to the recoil temperature. For ion traps, this heating is negligible compared with the large depth (>1000 K) of the traps and hence quantum state readout using direct detection of state-selective fluorescence can be achieved with no loss of the ions.

Neutral atom traps are much shallower, typically $\sim$1 mK, and hence the heating induced by state detection can be comparable to or exceed the depth of the trap. For this reason, state-selective ejection of atoms was developed for accurate quantum state measurement of individually trapped neutral atom qubits [20, 62, 65, 86, 87, 88]. In this technique, rather than trying to minimize the atom heating, the atoms in one quantum state are deliberately heated out of the trap with strong, unbalanced radiation pressure. Subsequently, the remaining atoms in the quantum register (which

are now known to be in the other quantum state) are detected using radiation that is not state selective and is detuned to provide simultaneous cooling of the atoms.

While state-selective ejection of atoms is a very powerful technique, the neutral atom traps must be loaded after every readout operation, which limits the experiments to a $\sim$1 s^{-1} repetition rate. These limitations will need to be overcome to significantly advance the field of neutral atom quantum information processing. One solution that has been demonstrated is to use a cavity QED system to increase the collection efficiency of the scattered photons [56, 89, 90, 91]. The quantum state can then be determined with fewer scattering events, resulting in lower heating. A drawback of this approach is that cavity QED systems significantly complicate the experimental setup and each atom to be detected needs be localized within the small cavity mode. There is therefore a need for an accurate and robust system to read out qubits without ejecting them from the trap, while maintaining the simplicity of a free space system. This chapter will describe a procedure for directly detecting the state of a qubit in free space, with low loss and fairly high accuracy. First, the system will be modeled to roughly ascertain the likelihood of success and to find suitable experimental parameters. This will be followed by an outline of the experimental setup, an explanation of the results, and finally a discussion on how this could be improved and extended to quantum information experiments in general.

6.1 Proposed System

The following system will be used to achieve nondestructive state detection. First, a single ^{87}Rb atom is trapped in a MOT and transferred to an optical lattice. This atom will be used as a qubit, with the two hyperfine ground states $F = 1$ and $F = 2$ representing $|0\rangle$ and $|1\rangle$ respectively. The qubit is prepared in an initial state using either optical pumping or microwaves.

The state of the qubit is detected using fluorescence imaging. The qubit is probed

by a short laser pulse ($t < 1$ ms) tuned near the $F = 2 \rightarrow F' = 3$ cycling transition, causing it to fluoresce if it is in the $F = 2$ state. The resulting fluorescence is captured by a single photon counting module. After detection is complete, the atom is cooled briefly using the MOT cooling light, after which it can again be used as a qubit.

The biggest challenges involved in this scheme are heating and depumping caused by the probe laser. Assuming a balanced probe beam, the atom is expected to gain energy equal to twice the recoil temperature ($T_r = 362$ nK) each time a photon is absorbed (see section 2.1). For a 2 mK trap, this means roughly 2800 photons can be scattered before the atom leaves the trap. For a detection efficiency of 1.5%, this gives an average of 41 photons detected.

The error level due to accidental depumping depends critically on the detuning of the probe beam. If the probe beam is exactly on resonance, then off-resonant excitation is suppressed by a factor of around 8000 (≈120 photons detected). However, at a probe detuning equal to the linewidth of the transition, this value drops to 1600 (≈24 photons detected), and at two linewidths it drops to only 450 (≈7 photons detected). Tuning the probe laser exactly on resonance is not difficult; however, the differential AC Stark shift of the transition due to the optical trapping fields can result in effective detunings comparable to the transition linewidth and hence must be considered.

6.2 Numerical Simulation

In order to better quantify the model above and optimize the experimental parameter choices, we have performed semi-classical Monte Carlo simulations of the experiment. The simulations consider classical motion of the atoms in realistic optical lattice potentials, subject to random initial conditions determined by an average atom temperature of 100 μK and random recoil kicks equally distributed between two counter-propagating probe beams. The axial and radial profiles of the trap are

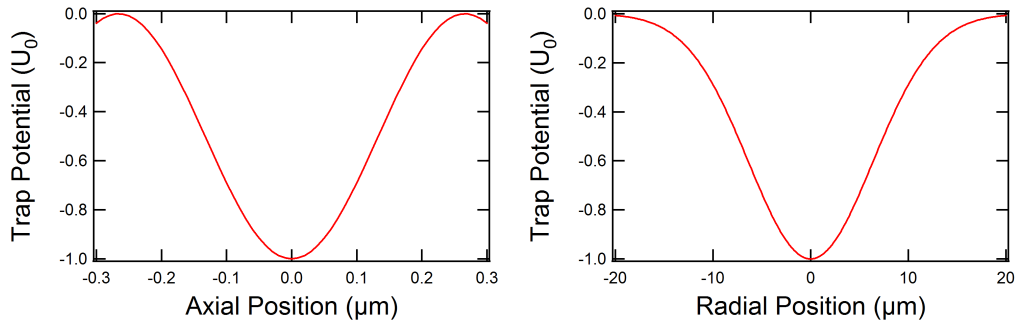

Figure 6.1: Trap profile of the simulated dipole trap in the axial (z) and radial (x,y) directions. For each time period (10 ns), the force on the atom is calculated from the potential at its location, and the atom's velocity is updated accordingly.

shown in Figure 6.1. For each calculation time-step (typically 10 ns), the probability of excitation is determined by the probe intensity, the probe detuning, the AC Stark shift of the transition (at the atom's current position in the trap), and the velocity of the atom (via the Doppler shift). For each excitation and emission cycle, the resulting change in the atom's velocity is determined (randomly). For each time period, there is also a small chance of an off-resonant excitation to the $F' = 2$ level. No attempt is made to model m_F states, nor any effects of photon polarization, magnetic fields, or sub-Doppler cooling.

It is assumed that two counts are required to detect an atom. The single photon counting module has a dark current of about 100 counts per second. The minimum probability of receiving a false count even during a short (300 μs) pulse is 3%. However, the probability of receiving two false counts during the same period is much lower, around 0.1%. Therefore, if the photon counter receives two counts within the pulse time, this should be sufficient to reliably report a detected atom. In an actual experiment, counts from background scatter become relevant as well, as will be discussed later.

The simulation was performed for a number of experimental parameters including

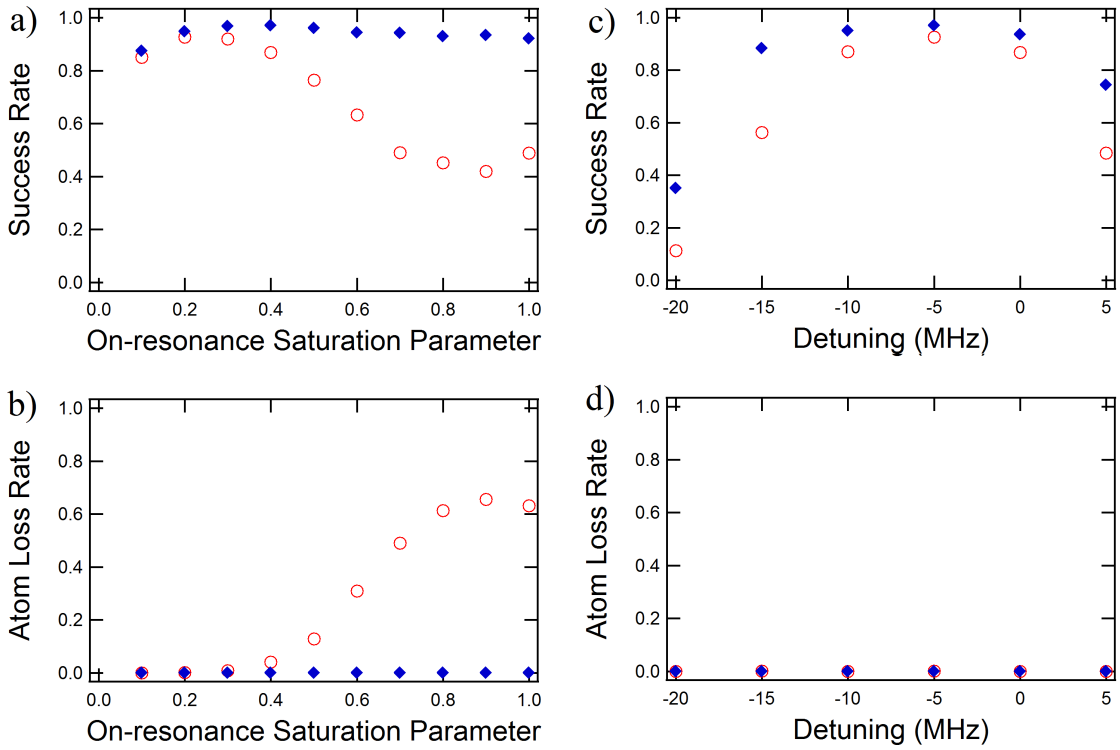

Figure 6.2: Sample graphs of simulation results. Red circles and blue diamonds indicate 1 mK and 2 mK trap depth, respectively. (a) Probability of successfully detecting at least two photons, versus probe intensity, for a -5 MHz probe detuning. (b) Probability of losing the atom from the trap before detecting two photons, versus probe intensity, for a -5 MHz probe detuning. (c) Probability of successfully detecting at least two photons, versus detuning, for a probe with $s_0 = 0.2$ (for the 1 mK trap) or $s_0 = 0.4$ (for the 2 mK trap). (d) Probability of losing the atom from the trap before detecting two photons, versus detuning, for a probe with $s_0 = 0.2$ (for the 1 mK trap) or $s_0 = 0.4$ (for the 2 mK trap).

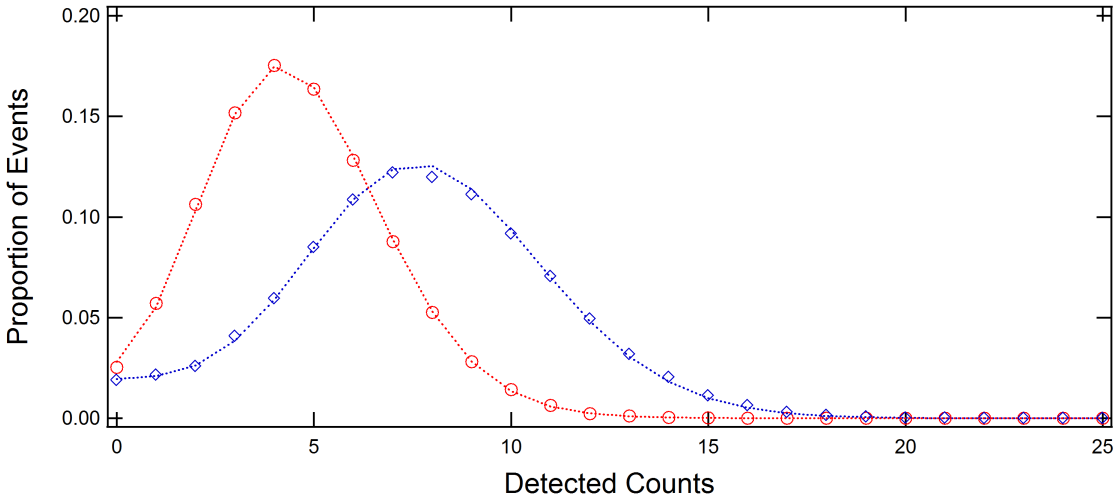

Figure 6.3: Histogram of detected counts, obtained by running the simulation 100,000 times. Red circles and blue diamonds indicate 1 mK and 2 mK trap depth, respectively. Dotted lines show the predicted distribution, assuming Poissonian statistics with a constant depump probability.

probe power, probe length, probe detuning, and trap depth. It was found that changing probe power vs. changing probe length produces equivalent results over a large range of values. Based on this finding, the probe length was held constant at $t = 300\ \mu$s. This value was chosen because it allows us to collect sufficient photons using a probe well below saturation intensity, while still keeping predicted errors due to dark counts below 0.1%. The other three parameters interact in a more complex way. A thorough three parameter search was performed in order to determine the ideal theoretical values for each parameter. A sample of the results is shown in Figure 6.2. After choosing specific values for probe power and detuning (for $U_0 = 1$ mK, $s_0 = 0.2$ and $\delta = -5$ MHz; for $U_0 = 2$ mK, $s_0 = 0.4$ and $\delta = -5$ MHz), the simulation was run for a much larger number of cycles, producing a histogram (Figure 6.3) of the number of counts before the atom either leaves the trap or falls into the dark state.

The numerical results indicated that, for the chosen experimental parameters, it should be possible to obtain error rates lower than 5% for a 2 mK trap depth, with negligible loss rates. Out of 1,000,000 runs, the atom was detected successfully 959,719

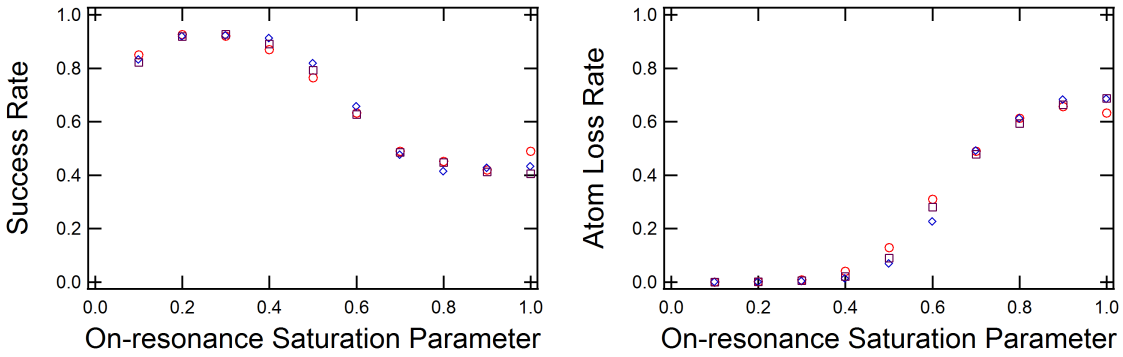

Figure 6.4: Success and loss rate versus saturation parameter for three different beam configurations. Red circles indicate a balanced probe beam in the x (radial) direction. Blue diamonds indicate a balance probe in the z (axial) direction. Purple squares indicate probe beams in both directions. For these data, the trap depth was set to 1 mK, with -5MHz detuning.

times, and the atom was lost from the trap only 2 times. The errors are primarily due to atoms becoming off-resonantly depumped into the $F = 1$ state before sufficient photons are detected. In order to further understand the system, a balanced probe beam was also added along the z (axial) direction, either instead of or in addition to the probe along the x direction. There was no significant effect due to switching the probe axis (see Figure 6.4). No probe beam was added along the y (radial) axis because constraints in the experimental apparatus make such a beam impractical.

6.3 Experimental Setup

We now turn to a description of the experimental setup and results. The system uses a modified version of the experimental setup used for pulsed cooling. First, the diameters of the MOT beams are reduced to <2 mm to minimize scattered light. Although the MOT lasers are off during state detection, low background scatter is nevertheless desirable in order to reliably determine the number and position of atoms in the trap. This also reduces the loading rate substantially. A balanced probe beam with linear polarization is added along one direction, focused to 125 μm at the center of the MOT. A beam sampler is added between the microscope objective and the

CCD camera, such that only 5% of the fluorescence goes to the camera. The rest of the light is directed to a PerkinElmer single photon counting module (model SPCM-AQR-14) with an efficiency of around 45%. The total detection efficiency η (of the single photon counting module) is given by

$$\eta = \left(\frac{NA}{2}\right)^2 \times \eta_{PBS} \times \eta_{filter} \times \eta_{detector} = 0.04 \times 0.95 \times 0.9 \times 0.45 = 0.015 = 1.5\%.$$

The magnification of the image on the photon counter is 2.5x, and the photon counter has an active radius of 85 μm. This produces a total field of view of radius 34 μm. The photon counter's field of view is centered on the high gradient MOT.

6.4 Loading a Single Atom

A timeline of the experimental procedure is shown in Figure 6.5. To begin, the MOT lasers (detuning = -10 MHz), a 110 G/cm magnetic field gradient, and a 2 mK optical lattice are all turned on simultaneously. The high gradient MOT is loaded for about 2 s, capturing an average of one atom, which is transferred to the optical lattice. At the end of the loading time, the magnetic gradient is turned off and the MOT lasers are shifted 10 MHz further from resonance to maximize continuous cooling. The trap is then imaged by the CCD camera for an exposure time of 1 s to determine if a single atom has been successfully loaded.

Figure 6.6 shows typical pictures of the loading. The number of atoms in the trap is determined using an algorithm which scans the CCD image for signals significantly above the noise. The resulting data show a background noise level (standard deviation) of 125 counts, and a single atom signal of about 1000 $\pm$200 counts. Figure 6.7 shows the probability of detecting a signal at a given number of counts. Based on these data, a cutoff is applied at 500 counts. Anything below the cutoff is assumed to be noise, and anything above the cutoff is assumed to be an atomic signal. Any signal above 1400 counts is not used, due to the likelihood of having more than one atom in approximately the same location. The cutoff is 4 standard deviations above

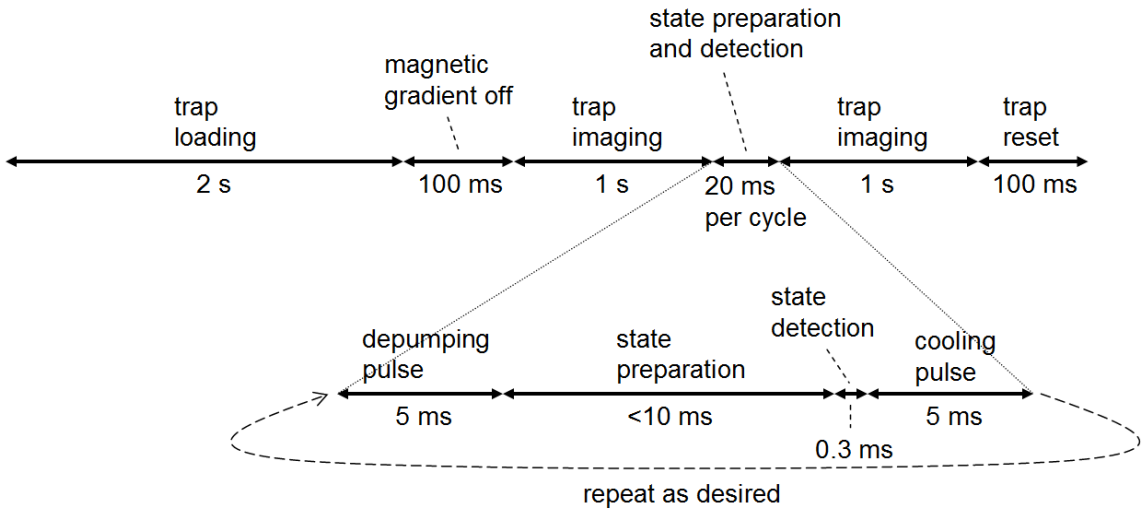

Figure 6.5: A timeline of the experiment. Atoms are loaded into the MOT for 2 s, trapping an average of one atom. The magnetic gradient is turned off, leaving the atom trapped in the lattice. 100 ms later, the trap is imaged by the camera, with an exposure time of 1 s. This determines whether there is exactly one atom in the trap. Then the MOT repump laser is turned off, followed 5 ms later by the trapping laser. This transfers the atoms into the $(F = 1)$ dark state. Next, the state of the atoms is prepared using either optical pumping or a microwave pulse. The state of the atom is detected non-destructively using a photon counter and a weak probe beam. The atom is then re-cooled for 5 ms using the MOT lasers. This preparation-detection cycle can be repeated as many times as desired. Once all cycles are complete, the trap is imaged once more by the camera to determine whether the atom survived all of the detection cycles. Finally, the trap is emptied in preparation for the next run.

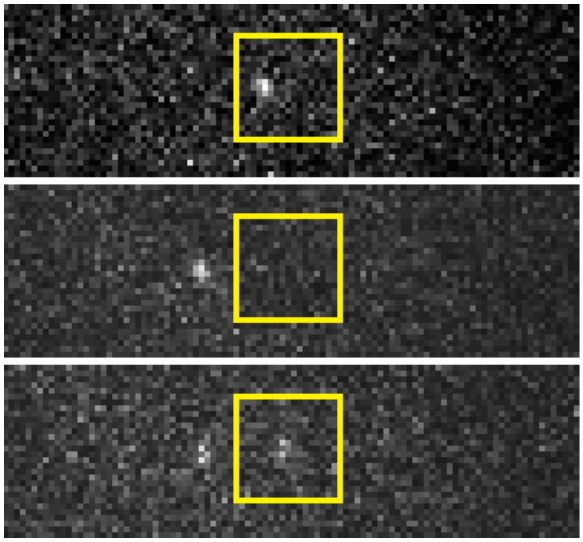

Figure 6.6: Images of different loading configurations. The top image shows a single atom loaded into the area of interest. The middle image shows an atom loaded outside of the area of interest. The bottom image shows two atoms loaded, one of which is in the area of interest. Of these, only the top image is considered to be successful trap loading.

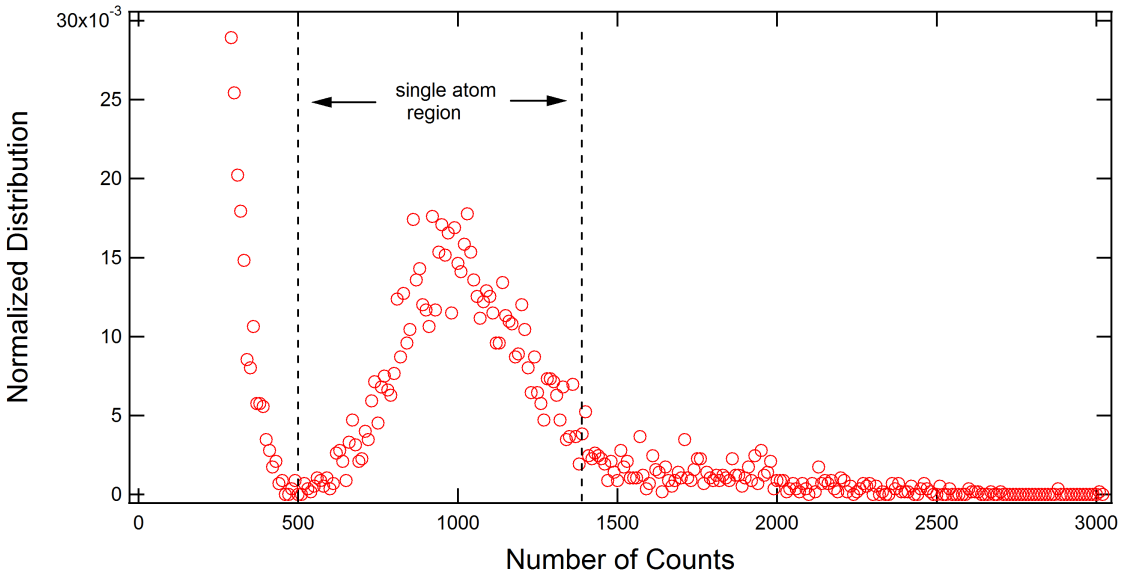

Figure 6.7: Distribution of detected counts from potential single atom signals. Any signal below 500 counts is treated as noise and ignored. Any signal above 1400 counts is assumed to be caused by multiple nearby atoms, and is discarded. Signals between 500 and 1400 counts are treated as single atoms.

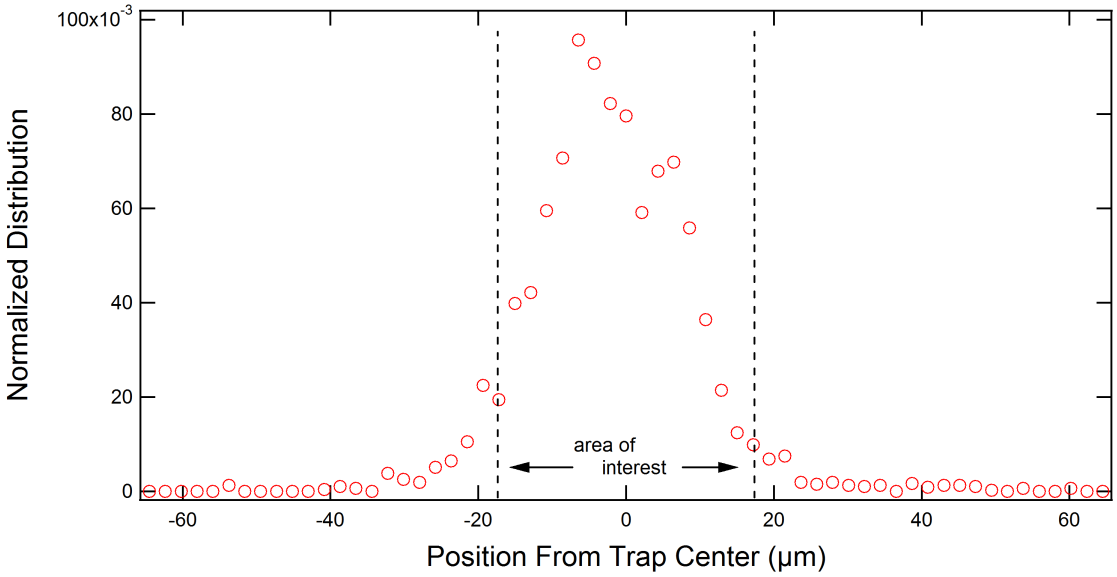

Figure 6.8: Spatial distribution of single atoms loaded into the trap. The dotted lines denote the area of interest.

the noise and 2.5 standard deviations below the average signal, yielding a probability of erroneously identifying a single atom of around 0.6%. Figure 6.8 shows the probability distribution for where the atoms load in the trap. If exactly one atom is loaded within the area of interest, and none outside of it, loading is considered successful. The area of interest is defined as the center half of the field of view, or the portion of the trap within 17 μm of the center of the MOT, and contains approximately 68 lattice sites.

The measured probabilities for loading a given number of atoms are shown in Figure 6.9. The probability of loading exactly one atom is 39%. Combined with a 10% probability of the atom appearing outside of the area of interest, the total success probability is measured to be 35%. These values vary slightly from day to day.

6.5 State Preparation and Detection

Once a single atom is successfully loaded into the region of interest, optical pumping is used to prepare it in the desired quantum state. For initial experiments, we ignore

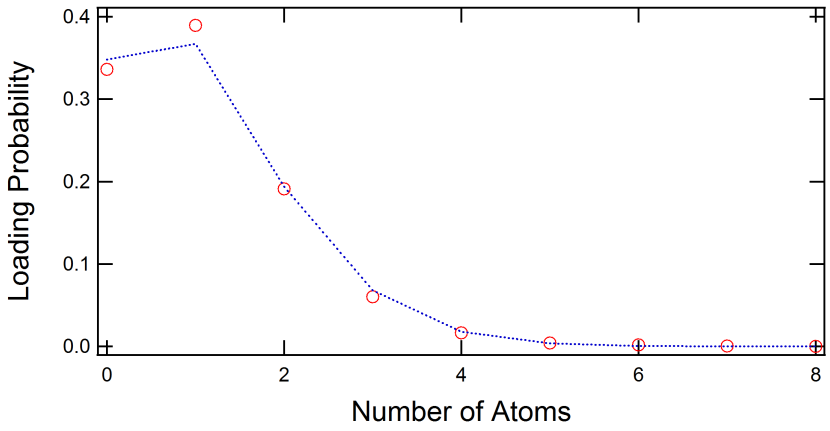

Figure 6.9: Probability of loading N atoms. The dotted line shows the expected Poisson distribution. The measured probability of loading exactly one atom is 38.9%.

the Zeeman structure and consider the qubit states to be the $F = 1$ and $F = 2$ hyperfine levels separated in energy by 6.8 GHz. The atom is prepared in either the $F = 1$ or $F = 2$ state by applying a 10 ms pulse of either the MOT cooling lasers or the repump laser.

Quantum state readout is performed using two 6 μW counter-propagating probe beams, focused to 125 μm and detuned +5 MHz from $F = 2 \rightarrow F' = 3$ transition. This produces an on-resonance saturation parameter $s_0 = 4$, although the effective saturation is much lower due to the differential Stark shift. The fluorescence is detected by the photon counter, and the resulting number of counts is recorded.

The detuning of +5 MHz was chosen empirically. According to our calculations, the Stark shift should be +155 MHz, which means our simulation predicts an optimal detuning of +150 MHz. However, we found that detunings larger than about +10 MHz caused significant heating and loss from the trap. Experimentally, we found that a detuning of +5 MHz maximized the total number of counts obtained from the atoms. This suggests that the Stark shift may be significantly smaller than expected. This discrepancy will be discussed at the end of this section.

Once the state of the atom has been determined, the MOT cooling lasers are

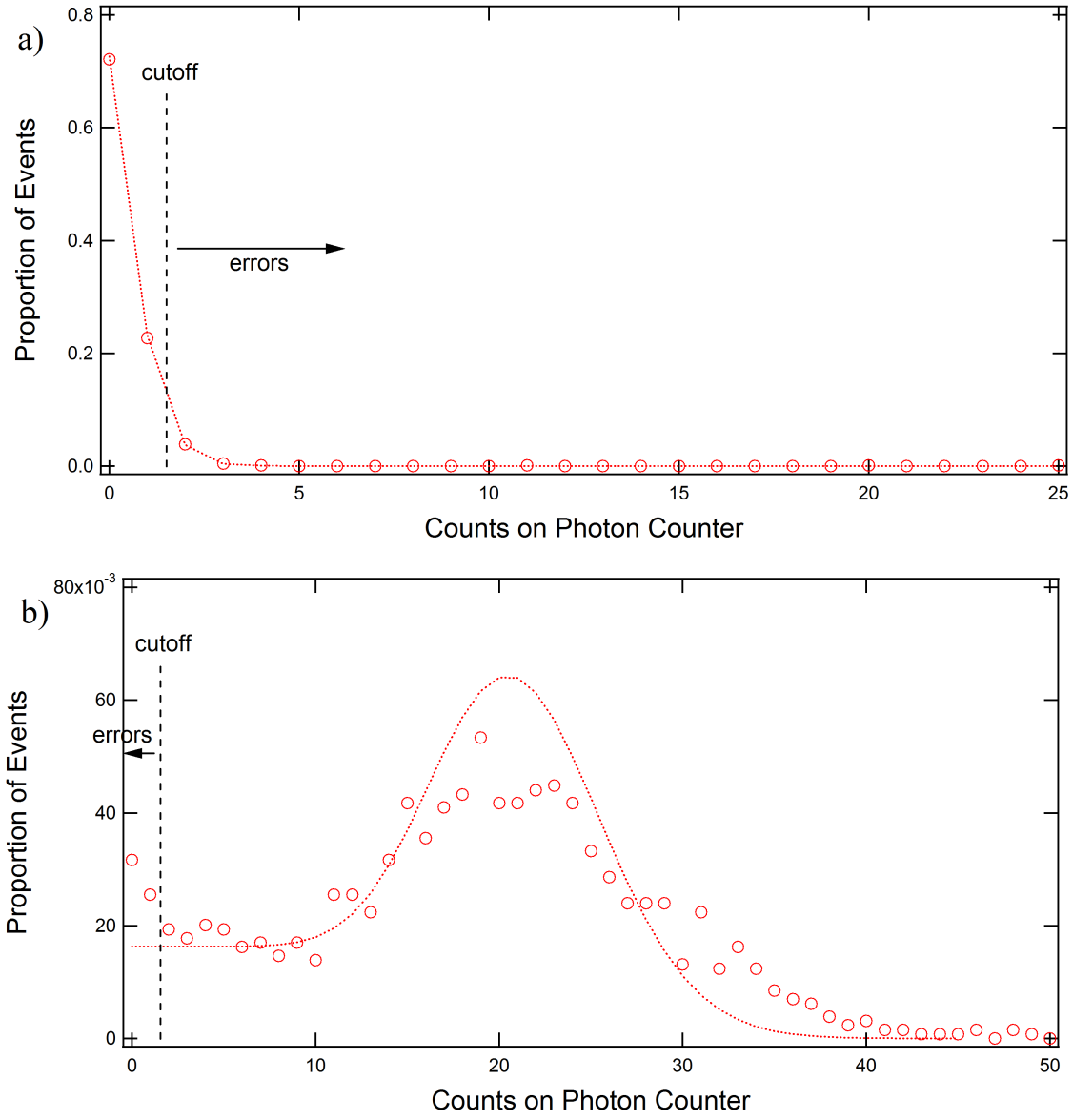

Figure 6.10: Histogram of counts per atom. (a) Atoms were prepared in the $F = 1$ hyperfine ground state and detected on the $F = 2 \rightarrow F' = 3$ transition. The dotted red line is a Poisson distribution with an average of 0.32 counts. The dotted black line shows the cutoff between one and two counts. Any signal above one count represents an error. (b) Atoms were prepared in the $F = 2$ hyperfine ground state and detected on the $F = 2 \rightarrow F' = 3$ transition. The dotted red line is a modified Poisson distribution, with an average of 21.5 counts, and with a uniform probability (total p = .35) of depumping into the dark state. The dotted black line shows the cutoff between one and two counts. Any signal below two counts represents an error.

turned back on, and the CCD camera takes another picture of the trap. This image is used to determine whether the atom has remained trapped. This process was repeated over 1600 times for each of the two initial states. Figure 6.10 shows the distribution of total counts on the single photon counter for atoms prepared in the $F = 1$ and $F = 2$ states respectively. For a fixed probe time of 300 μs, the average number of collected photons from the $F = 2$ state was measured to be $\bar{m} = 21$ and from the $F = 1$ state is $\bar{m} = 0.3$.

The histogram is used to select a cutoff at 2 counts, as in the simulation described previously. A signal of less than two counts is considered to be noise, while a signal of 2 or more counts is assumed to be a legitimate detection. Two types of errors are possible. The $F = 1$ error rate is defined as the probability of falsely detecting the atom in the $F = 2$ state when it was prepared in the $F = 1$ state. The $F = 2$ error rate is the probability of failing to detect an atom that was prepared in the $F = 2$ state. The data in the histogram gives error rates of 4.5% and 5.7% for $F = 1$ and $F = 2$ respectively. Naively, one might expect both graphs to approximate a Poisson distribution. However, the $F = 2$ graph deviates significantly. In particular, there is an additional peak at zero counts. This is due partially to failed state preparation and partially to the possibility of depumping into the $F = 1$ state before the end of the pulse. Also, the main peak is somewhat wider than expected. We believe this is because some atoms leave the trap before the end of the cooling pulse.

Since the cutoff for detecting a single atom has been set to two counts, this means that any additional counts received by the photon counter beyond the first two have no effect on the outcome. Our system monitors the output of the photon counter in real time, as the atom is being probed. As soon as two counts have been received, the atom is considered to be in the $F = 2$ state. At this point, no further counts are necessary to determine the state of the atom, and the probe beam can be shut off without losing any information. This minimizes the extent to which the probe beam

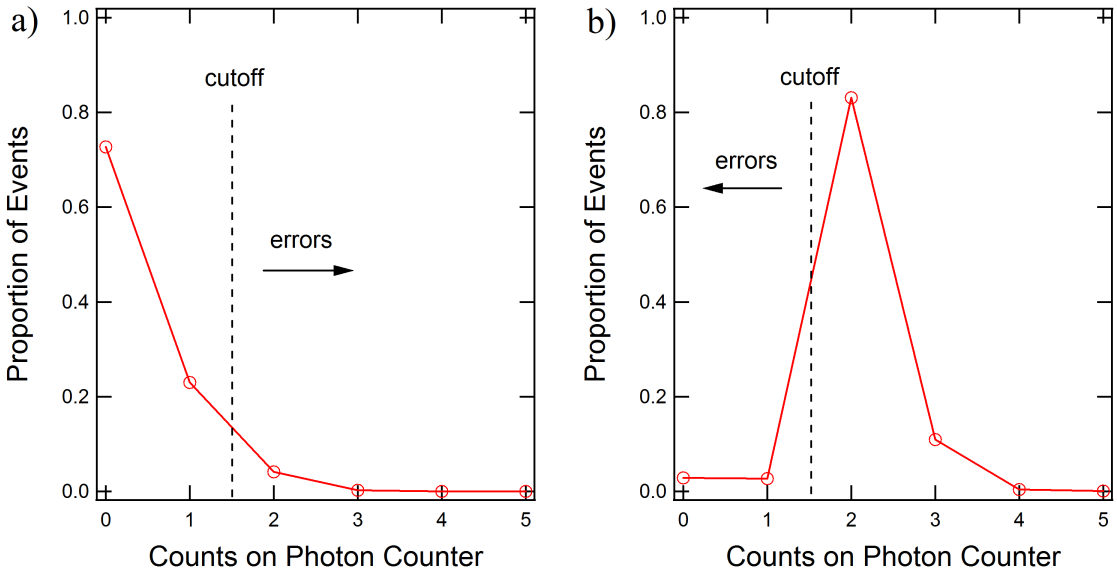

Figure 6.11: Histogram of counts per atom, where the probe was extinguished after the photon counter had reported two counts. (a) Atoms were prepared in the $F = 1$ hyperfine ground state and detected on the $F = 2 \rightarrow F' = 3$ transition. The dotted black line shows the cutoff between one and two counts. Any signal above one count represents an error. (b) Atoms were prepared in the $F = 2$ hyperfine ground state and detected on the $F = 2 \rightarrow F' = 3$ transition. The dotted black line shows the cutoff between one and two counts. Any signal below two counts represents an error.

disturbs the atom, while having no effect on the final outcome of the measurement. This two-photon shutoff is implemented by monitoring the output of the photon counting module. Once two pulses are received, an RF switch is triggered, which shuts off RF power to the AOM controlling the probe beam. The shutoff time is primarily limited by the response of the AOM, which is less than 1 μs.

Similar data to Figure 6.10, but with the two photon shutoff, is shown in Figure 6.11. As expected, the $F = 1$ histogram is not significantly different, while the $F = 2$ histogram shows a huge peak at two counts, followed by a steep cutoff. The instances in which three counts are detected are due either to dark counts on the photon counter or to background scatter from sources other than the probe beam. The data in Figure 6.11 gives error rates of 4% and 5.5% for $F = 1$ and $F = 2$ respectively. The measured atom loss rates were 0.9% for $F = 1$ and 1.05% for $F = 2$. These results

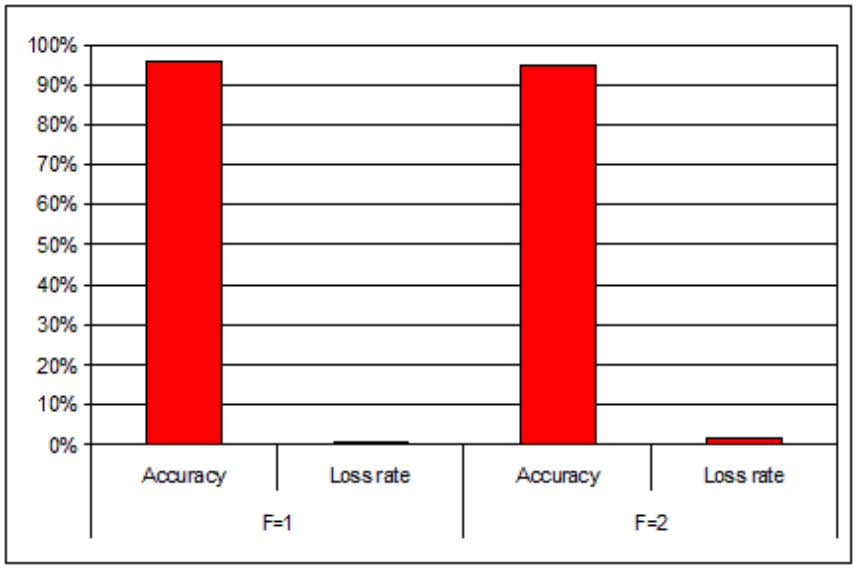

Figure 6.12: Accuracy and loss rate for detection of the hyperfine ground states. For the $F = 1$ initial state ($n = 1684$ data points), the accuracy was 96% and the loss rate was 0.9%. For the $F = 2$ initial state ($n = 2127$ data points), the accuracy was 94.5% and the loss rate was 1.05%.

are shown graphically in Figure 6.12.

The $F = 1$ error rate is almost entirely due to the probe beam scattering off of the sides of the glass cell. If that source of noise could be eliminated (for example, by using an AR-coated cell), only the dark counts of the photon counter would remain, giving a predicted error rate of ≈0.1%. The $F = 2$ error rate is due primarily to depumping into the $F = 1$ state, which is more difficult to address. Methods of reducing these errors will be discussed later. The $F = 1$ loss rate is due to a combination of losses from background collisions ($p \approx 0.35\%$ for a 300 s lifetime) and single atom detection errors ($p \approx 0.6\%$, as discussed previously). The $F = 2$ loss rate is slightly larger, presumably due to the perturbation from the probe beam. This loss rate is much higher than the loss rate predicted by the simulation. Several possible reasons exist for this discrepency. If the two probe beams have slightly different intensities, the resulting force imbalance would tend to push atoms out of the trap. Also, any slight misalignment of the lattice could result in a trap depth lower than the calculated

value.

The $F = 2$ error and loss rates can be further examined by observing their dependence on the various experimental parameters. $F = 2$ errors can be caused by depumping, insufficient scattering events, or loss of the atom. The first two types of errors should be affected directly by the probe detuning and probe power and indirectly by the trap depth, due to the effects of the differential Stark shift. The $F = 2$ loss rate should depend on trap depth and probe detuning, but should be mostly independent of probe power, because the probe beam is shut off after the atom has scattered enough photons to detect two counts.

The experiment was repeated for different values of trap depth, probe detuning and probe power. The results can be seen in Figure 6.13. As shown in Figure 6.13(a), reducing the probe power reduced the chance of detecting two photons before the pulse ended, and thus increased the $F = 2$ error rate. It had no significant effect on the loss rate. Figure 6.13(b) shows the effect of changing trap depth. For a shallow trap depth, the loss rate was extremely high. As the trap became deeper, the loss rate dropped quickly at first, and then appeared to asymptote towards about 1%. The $F = 2$ error rate followed a similar curve. Figure 6.13(c) shows the effect of changing the probe detuning. Detuning the probe further to the red of resonance increased the cooling effect of the beam, decreased the scattering rate, and increased the chance of depumping into the $F = 1$ state. This reduced the $F = 2$ loss rate, but increased the $F = 2$ error rate. If the probe was tuned too far blue, the $F = 2$ loss rate increased dramatically.

All relevant detunings have been reported with respect to the bare atomic resonance, ignoring the effects of the differential Stark shift. As mentioned earlier, the simulation predicted an ideal detuning of +150 MHz, due to the effects of the Stark shift, whereas the best detuning experimentally was +5 MHz. In order to reconcile these values, an attempt was made to measure the differential Stark shift. A single

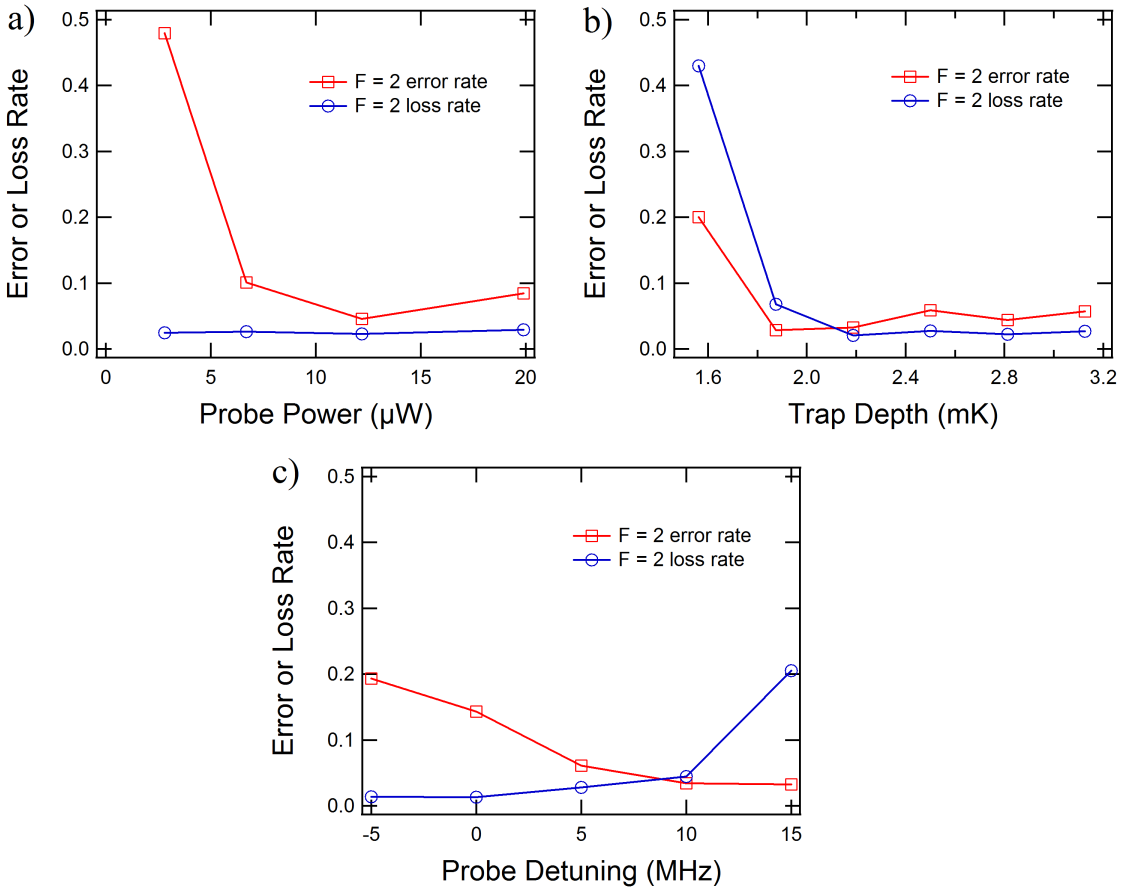

Figure 6.13: Error rates and loss rates for different experimental settings. (a) Error and loss rate versus probe power, for 2.5 mK trap depth and 5 MHz probe detuning. (b) Error and loss rate versus trap depth, for 12 μW probe power and 5 MHz probe detuning. (c) Error and loss rate versus probe detuning, for 12 μW probe power and 2.5 mK trap depth.

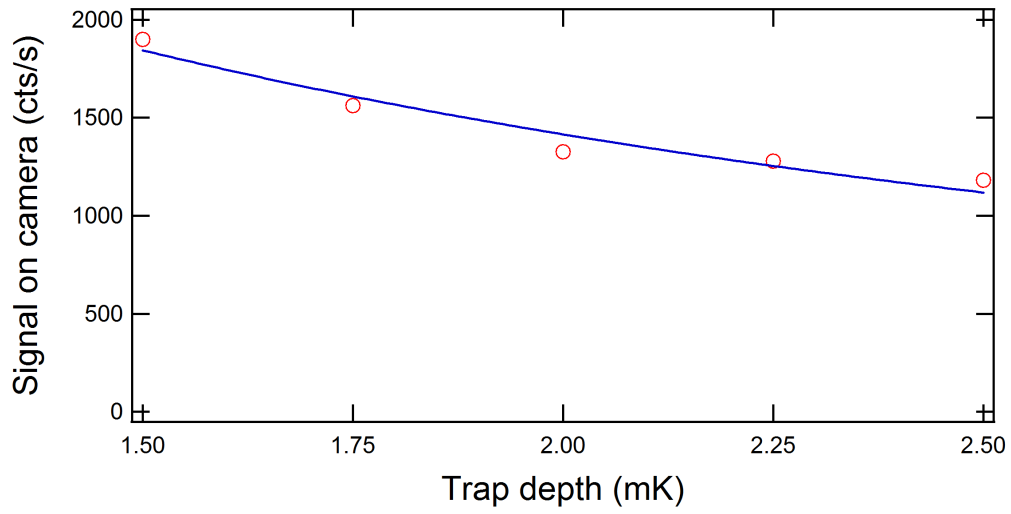

Figure 6.14: Single photon fluorescence versus trap depth. The differential Stark shift increases linearly with the trap depth, leading to a larger effective detuning of the cooling light from resonance. As the effective detuning increases, the fluorescence rate decreases. The solid blue line shows a theoretical fit to the data, which gives a differential Stark shift of 11.1 MHz per 1 mK trap depth.

atom was trapped and cooled for a variety of different trap depths ranging from 1.5 mK to 2.5 mK. The resulting fluorescence signals under continuous cooling are shown in Figure 6.14. The relationship between the number of counts detected and the trap depth is given by [34],

$$N_{cts}(U_0) = A\frac{s_0}{1 + s_0 + \frac{4(U_0\delta' + \delta)^2}{\Gamma^2}}, \tag{6.1}$$

where $s_0 = 10$ is the on resonance saturation parameter, $\delta = 20$ MHz is the detuning from the unshifted resonance, U_0 is the trap depth, δ' is the differential Stark shift per unit trap depth, and A depends on the atomic linewidth and detection efficiency. A fit to these data points gives an average differential Stark shift of 11.1 $\pm$ 2.8 MHz per 1 mK trap depth.

The measured value of the Stark shift is averaged over the atom's movement in the trap and should therefore be somewhat smaller than the calculated value. However, this is far too small an effect to account for the factor of seven discrepancy between the calculated and measured values. Our assumption, therefore, is that the trap depth

must actually be significantly smaller than the calculated value, perhaps by as much as a factor of four. This conclusion is also supported by the discrepancy between the calculated and measured values of the trap frequency, reported in Chapter 5. A smaller trap depth would also explain why the qubit loss rates tend to be much higher than in the simulation.

There are a few reasons why the trap depth might be smaller than the calculated value. The calculations assume an ideal focusing lens and perfect alignment, which are difficult to achieve. Furthermore, the trapping laser is focused through a glass cell, which might affect the quality of the focus. Future improvements to the alignment and focus of the optical lattice might improve the accuracy and repeatability of these detection techniques.

6.6 Repeated Measurements

The measured loss rates are low enough to enable preparation and detection of each atom many times before losing it from the trap. In order to test this, the experimental procedure was modified. After loading an atom and detecting it with the camera, the atom was prepared in the $F = 1$ or $F = 2$ state, and measured as before. Directly following state detection, the atom was cooled for 5 ms to counter the heating associated with the detection process. The atom was then immediately prepared in the desired state and the state measured again. This was repeated fifty times with each atom, before taking a final picture with the camera, to confirm whether the atom had survived all fifty cycles. The total time per cycle was 20 ms. The error rates for these measurements were 5.9% for $F = 2$ and 6.6% for $F = 1$, which roughly agreed with the earlier results.

The $F = 1$ loss rate was not significantly affected by the number of cycles, as expected. The $F = 2$ loss rate was 31.4% for fifty cycles. Figure 6.15(a) shows the probability of detecting an atom in $F = 2$ versus the cycle number. The curve

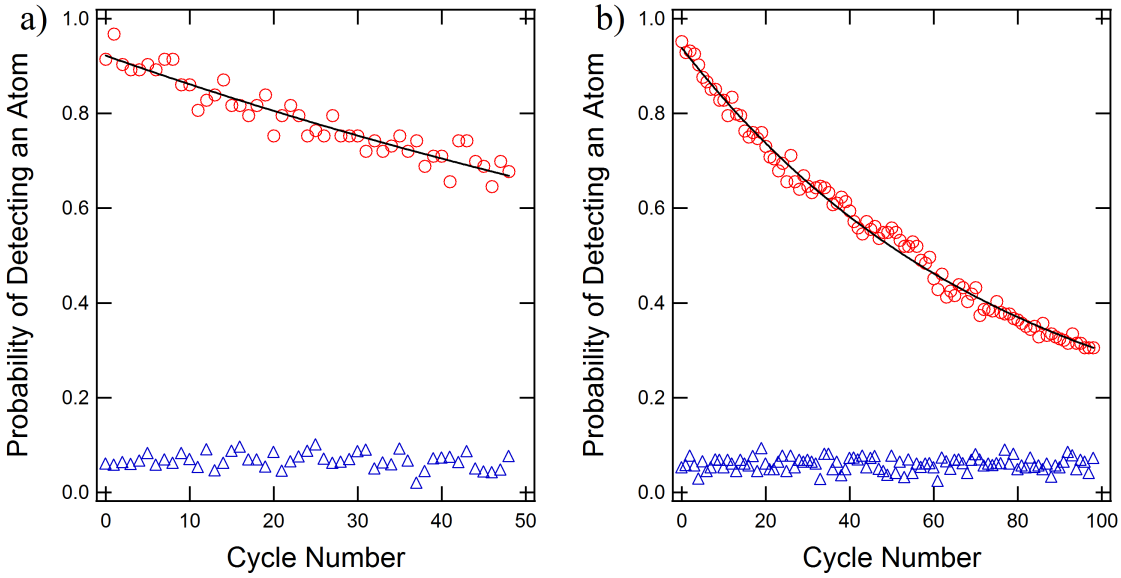

Figure 6.15: Probability of a single atom being detected during the Nth preparation and detection cycle. (a) Each atom is prepared and detected fifty times in the $F = 2$ state. The red circles show the probability of the atom being detected in the trap for each cycle. An exponential fit (solid line) gives a decay lifetime of 137 cycles, suggesting a loss probability of 0.73% per cycle. The blue triangles show detection probabilities if the atom is instead prepared in the $F = 1$ state. (b) Each atom is prepared and detected one hundred times in the $F = 2$ state. An exponential fit (solid line) gives a decay lifetime of 77 cycles, suggesting a loss probability of 1.3% per cycle. The blue triangles show detection probabilities if the atom is instead prepared in the $F = 1$ state.

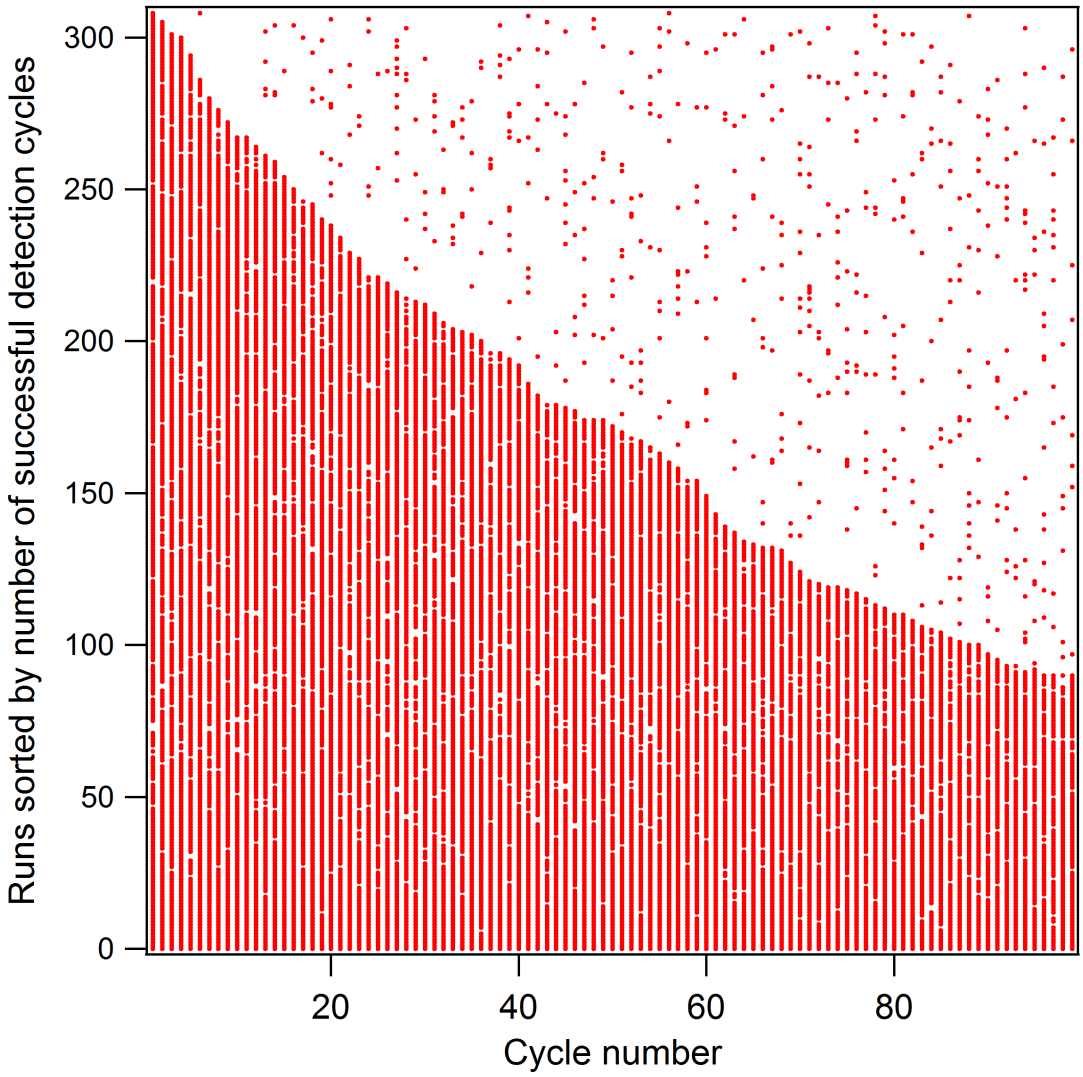

Figure 6.16: 308 individual atom runs. For each run, a single atom is prepared in the $F = 2$ state and then detected, repeated for 100 cycles. The dots correspond to a positive detection of the atom in the $F = 2$ state. The runs are numbered in order by how long the atom remained in the trap.

closely fits an exponential with a time constant of 137 cycles, giving a loss per cycle of 0.73%. In order to obtain a more complete exponential curve, the experiment was later repeated with 100 cycles per trapped atom. The corresponding graph is shown in Figure 6.15(b). Note that these data were taken on a different day, resulting in a small variation of the error and loss rates. A fit to the 100 cycle data indicated a 77 cycle lifetime, corresponding to a 1.3% loss per cycle. In Figure 6.16, each row corresponds to the series of state measurements of a single atom prepared in the $F = 2$ state and the dots correspond to a positive detection of the atom in the $F = 2$ state. The individual atom runs are sorted in order by how long the atom remained in the trap in order to illustrate the atom loss probability. The missing dots on the lower part of the graph indicate $F = 2$ errors, while the stray dots on the upper part of the graph indicate $F = 1$ errors. The shape of the data envelope reveals the atom loss probability.

6.7 Microwave State Preparation

State preparation to the $F = 1$ or $F = 2$ quantum states as used above provides a technically expedient method to assess the performance of quantum state detection. Of course, for useful applications to quantum information, we are interested in measuring qubits of arbitrary superpositions of the two states. Unfortunately, such methods are also generally more complicated to achieve. As a first demonstration, we will apply our technique to measure qubits created using microwave rotations between the two hyperfine states.

The experimental sequence is very similar to the previous section except that the atom is initialized to the $F = 1$ state and then excited to a superposition of the $F = 1$ and $F = 2$ states using a pulse of microwave radiation tuned to the $F = 1 \rightarrow F = 2$ hyperfine transition. The apparatus used to generate the microwaves is shown in Figure 6.17. A 3.417 GHz signal is supplied by a high-frequency function

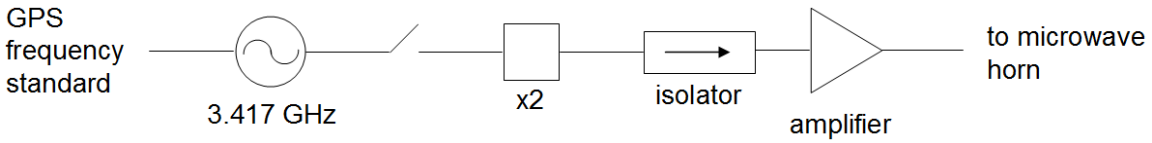

Figure 6.17: Experimental apparatus used to generate microwave pulses. A 3.417 GHz signal is supplied by a high-frequency function generator phase-locked to a GPS frequency reference. An RF switch is used to toggle the signal on and off. The signal passes through a frequency doubler, a microwave isolator, and then a 20 W power amplifier. The output is broadcast using a microwave horn.

generator (model HP E4422B), which is phase-locked to a 10 MHz GPS-synchronized frequency reference. An RF switch is used to toggle the signal on and off. The signal passes through a frequency doubler, which changes the frequency to 6.835 GHz. A microwave isolator prevents reflection back into the frequency doubler. Finally, the signal is fed into a 20 W power amplifier, and the output of the amplifier goes to a microwave horn directed toward the atom trap. The resulting microwaves excite the $F = 1, m_F = 0 \rightarrow F = 2, m_F = 0$ magnetic dipole transition, resulting in a population inversion which is dependent on the pulse length, as was discussed in Chapter 3.

In this experiment, the maximum probability of transferring the atom to the $F = 2$ state should be approximately 1/3, due to the multiplicity of the Zeeman states that we have so far ignored. The state preparation to the $F = 1$ initial state should equally populate the three $F = 1, m_F = 0$ Zeeman states. On the other hand, the microwave radiation is tuned to the $F = 1, m_F = 0 \rightarrow F = 2, m_F = 0$ clock transition, which is insensitive to magnetic fields to first order. The microwave radiation is not resonant with transitions from the $F = 1, m_F = \pm 1$ Zeeman states to the $F = 2$ states, due to Zeeman shifts, so these states are not excited.

For each atom loaded, fifty preparation and detection cycles were run, with a variable microwave pulse length proportional to the cycle number. After running this on a large number of atoms, an average result was calculated for all of the atoms that

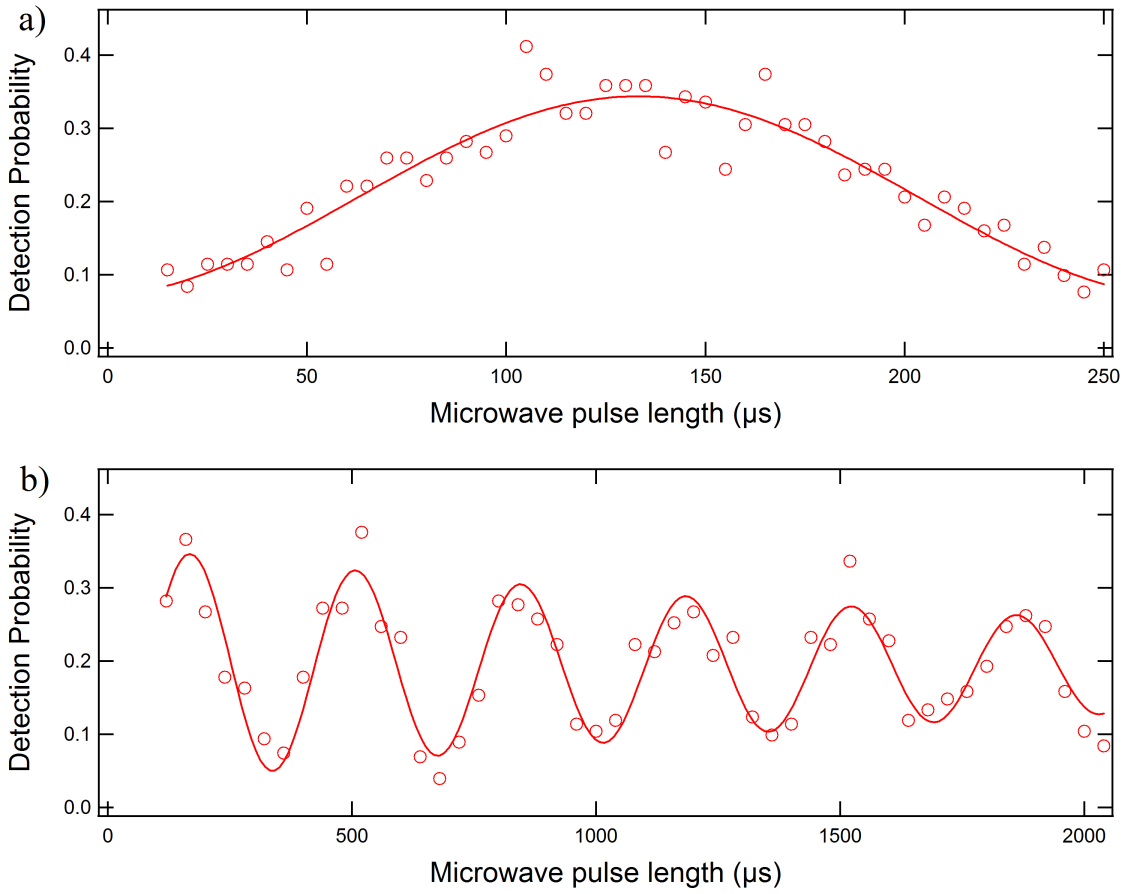

Figure 6.18: Graphs showing Rabi flopping. (a) Probability of detecting an atom in the $F = 2$ state as a function of the microwave pulse length. The graph shows most of one Rabi flop. The solid line is a fit to a sine wave. (b) Six Rabi flops. The solid line is a fit to an exponentially decaying sine wave. The fit gives a Rabi rate of 2.95 kHz and a decoherence time of 2.2 ms.

had remained in the trap until the end of their respective runs. Figure 6.18(a) shows the resulting Rabi flopping for microwave pulse lengths ranging from 10 μs to 250 μs. As predicted, the maximum probability of finding the atom in the $F = 2$ state is approximately 1/3. In order to estimate both the Rabi rate and the decoherence time, this measurement was repeated with a maximum microwave pulse length of 2000 μs (Figure 6.18(b)). A fit to the data matches a damped Rabi oscillation with a Rabi rate of 2.95 kHz and a decoherence time of 2.2 ms. For comparison, the differential Stark shift between the $F = 1$ and $F = 2$ hyperfine states is expected to cause a decoherence time of 1.5 ms for atoms at the Doppler temperature [65].

Thus far, we have discounted any off-resonant coupling from the $m_F = \pm 1$ states. For this experiment, we have minimized the magnetic bias field only so far as to ensure effective continuous observation. As discussed in the last chapter, continuous observation works well over a range of roughly $\pm$ 100 mG. It is therefore unlikely that the magnetic field at the trapping site is less than 10-30 mG. A 10 mG bias field would produce a Zeeman shift of 7 kHz, resulting in a generalized Rabi rate of 7.6 kHz for the $m_F = \pm 1$ states. This would add an additional sinusoidal term to the Rabi flopping graph with a frequency of 7.6 kHz and an amplitude about 6.5 times smaller than the $m_F = 0$ term. Such an effect is not visible in Figure 6.18, suggesting that the bias field is probably larger than 10 mG.

The versatility of this system is further demonstrated by obtaining a graph of two Rabi flops using only a single atom. For the first two graphs in Figure 6.19, a single atom was captured. The initial state was prepared using microwaves, and was then measured. This was repeated for fifty different microwave pulse lengths ranging from 10 to 500 μs, all with the same atom. Figure 6.19(c) shows the average of 312 such graphs.

Microwave transfer rates were limited to 1/3 in this experiment due to the extra Zeeman levels, but this limitation would be straightforward to address in future

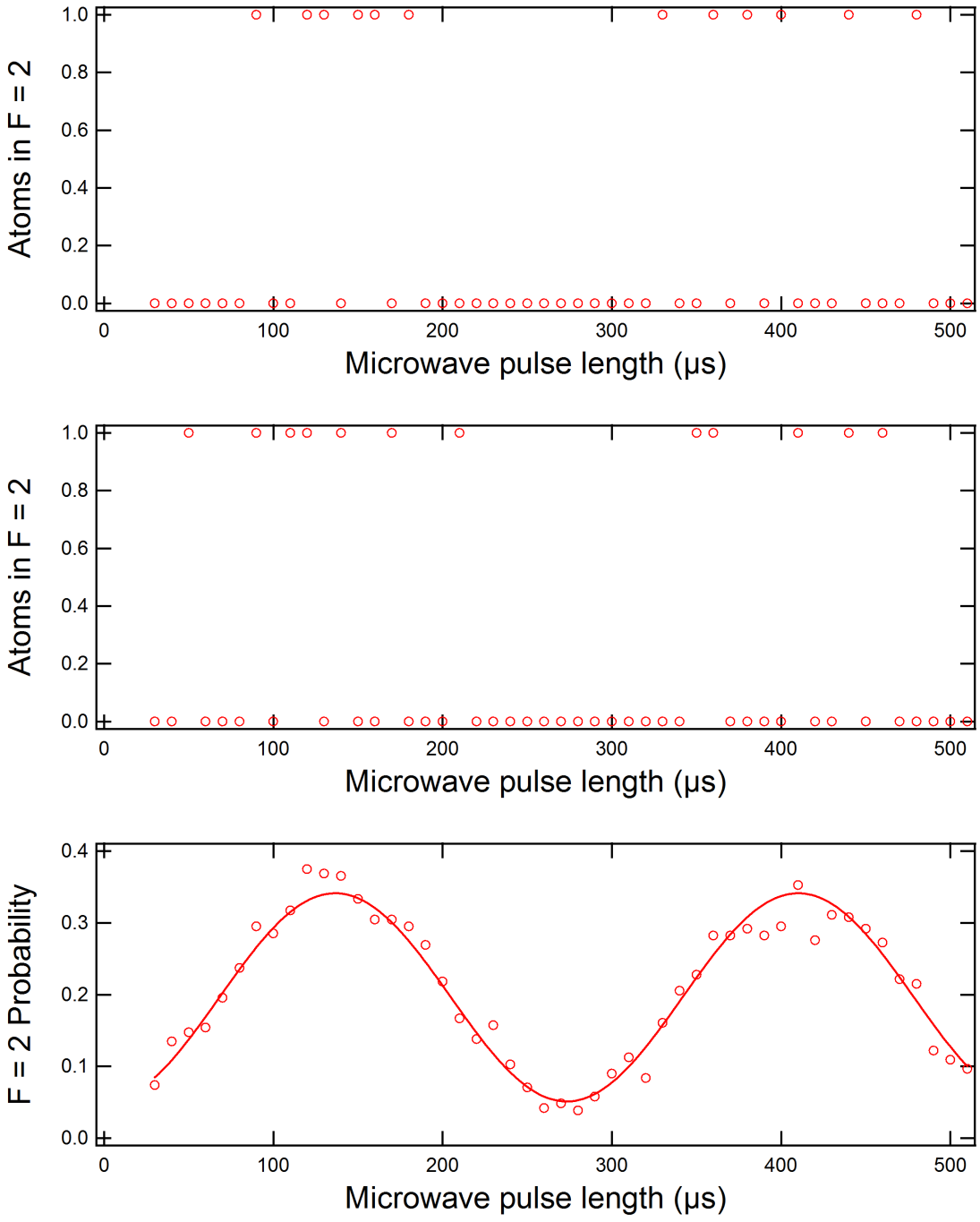

Figure 6.19: Rabi flops with single atoms. (a,b) An individual atom is prepared and detected fifty times, for fifty different microwave pulse lengths. (c) An average of 312 individual atom runs. The solid line is a sinusoidal fit to the data.

studies. A number of methods exist for preparing atoms in a specific m_F state, with optical pumping being perhaps the easiest. This is accomplished by applying a circularly polarized pump beam tuned to the $F = 1 \rightarrow F' = 0$ transition aligned along the magnetic field axis of the atoms. By conservation of angular momentum, any transition from the $F = 1, m_F = 0$ state becomes forbidden, causing the atom to (sooner or later) be pumped into that state. Once the atom is prepared in the $F = 1, m_F = 0$ state, microwaves could be used to transfer atoms to the $F = 2$ state (or any superposition of the two) with arbitrarily high efficiency.

6.8 Future Goals

One possible improvement to this experimental setup would be to add an additional microscope objective below the glass cell. Increasing the light to the camera by a factor of twenty could allow the exposure time to be reduced to 50 ms, which would significantly increase the repetition rate of the experiment. Several other methods would also work to improve the signal to noise ratio. Most obviously, switching to an AR coated glass cell would reduce the scattered light from the MOT lasers, thus reducing the background noise. Alternatively, a separate set of smaller (or focused) lasers could be used for continuous cooling. This would also allow the use of larger MOT beams, which would increase the loading rate for a single atom, and therefore also the repetition rate of the experiment.

Another possible option would be to remove the camera entirely and use the photon counter to confirm the presence of a single atom. Since the signal to the photon counter is twenty times larger than the signal to the camera, this seems like it might work well. In practice, it was found that this method introduced too much error into the process. As was seen in Figure 6.6, each atom appears only on a small number of pixels. The photon counter, however, sums over a much larger area, which significantly increases the background noise. The resulting signal to noise ratio is not

significantly better than is produced by the camera, given the same exposure time. Furthermore, the camera has the advantage of giving the approximate location of the atom in the trap, rather than just the number of atoms.

Much of the current error rate is due to accidental depumping of the atom to the $F = 1$ state via off-resonant excitation to the $F' = 2$ level. The results from the simulations show that this error is difficult to suppress due to the spatial variation of the AC Stark shift of the $F = 2 \rightarrow F' = 3$ transition. There are several strategies that we can pursue to address this issue that range in complexity. The most promising tactic is to employ a circularly polarized probe beam coaligned with a magnetic field to excite the $F = 2, m_F = 2 \rightarrow F' = 3, m_F = 3$ transition. This is a true closed (cycling) transition that should completely suppress off-resonant excitation to the $F' = 2$ level. Other possibilities include cooling the atoms to reduce the spatial variation of the shifts, minimizing shifts with compensating fields, and switching to a different trapping wavelength where the shifts are minimized [117, 118].

The current version of this experiment is limited to a single qubit, but there is no reason, in principle, that it couldn't be applied to a quantum register of arbitrary length. The first step would be to build a uniform quantum register. Although this could be done probabilistically, a uniform quantum register would require an amount of time to load that is exponential with register length. More reasonable strategies have been implemented by Miroshnychenko et al. [63], and have been discussed by others [76]. Once a quantum register is loaded into the lattice, the atoms can be moved along the trap axis using optical conveyor techniques [58]. By focusing the probe beam more tightly, it should be possible to read out only one atom at a time. Furthermore, if the atoms are prepared in an $m_F = \pm 1$ state, a magnetic field can be used to allow the microwaves to address only one atom at a time. Using a combination of these techniques, it should be straightforward to construct a robust, re-usable quantum register.

CHAPTER VII

PROGRESS ON A BLUE DETUNED 1-D OPTICAL LATTICE

The differential Stark shift between the $5S_{1/2}$ and $5P_{3/2}$ states creates a time varying frequency shift of the optical transition, which is large compared to the natural linewidth of the transition. Besides changing the effective detuning of the lasers, this can cause depumping and interfere with cooling, as discussed in the previous few chapters. Furthermore, differential Stark shifts between the two $5S_{1/2}$ hyperfine states produce decoherence, which is extremely undesirable in quantum information systems. Several methods exist for dealing with these problems, but each has its own limitations. Direct Stark shift cancellation is possible, but it requires an additional laser and very careful alignment [119]. Trapping at the magic wavelength is possible for some atoms, such as cesium, but it severely limits the choice of trapping lasers available [66]. A partial solution is to turn off the trapping laser briefly while addressing the atoms. Although this may help in some cases, it does not sufficiently address the problem, and can cause other issues such as atom loss.

A very promising solution to the differential Stark shift is to switch to a blue detuned dipole trap [120]. Blue detuned lasers repel atoms instead of attracting them, so the trapping geometry is typically more complicated. The atoms are held at the minimum of the light field, and must be enclosed on all sides in order to remain trapped. However, because the atoms are trapped in the area of minimum light, the Stark shift is zero at the center of the trap. 3-D blue detuned optical lattice traps have been demonstrated by several groups, and have been shown to reduce both the average Stark shift and the off-resonant scattering rate substantially [121]. Other trap

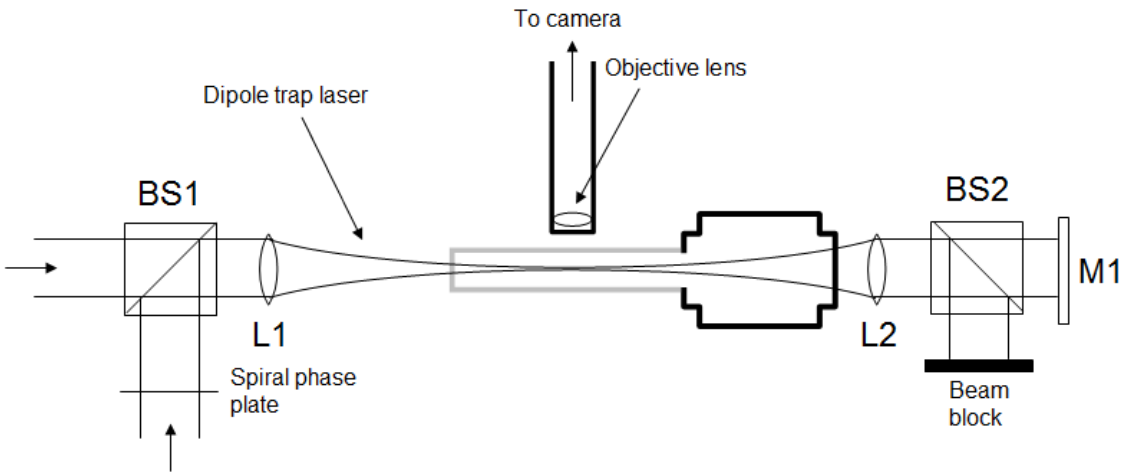

Figure 7.1: Experimental setup for a one dimensional blue detuned optical lattice. A blue detuned laser beam passes through a spiral phase plate, forming a ring beam at its focus. This beam is combined with a separate Gaussian beam on a polarizing beamsplitter cube (BS1), and both are focused onto the MOT. After exiting the chamber, the beams are split by a second polarizing beamsplitter cube (BS2). The ring beam is blocked, while the Gaussian beam is retro-reflected to form the lattice.

configurations, which produce only a single large trap site, have also been used [122]. In this chapter, we describe work aimed at developing a blue detuned 1-D lattice trap.

7.1 Experimental Setup

The proposed setup is shown in Figure 7.1. It uses a 1 W tapered amplifier pumped by a 776 nm diode laser to create two trapping beams, one with P =50 mW and the second with P =300 mW. The 50 mW trapping beam is oriented just like the red detuned lattice beam discussed previously. It is retro-reflected to produce an interference pattern. This provides tight confinement in the axial direction.

Radial confinement is more difficult to achieve. Accomplishing this using trap lasers in only one dimension will require a beam with a ring-shaped cross-section near the focus. Superimposing this beam on a standard retro-reflected lattice beam will produce a series of dark traps, as shown in Figure 7.2. There are a few established methods of producing such beams, including forked diffraction gratings [123], spiral

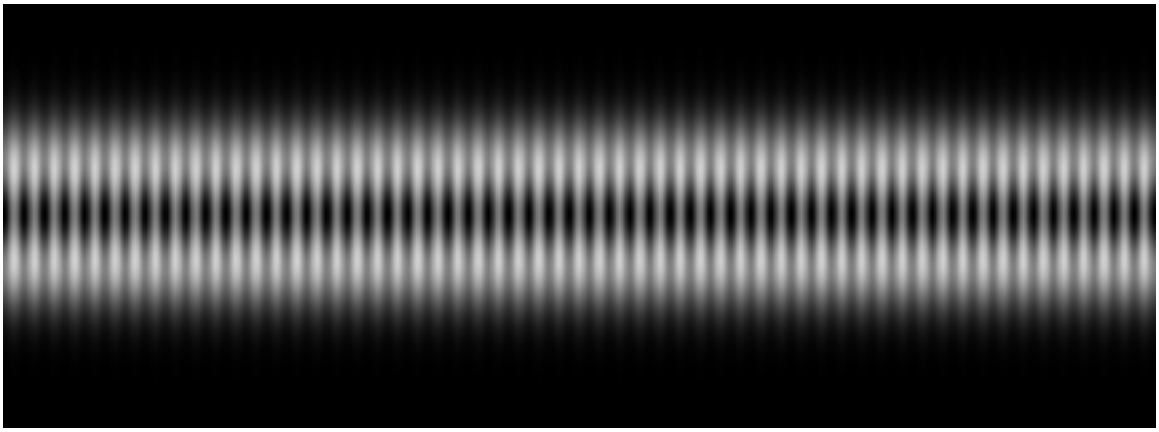

Figure 7.2: Simulated profile of a one dimensional blue detuned optical lattice. A retro-reflected Gaussian beam creates the lattice structure, while a co-propagating ring beam confines the atoms in the radial directions. Atoms are trapped in each of the dark locations.

Fresnel zone plates [124], and spiral phase plates [125]. Traditionally, these beams are primarily used for creating optical vortices [126]. For many applications, a non-uniform ring is sufficient, as long as it carries orbital angular momentum. For atom trapping, however, the ring must be as uniform as possible, since the trap depth is determined by the weakest point in the trap. The ring must also be created with as high an efficiency as possible, in order to produce a sufficiently deep trap. We use a spiral phase plate to create the ring beam, because it produces a near-ideal beam profile with high efficiency and low complexity.

7.2 Spiral Phase Plate

A spiral phase plate is a clear optic with varying thickness $T(\phi)$, given by

$$T(\phi) = T_0 + \frac{n\lambda}{2\pi}\phi, \tag{7.1}$$

where n is the order of the phase plate, λ is the design wavelength of the phase plate, and ϕ is the radial angle measured in the plane of the phase plate. A beam passing through the center of the phase plate, orthogonal to the plane of the optic, experiences a phase shift proportional to ϕ. Taking a Fourier transform of the beam profile gives

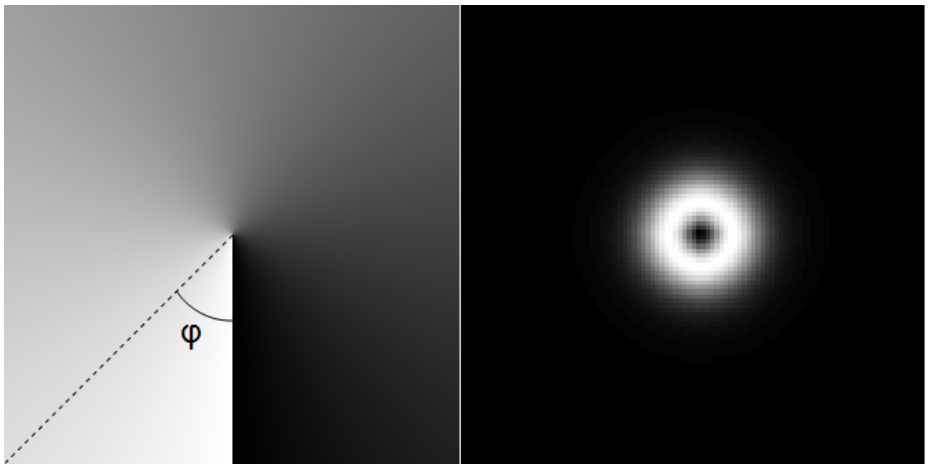

Figure 7.3: Simulation of an ideal spiral phase plate. (left) Thickness profile of a spiral phase plate. The thickness increases linearly with respect to the angle ϕ. (right) Predicted cross-section of a beam that has passed through a spiral phase plate, near its focus.

the expected beam shape at the focus, for an ideal spiral phase plate. For $n = 1$, this is a very close approximation of a LG01 (Laguerre-Gaussian) beam. The thickness profile of a spiral phase plate, as well as the expected cross-section of the resulting beam at its focus, are shown in Figure 7.3.

One of the simplest ways to construct a spiral phase plate is to cut a slit in a piece of flexible plastic and bend one of the resulting flaps [127]. On the bent side of the slit, the light propagates slightly farther through the plastic than on the unbent side. To first order, the resulting change in thickness is linear with the angle. One possible design uses a small piece of a blank transparency sheet, mounted on an optical mount, with set screws to determine the bend angle. While this does produce a ring beam, it was not sufficiently uniform for the current purposes. In particular, it contained a weak spot, due primarily to the poorly controlled discontinuity at $\phi = 2\pi$. The resulting beam is shown in Figure 7.4, as well as the simulated profile assuming a 0.5 mm discontinuity.

Several types of plastic were tried, with even less success. Finally, a professional spiral phase plate was commissioned, made step-wise using a diamond carving process.

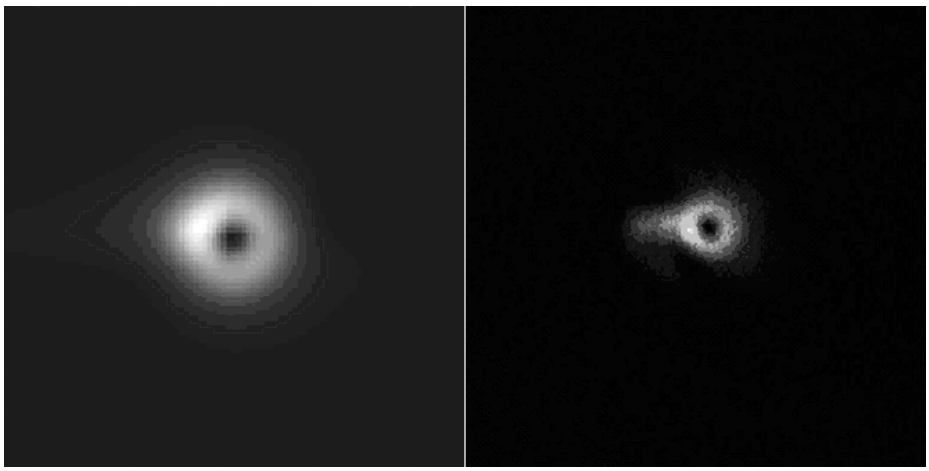

Figure 7.4: Predicted and measured results for a spiral phase plate made out of a blank transparency sheet. (left) Predicted beam cross-section, at the focus, for a beam that has passed through the phase plate. This assumes a 0.5 mm discontinuity at the point where the transparency is cut. (right) Measured beam cross-section, for a beam that has passed through the phase plate. The beam was measured at its focus using a webcam.

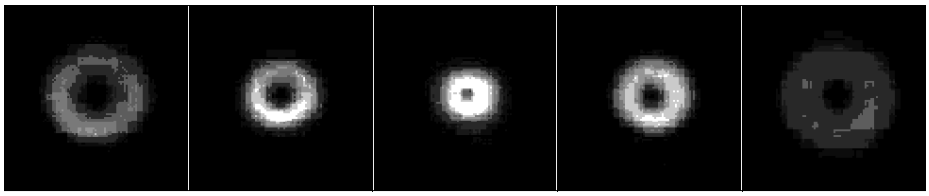

Figure 7.5: Beam profile of a ring beam made using a custom fabricated spiral phase plate. The pictures were taken (from left to right) 10 mm before the focus, 5 mm before the focus, at the focus, 5 mm after the focus, and 10 mm after the focus.

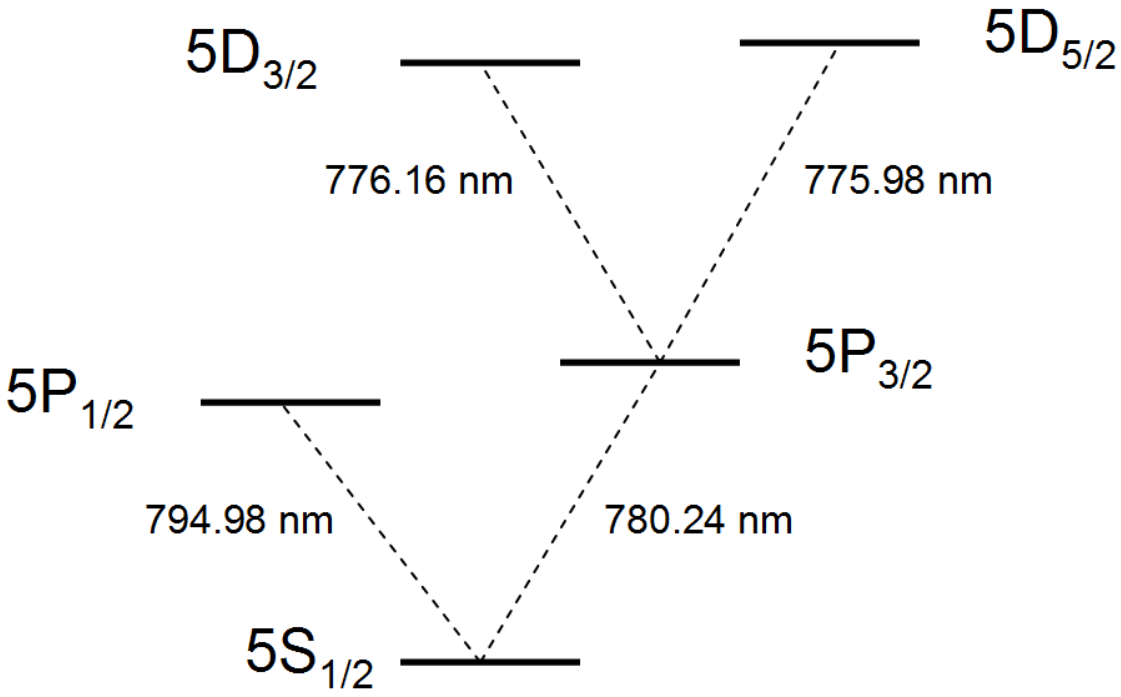

Figure 7.6: Relevant ground and excited state transitions for ^{87}Rb. Atoms in the $5P_{3/2}$ excited state can be further excited to either of the 5D states.

In theory, sixteen phase steps are enough to produce an efficiency of greater than 90% of the light in the LG01 mode. Experimentally, an efficiency of approximately 80% was observed, with the profile through the focus shown in Figure 7.5. Extremely precise alignment was necessary, not only through the phase plate, but through all subsequent optics. Even small deviations could prevent a ring from forming at the focus of the trap. Taking into account all of the efficiencies and losses, and using all of the power available, the resulting calculated trap depth is 660 μK. This is lower than would be ideal, but should be sufficient to achieve continuous observation of single atoms.

7.3 Initial Attempts

A hybrid trap was constructed as a first step towards a 1-D blue-detuned lattice. This system used the 1064 nm laser to first produce a single focus trap, as in previous

sections. A 50 mW co-propagating beam at 776 nm was then added, focused to 25 μm, which was retro-reflected to create a lattice. The expected result would be a trap similar to the 1-D optical lattice, but instead, when the blue-detuned light was turned on, all of the atoms immediately left the trap. After some investigation, it was found that the $5P_{3/2} \rightarrow 5D_{3/2}$ and $5P_{3/2} \rightarrow 5D_{5/2}$ transitions were being unintentionally excited. These transitions are located at 776.15 nm and 775.98 nm respectively, as shown in Figure 7.6. In order to remove the undesired wavelengths from the trapping laser, the trapping wavelength was changed to 777 nm and a diffraction grating (efficiency = 40%) was added after the tapered amplifier. Another attempt to produce a hybrid trap was performed, and this time it worked as expected. The atoms were continuously observed, with lifetimes greater than 20 s.

Unfortunately, while the diffraction grating allowed the successful construction of a hybrid trap, it significantly reduced the maximum power available for generating the trap. This reduced the maximum achievable trap depth to 270 μK. For the current system, this is probably not sufficient to perform continuous cooling. Several attempts were made to form a blue-detuned trap at this lower trap depth, but they were unsuccessful.

7.4 Possible Improvements

Ultimately, these attempts at making a blue-detuned trap were limited by the maximum power of the trapping laser. Several methods exist to deal with this issue. First, one could obtain a higher power laser. Tapered amplifiers with a maximum power of 2 W now exist at the desired wavelength and could probably produce enough power. Alternatively, a titanium sapphire laser could produce a high power beam without the amplified spontaneous emission pedestal characteristic of diode lasers.

CHAPTER VIII

CONCLUSION

This thesis has presented experimental work toward developing robust, reusable neutral atom qubits. The work examined the factors involved in trap heating, achieved optical lattice lifetimes far beyond previous records, and demonstrated non-destructive state detection of a neutral atom qubit. The work on non-destructive state detection is especially valuable because of its potential to advance quantum information science.

To begin, heating and cooling were thoroughly examined and optimized in an optical lattice. Single atoms were trapped in a MOT, and transferred to an optical lattice. Heating rates from various sources were measured and calculated, and ultimately compared. By using a laser with low intensity noise, atoms were trapped with lifetimes exceeding half a minute without any form of cooling. This lifetime was shown to be limited by position fluctuations in the optical trap. With active cooling to counteract this heating, a vacuum limited lifetime of over 300 s was achieved, which is five times longer than has been previously reported in a lattice.

These results were then replicated using pulsed cooling. Pulsing the cooling light as infrequently as once every 20 s was shown to give a lifetime almost indistinguishable from the lifetime with continuous cooling. This allows for a variety of state-sensitive quantum operations to be performed between cooling pulses, while still maintaining an extremely long lifetime.

A non-destructive state detection system was simulated by modeling a single atom in an optical lattice, with trap parameters that are achievable in the lab. Based on the promising outcome of the simulation, the system was constructed, and single atoms were prepared and detected in the $F = 1$ and $F = 2$ hyperfine states, producing results

that were only slightly worse than the simulation. This system attained an average state detection error rate around 5% and an atom loss rate less than 1%. Following this success, the experiment was reconfigured to prepare and detect each atom as many as 100 times, with a short cooling pulse between each cycle. Loss rates were slightly above 1% per cycle, while error rates remained around 5%. The resulting ability to retain an atom through multiple detection cycles will allow much faster repetition rates for quantum information experiments. Also, it could enable the use of more complex register loading schemes, which might otherwise take prohibitively long to conduct for every new quantum operation.

Next, individual atoms were prepared as qubits in quantum superposition states, using microwaves. State detection was performed for a variety of different microwave pulse lengths, producing Rabi oscillations. This represents the first demonstration of non-destructive state detection of a neutral atom qubit.

Initial attempts were made to recreate the single atom lattice in a blue trapping regime, in order to minimize the differential Stark shift and other disturbances caused by the trapping light. Although these efforts were thus far unsuccessful, it is likely that further effort, coupled with higher laser power, could produce more satisfactory results.

8.1 Future Work

Future work will focus on extending these results to create a fully functional quantum register. This process should be fairly straightforward. The first step is to improve qubit creation through optical pumping. By pumping the atoms into the $m_F = 0$ state before applying the microwaves, successful preparation rates approaching unity should be achievable.

Optical pumping could also be used to reduce the error rate for successful state detection. If the atoms are correctly oriented with respect to a magnetic field, then

a circularly polarized probe beam should pump them into the $m_F = 2$ state. From that state, σ_+ light cannot cause off-resonant depumping into the $F = 1$ state, due to conservation of angular momentum. Currently, such depumping is the primary source of errors. One other major source of error is due to probe light scattered off of the walls of the glass cell. This could be minimized by switching to an anti-reflection coated cell, or possibly by altering the probe configuration. If these two sources of error could be rendered negligible, error rates less than 1% should be readily achievable.

This system could be adapted to a multiple qubit register by changing the lattice into an optical conveyor. For a small number of qubits, probabilistic loading would be feasible. Each qubit could be moved into the region of interest and detected in turn. Another possible implementation would leave the atoms stationary, while moving the probe beam using an acousto-optical modulator or similar device. Alternatively, an array of photon counters or a low noise camera might allow multiple qubits to be detected at once.

Taken together, all of these improvements could result in a highly reliable multi-qubit detection system, with extremely low error and loss rates. Such a breakthrough would remove the bottleneck from neutral atom quantum information experiments, allowing greatly increased repetition rates, without sacrificing accuracy or reliability. Faster repetition would, in turn, allow more complex experiments.

By demonstrating extremely long storage times and non-destructive state detection of a neutral atom qubit, the work in this thesis will facilitate the development of faster and more complex quantum operations. These accomplishments provide foundations for exciting new developments in the field of quantum information.

REFERENCES

[1] Stockwell, F., *A history of information storage and retrieval*. Jefferson: McFarland & Company, Inc., 2001.

[2] Hollerith, H., "An electric tabulating system," *The Quarterly, Columbia University School of Mines*, vol. X, pp. 238–255, 1889.

[3] Feynman, R. P., "Simulating physics with computers," *Int. J. Theor. Phys.*, vol. 21, pp. 467–488, 1982.

[4] Deutsch, D., "Quantum theory, the church-turning principle and the universal quantum computer," *Proc. R. Soc. Lond. A*, vol. 400, no. 1818, pp. 97–117, 1985.

[5] Shor, P., "Algorithms for quantum computation: Discrete logarithms and factoring," *35th Annual Symposium on Foundations of Computer Science, 1994 Proceedings*, pp. 124–134, 1994.

[6] Grover, L., "Quantum mechanics helps in searching for a needle in a haystack," *Phys. Rev. Lett.*, vol. 79, no. 2, pp. 325–328, 1997.

[7] DiVincenzo, D. P., "The physical implementation of quantum computation," *Fortschritte der Physik - Progress of Physics*, vol. 48, pp. 771–783, 2000.

[8] Monroe, C., Meekhof, D. M., King, B. E., Itano, W. M., and Wineland, D. J., "Demonstration of a fundamental quantum logic gate," *Phys. Rev. Lett.*, vol. 75, no. 25, pp. 4714–4717, 1995.

[9] Turchette, Q. A., Wood, C. S., King, B. E., Myatt, C. J., Leibfried, D., Itano, W. M., Monroe, C., and Wineland, D. J., "Deterministic entanglement of two trapped ions," *Phys. Rev. Lett.*, vol. 81, no. 17, pp. 3631–3634, 1998.

[10] Leibfried, D., DeMarco, B., Meyer, V., Lucas, D., Barrett, M., Britton, J., Itano, W. M., Jelenkovic, B., Langer, C., Rosenband, T., and Wineland, D. J., "Experimental demonstration of a robust, high-fidelity geometric two ion-qubit phase gate," *Nature*, vol. 422, p. 412, 2003.

[11] Brickman, K. A., Haljan, P. C., Lee, P. J., Acton, M., Deslauriers, L., and Monroe, C., "Implementation of grover's quantum search algorithm in a scalable system," *Phys. Rev. A*, vol. 72, no. 5, p. 050306, 2005.

[12] Haffner, H., Hansel, W., Roos, C. F., Benhelm, J., al kar, D. C., Chwalla, M., Korber, T., Rapol, U. D., Riebe, M., Schmidt, P. O., Becher, C., Guhne, O., Dur, W., and Blatt, R., "Scalable multiparticle entanglement of trapped ions," *Nature*, vol. 438, no. 7068, pp. 643–646, 2005.

[13] Hensinger, W. K., Olmschenk, S., Stick, D., Hucul, D., Yeo, M., Acton, M., Deslauriers, L., Monroe, C., and Rabchuk, J., "T-junction ion trap array for two-dimensional ion shuttling, storage, and manipulation," *Appl. Phys. Lett.*, vol. 88, no. 3, p. 034101, 2006.

[14] Home, J. P., Hanneke, D., Jost, J. D., Amini, J. M., Leibfried, D., and Wineland, D. J., "Complete methods set for scalable ion trap quantum information processing," *Science*, vol. 325, no. 5945, pp. 1227–1230, 2009.

[15] Jaksch, D., Cirac, J. I., Zoller, P., Rolston, S. L., Cote, R., and Lukin, M. D., "Fast quantum gates for neutral atoms," *Phys. Rev. Lett.*, vol. 85, pp. 2208–2211, 2000.

[16] Hu, Z. and Kimble, H. J., "Observation of a single-atom in a magneto-optical trap," *Opt. Lett.*, vol. 19, no. 22, pp. 1888–1890, 1994.

[17] Frese, D., Ueberholz, B., Kuhr, S., Alt, W., Schrader, D., Gomer, V., and Meschede, D., "Single atoms in an optical dipole trap: Towards a deterministic source of cold atoms," *Phys. Rev. Lett.*, vol. 85, no. 18, pp. 3777–3780, 2000.

[18] Kuhr, S., Alt, W., Schrader, D., Muller, M., Gomer, V., and Meschede, D., "Deterministic delivery of a single atom," *Science*, vol. 293, pp. 278–280, 2001.

[19] Schrader, D., Dotsenko, I., Khudaverdyan, M., Miroshnychenko, Y., Rauschenbeutel, A., and Meschede, D., "Neutral atom quantum register," *Phys. Rev. Lett.*, vol. 93, no. 15, p. 150501, 2004.

[20] Volz, J., Weber, M., Schlenk, D., Rosenfeld, W., Vrana, J., Saucke, K., Kurtsiefer, C., and Weinfurter, H., "Observation of entanglement of a single photon with a trapped atom," *Phys. Rev. Lett.*, vol. 96, p. 030404, 2006.

[21] Wilk, T., Gaetan, A., Evellin, C., Wolters, J., Miroshnychenko, Y., Grangier, P., and Browaeys, A., "Entanglement of two individual neutral atoms using rydberg blockade," *Phys. Rev. Lett.*, vol. 104, p. 010502, 2010.

[22] Isenhower, L., Urban, E., Zhang, X. L., Gill, A. T., Henage, T., Johnson, T. A., Walker, T. G., and Saffman, M., "Demonstration of a neutral atom controlled-not quantum gate," *Phys. Rev. Lett.*, vol. 104, no. 1, p. 010503, 2010.

[23] Shor, P. W., "Scheme for reducing decoherence in quantum computer memory," *Phys. Rev. A*, vol. 52, p. R2493, 1995.

[24] Greiner, M., Mandel, O., Esslinger, T., Hansch, T. W., and Bloch, I., "Quantum phase transition from a superfluid to a mott insulator in a gas of ultracold atoms," *Nature*, vol. 415, pp. 39–44, 2002.

[25] Nelson, K. D., Li, X., and Weiss, D. S., "Imaging single atoms in a three-dimensional array," *Nature Physics*, vol. 3, no. 8, pp. 556–560, 2007.

[26] Bakr, W. S., Gillen, J. I., Peng, A., Folling, S., and Greiner, M., "A quantum gas microscope for detecting single atoms in a hubbard-regime optical lattice," *Nature*, vol. 462, pp. 74–78, 2009.

[27] Klinger, A., Degenkolb, S., Gemelke, N., Soderberg, K.-A. B., and Chin, C., "Optical lattices for atom-based quantum microscopy," *Rev. Sci. Instr.*, vol. 81, p. 013109, 2010.

[28] Migdall, A. L., Prodan, J. V., Phillips, W. D., Bergeman, T. H., and Metcalf, H. J., "First observation of magnetically trapped neutral atoms," *Phys. Rev. Lett.*, vol. 54, no. 24, pp. 2596–2599, 1985.

[29] Heer, C. V., "Feasibility of containment of quantum magnetic dipoles," *Rev. Sci. Instr.*, vol. 34, no. 5, p. 532, 1963.

[30] Pritchard, D. E., "Cooling neutral atoms in a magnetic trap for precision spectroscopy," *Phys. Rev. Lett.*, vol. 51, no. 15, pp. 1336–1339, 1983.

[31] Chu, S., Hollberg, L., Bjorkholm, J. E., Cable, A., and Ashkin, A., "Three-dimensional viscous confinement and cooling of atoms by resonance radiation pressure," *Phys. Rev. Lett.*, vol. 55, no. 1, pp. 48–51, 1985.

[32] Raab, E. L., Prentiss, M., Cable, A., Chu, S., and Pritchard, D. E., "Trapping of neutral sodium atoms with radiation pressure," *Phys. Rev. Lett.*, vol. 59, no. 23, pp. 2631–2634, 1987.

[33] Chu, S., Bjorkholm, J. E., Ashkin, A., and Cable, A., "Experimental observation of optically trapped atoms," *Phys. Rev. Lett.*, vol. 57, no. 3, pp. 314–317, 1986.

[34] Metcalf, H. J. and van der Straten, P., *Laser Cooling and Trapping*. New York: Springer, 1999.

[35] Foot, C. J., *Atomic Physics*. Oxford: Oxford University Press, 2005.

[36] Lett, P. D., Watts, R. N., Westbrook, C. I., Phillips, W. D., Gould, P. L., and Metcalf, H. J., "Observation of atoms cooled below the doppler limit," *Phys. Rev. Lett.*, vol. 61, no. 2, pp. 169–172, 1988.

[37] Ungar, P. J., Weiss, D. S., Riis, E., and Chu, S., "Optical molasses and multilevel atoms - theory," *J. Opt. Soc. Am. B*, vol. 6, no. 11, pp. 2058–2071, 1989.

[38] Dalibard, J. and Cohen-Tannoudji, C., "Laser cooling below the doppler limit by polarization gradients - simple theoretical models," *J. Opt Soc. Am. B*, vol. 6, no. 11, pp. 2023–2045, 1989.

[39] Corney, A., *Atomic and laser spectroscopy*. Oxford: Oxford University Press, 1977.

[40] Ashkin, A., "Acceleration and trapping of particles by radiation pressure," *Phys. Rev. Lett.*, vol. 24, no. 4, p. 156, 1970.

[41] Block, S., "Making light work with optical tweezers," *Nature*, vol. 360, no. 6403, pp. 493–495, 1992.

[42] Miller, J. D., Cline, R. A., and Heinzen, D. J., "Far-off-resonance optical trapping of atoms," *Phys. Rev. A*, vol. 47, no. 6, pp. R4567–R4570, 1993.

[43] Takamoto, M., Hong, F. L., Higashi, R., and Katori, H., "An optical lattice clock," *Nature*, vol. 435, no. 7040, pp. 321–324, 2005.

[44] Chin, C., Leiber, V., Vuletic, V., Kerman, A. J., and Chu, S., "Measurement of an electron's electric dipole moment using cs atoms," *Phys. Rev. A*, vol. 63, no. 3, p. 033401, 2001.

[45] Barrett, M. D., Sauer, J. A., and Chapman, M. S., "All-optical formation of an atomic bose-einstein condensate," *Phys. Rev. Lett.*, vol. 87, no. 1, p. 010404, 2001.

[46] Stamper-Kurn, D. M., Andrews, M. R., Chikkatur, A. P., Inouye, S., Miesner, H. J., Stenger, J., and Ketterle, W., "Optical confinement of a bose-einstein condensate," *Phys. Rev. Lett.*, vol. 80, no. 10, pp. 2027–2030, 1998.

[47] Schlosser, N., Reymond, G., Protsenko, I., and Grangier, P., "Sub-poissonian loading of single atoms in a microscopic dipole trap," *Nature*, vol. 411, no. 6841, pp. 1024–1027, 2001.

[48] Schlosser, N., Reymond, G., and Grangier, P., "Collisional blockade in microscopic optical dipole traps," *Phys. Rev. Lett.*, vol. 89, no. 2, p. 023005, 2002.

[49] Fortier, K. M., Kim, S. Y., Gibbons, M. J., Ahmadi, P., and Chapman, M. S., "Deterministic loading of individual atoms to a high-finesse optical cavity," *Phys. Rev. Lett.*, vol. 98, no. 23, p. 233601, 2007.

[50] Grimm, R., Weidemuller, M., and Ovchinnikov, Y. B., "Optical dipole traps for neutral atoms," *Advances in Atomic Molecular and Optical Physics*, vol. 42, pp. 95–170, 2000.

[51] O'Hara, K. M., Granade, S. R., Gehm, M. E., Savard, T. A., Bali, S., Freed, C., and Thomas, J. E., "Ultrastable co2 laser trapping of lithium fermions," *Phys. Rev. Lett.*, vol. 82, no. 21, pp. 4204–4207, 1999.

[52] Saleh, B. E. A. and Teich, M. C., *Fundamentals of Photonics*. New York: Wiley-Interscience, 1991.

[53] Salomon, C., Dalibard, J., Aspect, A., Metcalf, H., and Cohen-Tannoudji, C., "Channeling atoms in a laser standing wave," *Phys. Rev. Lett.*, vol. 59, pp. 1659–1662, 1987.

[54] Westbrook, C. I., Watts, R. N., Tanner, C. E., Rolston, S. L., Phillips, W. D., and Lett, P. D., "Localization of atoms in a three-dimensional standing wave," *Phys. Rev. Lett.*, vol. 65, pp. 33–36, 1990.

[55] Murr, K., Nussmann, S., Puppe, T., Hijlkema, M., Weber, B., Webster, S. C., Kuhn, A., and Rempe, G., "Three-dimensional cavity cooling and trapping in an optical lattice," *Phys. Rev. A*, vol. 73, no. 6, p. 063415, 2006.

[56] Boozer, A. D., Boca, A., Miller, R., Northup, T. E., and Kimble, H. J., "Cooling to the ground state of axial motion for one atom strongly coupled to an optical cavity," *Phys. Rev. Lett.*, vol. 97, no. 8, p. 083602, 2006.

[57] Greiner, M., Mandel, O., Esslinger, T., Hnsch, T. W., and Bloch, I., "Quantum phase transition from a superfluid to a mott insulator in a gas of ultracold atoms," *Nature*, vol. 415, no. 6867, pp. 39–44, 2002.

[58] Schrader, D., Kuhr, S., Alt, W., Muller, M., Gomer, V., and Meschede, D., "An optical conveyor belt for single neutral atoms," *Applied Physics B*, vol. 73, no. 8, pp. 819–824, 2001.

[59] Dahan, M. B., Peik, E., Reichel, J., Castin, Y., and Salomon, C., "Bloch oscillations of atoms in an optical potential," *Phys. Rev. Lett.*, vol. 76, pp. 4508–4511, 1996.

[60] Wilkinson, S. R., Bharucha, C. F., Madison, K. W., Niu, Q., and Raizen, M. G., "Observation of atomic wannier-stark ladders in an accelerating optical potential," *Phys. Rev. Lett.*, vol. 76, pp. 4512–4515, 1996.

[61] Miroshnychenko, Y., Alt, W., Dotsenko, I., Forster, L., Khudaverdyan, M., Meschede, D., Schrader, D., and Rauschenbeutel, A., "Continued imaging of the transport of a single neutral atom," *Opt. Express*, vol. 11, no. 25, pp. 3498–3502, 2003.

[62] Kuhr, S., Alt, W., Schrader, D., Dotsenko, I., Miroshnychenko, Y., Rosenfeld, W., Khudaverdyan, M., Gomer, V., Rauschenbeutel, A., and Meschede, D., "Coherence properties and quantum state transportation in an optical conveyor belt," *Phys. Rev. Lett.*, vol. 91, p. 213002, 2003.

[63] Miroshnychenko, Y., Alt, W., Dotsenko, I., Forster, L., Khudaverdyan, M., Meschede, D., Schrader, D., and Rauschenbeutel, A., "An atom-sorting machine," *Nature*, vol. 442, no. 7099, pp. 151–151, 2006.

[64] Eizmar, T., Garces-Chavez, V., Dholakia, K., and Zemaneka, P., "Transient nutations in nuclear magnetic resonance," *Appl. Phys. Lett.*, vol. 86, p. 174101, 2005.

[65] Kuhr, S., Alt, W., Schrader, D., Dotsenko, I., Miroshnychenko, Y., Rauschenbeutel, A., and Meschede, D., "Analysis of dephasing mechanisms in a standing-wave dipole trap," *Phys. Rev. A*, vol. 72, p. 023406, 2005.

[66] McKeever, J., Buck, J. R., Boozer, A. D., Kuzmich, A., Nagerl, H. C., Stamper-Kurn, D. M., and Kimble, H. J., "State-insensitive cooling and trapping of single atoms in an optical cavity," *Phys. Rev. Lett*, vol. 90, no. 13, p. 133602, 2003.

[67] Cetinbas, M., "Emergence of decoherence by incoherent manifestation of coherent quantum fluctuations," *J. Phys. A*, vol. 42, no. 14, p. 145302, 2009.

[68] DiVincenzo, D. P., "The physical implementation of quantum computation," *Fortschritte Der Physik*, vol. 48, no. 9–11, pp. 771–783, 2000.

[69] Kielpinski, D., Monroe, C., and Wineland, D. J., "Architecture for a large-scale ion-trap quantum computer," *Nature*, vol. 417, pp. 709–711, 2002.

[70] Balandin, A., Jin, G. L., and Wang, K. L., "Issues of practical realization of a quantum dot register for quantum computing," *J. Elec. Mat.*, vol. 29, pp. 549–553, 2000.

[71] Steck, D. A., "Rubidium 87 d line data." http://steck.us/alkalidata/; accessed Aug, 2010, 2009.

[72] Monroe, C., Swann, W., Robinson, H., and Wieman, C., "Very cold trapped atoms in a vapor cell," *Phys. Rev. Lett.*, vol. 65, no. 13, pp. 1571–1574, 1990.

[73] Gibble, K. E., Kasapi, S., and Chu, S., "Improved magneto-optic trapping in a vapor cell," *Opt. Lett.*, vol. 17, pp. 526–528, 1992.

[74] Haubrich, D., Hope, A., and Meschede, D., "A simple model for optical capture of atoms in strong magnetic quadrupole fields," *Opt. Comm.*, vol. 102, pp. 225–230, 1993.

[75] Sesko, D., Walker, T., Monroe, C., Gallagher, A., and Wieman, C., "Collisional losses from a light-force atom trap," *Phys. Rev. Lett.*, vol. 63, pp. 961–964, 1989.

[76] Vala, J., Thapliyal, A. V., Myrgren, S., Vazirani, U., Weiss, D. S., and Whaley, K. B., "Perfect pattern formation of neutral atoms in an addressable optical lattice," *Phys. Rev. A*, vol. 71, no. 3, p. 032324, 2005.

[77] Rozanov, L. N. and Hablanian, M. H., *Vacuum technique*. New York: Taylor & Francis, 2002.

[78] Savard, T. A., O'Hara, K. M., and Thomas, J. E., "Laser-noise-induced heating in far-off resonance optical traps," *Phys. Rev. A*, vol. 56, no. 2, pp. R1095–R1098, 1997.

[79] Coudreau, T., "Recent experiments in quantum information with trapped ions," *J. Phys. B*, vol. 42, p. 154011, 2009.

[80] Happer, W., "Optical pumping," *Rev. Mod. Phys.*, vol. 44, pp. 169–249, 1972.

[81] Unanyan, R., Fleischhauer, M., Shore, B. W., and Bergmann, K., "Robust creation and phase-sensitive probing of superposition states via stimulated raman adiabatic passage (stirap) with degenerate dark states," *Opt. Comm.*, vol. 155, pp. 144–154, 1998.

[82] Allen, L. and Eberly, J. H., *Optical Resonance and Two-Level Atoms*. New York: Dover Publications, Inc., 1975.

[83] Siegman, A. E., *Lasers*. Sausalito, CA: University Science Books, 1986.

[84] Torrey, H. C., "Transient nutations in nuclear magnetic resonance," *Phys. Rev.*, vol. 76, no. 8, pp. 1059–1068, 1949.

[85] Vanier, J. and Audoin, C., *The Quantum Physics of Atomic Frequency Standards*. Bristol: IOP Publishing, Ltd., 1989.

[86] Yavuz, D. D., Kulatunga, P. B., Urban, E., Johnson, T. A., Proite, N., Henage, T., Walker, T. G., and Saffman, M., "Fast ground state manipulation of neutral atoms in microscopic optical traps," *Phys. Rev. Lett.*, vol. 96, p. 063001, 2006.

[87] Lengwenus, A., Kruse, J., Volk, M., Ertmer, W., and Birkl, G., "Coherent manipulation of atomic qubits in optical micropotentials," *Appl. Phys. B*, vol. 86, pp. 377–383, 2007.

[88] Jones, M. P. A., Beugnon, J., Gaetan, A., Zhang, J., Messin, G., Browaeys, A., and Grangier, P., "Fast quantum state control of a single trapped neutral atom," *Phys. Rev. A*, vol. 75, p. 040301, 2007.

[89] Khudaverdyan, M., Alt, W., Kampschulte, T., Reick, S., Thobe, A., Widera, A., and Meschede, D., "Quantum jumps and spin dynamics of interacting atoms in a strongly coupled atom-cavity system," *Phys. Rev. Lett.*, vol. 103, p. 123006, 2009.

[90] Bochmann, J., Mucke, M., Guhl, C., Ritter, S., Rempe, G., and Moehring, D. L., "Lossless state detection of single neutral atoms," *Phys. Rev. Lett.*, vol. 104, no. 20, p. 203601, 2010.

[91] Gehr, R., Volz, J., Dubois, G., Steinmetz, T., Colombe, Y., Lev, B. L., Long, R., Esteve, J., and Reichel, J., "Cavity-based single atom preparation and high-fidelity hyperfine state readout," *Phys. Rev. Lett.*, vol. 104, p. 203602, 2010.

[92] Schulz, L., "Sputter-ion pumps," *CERN European Organization for Nuclear Research Reports*, vol. 5, pp. 37–42, 1999.

[93] Favre, F., le Guen, D., Simon, J., and Landousies, B., "External-cavity semiconductor laser with 15 nm continuous tuning range," *Electronics Lett.*, vol. 22, pp. 795–796, 1986.

[94] Libbrecht, K. G. and Hall, J. L., "A low-noise high speed diode laser current controller," *Rev. Sci. Instr.*, vol. 64, p. 2133, 1993.

[95] Bradley, C. C., Chen, J., and Hulet, R. G., "Instrumentation for the stable operation of laser diodes," *Rev. Sci. Instr.*, vol. 61, p. 2097, 1990.

[96] Fortier, K. M., "Individual trapped atoms for cavity qed quantum information applications." Diss., Georgia Institute of Technology, Atlanta, 2007.

[97] Kim, S. Y., "Cold single atoms for cavity qed experiments." Diss., Georgia Institute of Technology, Atlanta, 2008.

[98] Klempt, C., van Zoest, T., Henninger, T., Topic, O., Rasel, E., Ertmer, W., and Arlt, J., "Ultraviolet light-induced atom desorption for large rubidium and potassium magneto-optical traps," *Phys. Rev. A*, vol. 73, no. 1, p. 013410, 2006.

[99] Hope, A., Haubrich, D., Muller, G., Kaenders, W. G., and Meschede, D., "Neutral cesium atoms in strong magnetic-quadrupole fields at sub-doppler temperatures," *Europhys. Lett.*, vol. 22, pp. 669–674, 1993.

[100] Adams, C. S., Lee, H. J., Davidson, N., Kasevich, M., and Chu, S., "Evaporative cooling in a crossed dipole trap," *Phys. Rev. Lett.*, vol. 74, pp. 3577–3580, 1995.

[101] Alt, W., Schrader, D., Kuhr, S., Muller, M., Gomer, V., and Meschede, D., "Single atoms in a standing-wave dipole trap," *Phys. Rev. A*, vol. 67, no. 3, p. 033403, 2003.

[102] Gardiner, C. W., J. Ye, H. C. N., and Kimble, H. J., "Evaluation of heating effects on atoms trapped in an optical trap," *Phys. Rev. A*, vol. 61, no. 4, p. 045801, 2000.

[103] Kuppens, S. J. M., Corwin, K. L., Miller, K. W., Chupp, T. E., and Wieman, C. E., "Loading an optical dipole trap," *Phys. Rev. A*, vol. 62, p. 013406, 2000.

[104] Hoffmann, D., Feng, P., and Walker, T., "Measurements of rb trap-loss collision spectra," *J. Opt. Soc. Am. B*, vol. 11, no. 5, pp. 712–720, 1994.

[105] Bjorkholm, J. E., "Collision-limited lifetimes of atom traps," *Phys. Rev. A*, vol. 38, no. 3, pp. 1599–1600, 1988.

[106] Wallace, C. D., Dinneen, T. P., Tan, K.-Y. N., Grove, T. T., and Gould, P. L., "Isotopic difference in trap loss collisions of laser cooled rubidium atoms," *Phys. Rev. Lett.*, vol. 69, no. 6, pp. 897–900, 1992.

[107] Bacon, A. M., Zhao, H. Z., Wang, L. J., and Thomas, J. E., "Microwatt shot-noise measurement," *Appl. Opt.*, vol. 34, no. 24, pp. 5326–5330, 1995.

[108] Wu, J. W., Newell, R., Hausmann, M., Vieira, D. J., and Zhao, X. X., "Loading dynamics of optical trap and parametric excitation resonances of trapped atoms," *J. Appl. Phys.*, vol. 100, no. 5, p. 054903, 2006.

[109] Friebel, S., D'Andrea, C., Walz, J., Weitz, M., and Hansch, T. W., "Co2-laser optical lattice with cold rubidium atoms," *Phys. Rev. A*, vol. 57, no. 1, pp. R20–R23, 1998.

[110] Gehm, M. E., O'Hara, K. M., Savard, T. A., and Thomas, J. E., "Dynamics of noise-induced heating in atom traps," *Phys. Rev. A*, vol. 58, no. 5, pp. 3914–3921, 1998.

[111] Acton, M., Brickman, K. A., Haljan, P. C., Lee, P. J., Deslauriers, L., and Monroe, C., "Near-perfect simultaneous measurement of a qubit register," *Quant. Inf. Comput.*, vol. 6, pp. 465–482, 2006.

[112] Olmschenk, S., Younge, K. C., Moehring, D. L., Matsukevich, D. N., Maunz, P., and Monroe, C., "Manipulation and detection of a trapped yb+ hyperfine qubit," *Phys. Rev. A*, vol. 76, p. 052314, 2007.

[113] Roos, C. F., Lancaster, G. P. T., Riebe, M., Haffner, H., Hansel, W., Gulde, S., Becher, C., Eschner, J., Schmidt-Kaler, F., and Blatt, R., "Bell states of atoms with ultralong lifetimes and their tomographic state analysis," *Phys. Rev. Lett.*, vol. 92, p. 220402, 2004.

[114] Nagourney, W., Sandberg, J., and Dehmelt, H., "Shelved optical electron amplifier: Observation of quantum jumps," *Phys. Rev. Lett.*, vol. 56, pp. 2797–2799, 1986.

[115] Bergquist, J. C., Hulet, R. G., Itano, W. M., and Wineland, D. J., "Observation of quantum jumps in a single atom," *Phys. Rev. Lett.*, vol. 57, pp. 1699–1702, 1986.

[116] Sauter, T., Neuhauser, W., Blatt, R., and Toschek, P. E., "Observation of quantum jumps," *Phys. Rev. Lett.*, vol. 57, pp. 1696–1698, 1986.

[117] Arora, B., Safronova, M. S., and Clark, C. W., "Magic wavelengths for the np-ns transitions in alkali-metal atoms," *Phys. Rev. A*, vol. 76, p. 052509, 2007.

[118] Arora, B., Safronova, M. S., and Clark, C. W., "State-insensitive bichromatic optical trapping," *Phys. Rev. A*, vol. 82, p. 022509, 2010.

[119] Lundblad, N., Schlosser, M., and Porto, J. V., "Experimental observation of magic-wavelength behavior of ^{87}rb atoms in an optical lattice," *Phys. Rev. A*, vol. 81, p. 031611, 2010.

[120] Davidson, N., Lee, H. J., Adams, C. S., Kasevich, M., and Chu, S., "Long atomic coherence times in an optical dipole trap," *Phys. Rev. Lett.*, vol. 74, pp. 1311–1314, 1995.

[121] Takamoto, M., Katori, H., Marmo, S. I., Ovsiannikov, V. D., and Pal'chikov, V. G., "Prospects for optical clocks with a blue-detuned lattice," *Phys. Rev. Lett.*, vol. 102, no. 6, p. 063002, 2009.

[122] Xu, P., He, X. D., Wang, J., and Zhan, M. S., "Trapping a single atom in a blue detuned optical bottle beam trap," *Opt. Lett.*, vol. 35, no. 13, pp. 2164–2166, 2010.

[123] Singh, R. P., Roychowdhury, S., and Jaiswal, V. K., "Optical vortices produced by forked holographic grating and sign of their topological charge," *Indian Journal of Physics and Proceedings of the Indian Assiciation for the Cultivation of Science*, vol. 80, no. 5, pp. 491–494, 2006.

[124] Heckenberg, N. R., McDuff, R., Smith, C. P., and White, A. G., "Generation of optical-phase singularities by computer-generated holograms," *Opt. Lett.*, vol. 17, no. 3, pp. 221–223, 1992.

[125] Watanabe, T., Fujii, M., Watanabe, Y., Toyama, N., and Iketaki, Y., "Generation of a doughnut-shaped beam using a spiral phase plate," *Rev. Sci. Instr.*, vol. 75, no. 12, pp. 5131–5135, 2004.

[126] Kotlyar, V. V., Kovalev, A. A., Skidanov, R. V., Khonina, S. N., and Moiseev, O. Y., "Simple optical vortices formed by a spiral phase plate," *J. Opt. Tech.*, vol. 74, no. 10, pp. 686–693, 2007.

[127] Rotschild, C., Zommer, S., Moed, S., Hershcovitz, O., and Lipson, S. G., "Adjustable spiral phase plate," *Appl. Opt.*, vol. 43, no. 12, pp. 2397–2399, 2004.